

UCLA

UCLA Electronic Theses and Dissertations

Title

The Fundamental Photophysics Underlying Near and Shortwave Infrared Chromophores

Permalink

<https://escholarship.org/uc/item/0790t0wx>

Author

Friedman, Hannah Concetta

Publication Date

2022

Peer reviewed|Thesis/dissertation

UNIVERSITY OF CALIFORNIA

Los Angeles

The Fundamental Photophysics Underlying  
Near and Shortwave Infrared Chromophores

A dissertation submitted in partial satisfaction of the  
Requirements for the degree for Doctor of Philosophy  
in Chemistry

by

Hannah Concetta Friedman

2022

© Copyright by

Hannah Concetta Friedman

2022

## ABSTRACT OF THE DISSERTATION

The Fundamental Photophysics Underlying  
Near and Shortwave Infrared Chromophores

by

Hannah Concetta Friedman

Doctor of Philosophy in Chemistry

University of California Los Angeles, 2022

Professor Justin Ryan Caram, Chair

Rational design of bright near and shortwave infrared (NIR: 700-1000 SWIR: 1000-2000 nm) molecular and nanoscale emitters is fundamental for applications ranging from deep tissue imaging to telecommunications. However, currently all reported organic chromophores with energy gaps in the SWIR have suboptimal properties due to their especially low fluorescent quantum yields. This thesis introduces the main questions pertaining to molecular absorption and emission in Chapter 1, and in Chapter 2 demonstrates the fundamental principles that govern photophysical properties of SWIR dyes, explicating the precipitous decline of quantum yield with longer wavelengths. I demonstrate that for polymethine dyes such declines are consistent with the combination of decreased radiative rates due to shrinking singlet energy gaps and increased nonradiative deactivation via high frequency vibrations. Through simplifying and combining earlier energy gap laws, I develop an energy gap independent parameter that enables comparison

of quantum yields among NIR/SWIR chromophores independent of the differences between each molecule's energy gaps. Applying the energy gap independent parameter, I provide predictions on whether specific synthetic modifications of a dye would lead to improvements in photophysical properties. In Chapter 3, I recontextualize my work in terms of brightness, which is the quantum yield weighted by the dye's absorptivity, a paramount chromophore property for imaging applications. Here the analysis expands to a greater survey of other dye scaffolds. In Chapter 4, I show preliminary experimental work that tests temperature dependence, heavy atom effects, and other dye scaffolds. In Chapter 5, I discuss potential synthetic and photophysical experiments to further understand the molecular parameters important to bright SWIR chromophores. Modelling both molecular and solvation impacts of fluorescence lifetimes and quantum yield will give both synthetic and physical chemists a handle on key variables to help develop better organic SWIR imaging systems.

The dissertation of Hannah Concetta Friedman is approved.

Miguel A. Garcia-Garibay

Chong Liu

Benjamin Joel Schwartz

Justin Ryan Caram, Committee Chair

University of California, Los Angeles

2022

*To my parents, the original Caram lab crew, Midnight and  
other fluffy friends who have supported me.*

## TABLE OF CONTENTS

Chapter 1. Introduction to NIR/SWIR Photoluminescence.....	1
1.1. Introduction.....	1
1.2. What is Photoluminescence.....	1
1.3. What is NIR/SWIR and Why Do We Care?.....	2
1.4. Photophysical Figures of Merit for Imaging: Quantum Yield and Brightness.....	4
1.5. Qualitative Relationship Between Energy Gap and Quantum Yield into SWIR.....	4
1.6. Probability of Transition: Fermi's Golden Rule.....	6
1.7. Primer on Radiative Rate Energy Gap Law.....	7
1.8. Primer on Nonradiative Rate Energy Gap Law .....	10
Chapter 2. Establishing Design Principles for Emissive Organic SWIR Chromophores from Energy Gap Laws.....	14
2.1. Introduction.....	14
2.2. Results.....	17
2.2a. The First Energy Gap Law - Radiative Rates.....	21
2.2b. The Second Energy Gap Law - Nonradiative Rates.....	23
2.2c. Energy Gap Quantum Yield Master Equation.....	26
2.2d. Comparing Chromophore Quantum Yield while Accounting for Energy Gap Changes.....	28
2.2e. Overcoming Energy Gap Laws.....	32
2.3. Discussion.....	35
2.4. Conclusion.....	38
2.5. Supporting Information.....	39
2.5a. Methods.....	39
2.5a.i. Materials.....	39
2.5a.ii. Absorption coefficients.....	39



2.5a.iii. Fluorescence quantum yield.....	40
2.5a.iv. Time correlated single photon counting.....	40
2.5b. Modeling Absorption and Emission.....	42
2.5b.i. Einstein coefficients, absorption, and emission.....	43
2.5b.ii. Absorption parameters to Einstein coefficients.....	45
2.5b.iii. Comparison to the Strickler-Berg equation.....	48
2.5b.iv. Relating Einstein coefficients to transition dipole moments.....	49
2.5b.v. Oscillator strength.....	50
2.5c. Nonradiative Rate Estimation.....	51
2.5c.i. Exponential rate law assumptions.....	51
2.5c.ii. Impact of $\gamma_m$ and $C$ on quantum yield.....	54
2.5d. EQME with Labelled Polymethine Dyes.....	56
2.5e. Derivation of Comparison Equation.....	58
2.5e.i. Enhanced worked example.....	60
2.5e.ii. Comparison relative to IR-27 (dye 4).....	62
2.5f. Overcoming Energy Gap Laws.....	63
2.5f.i. Enhancement from changing maximum vibrational stretch comparing parameters.....	63
2.5f.ii. Synthesis and characterization of dye 3' and 3''.....	64
2.5f.iii. Comparison of dyes 3, 3', and 3'' spectral properties.....	72
2.5f.iv. T-test and error propagation.....	72
2.5g. 50% Quantum Yield Scaffold Comparison.....	73
2.5h. Solvent Deuteration Impact on Fluorescence Lifetime.....	75
Chapter 3. The Optimization Problem for Shortwave Infrared Fluorescence Chromophores.....	76
3.1. Introduction.....	76

3.2. Defining Maximum Brightness.....	80
3.3. Using “Particle in a Box” to Determine $\mu_{21}$ .....	84
3.4. Maximizing Quantum Yield and Brightness Specific Energy of Fluorescence.....	85
3.5. Deuteration Impact on Brightness.....	88
3.6. Conclusions.....	91
Chapter 4 Challenges and Collaborations.....	92
4.1. Toward Temperature Dependent Photophysics.....	92
4.2. Heavy Atom Effect.....	96
4.2a. Internal Heavy Atom Effect.....	96
4.2b. External Heavy Atom Effect .....	99
4.3. Silicon-Rosindolizine Fluorophores.....	102
4.4. Deuteration of Additional Polymethine Scaffolds.....	104
4.5. General Lifetime Methods.....	106
4.6. Future Directions.....	107
Chapter 5 Outlook on Photophysics in the SWIR.....	109
References.....	113

## LIST OF FIGURES

Figure 1.1. Jablonski diagram.....	2
Figure 1.2. Definition and applications of shortwave infrared light.....	3
Figure 1.3. Literature results showing energy gap with quantum yield and brightness .....	5
Figure 1.4. Diagram of displaced harmonic oscillator with an avoided crossing in frequency space.....	12
Figure 2.1. Chromophores studied in this chapter .....	16
Figure 2.2. Representative plots of photophysical measurements used to determine energy law constants.....	18
Figure 2.3. Polymethines follow the radiative rate energy gap law .....	23
Figure 2.4. $k_{nr}$ are governed by high-frequency vibrational mode $E_M > 3000\text{cm}^{-1}$ .....	26
Figure 2.5. EQME provides consistent upper bounds for SWIR quantum yields .....	27
Figure 2.6. Energy gap free QY comparator, $\xi$ uncovers a linear free energy relationship.....	31
Figure 2.7. Deuteration and increased transition dipole moment enhances PLQY in SWIR .....	33
Figure 2.8. 50% quantum yield energy map .....	36
Figure 2.9. Example lifetime fit.....	42
Figure 2.10. Depiction of Einstein coefficients .....	45
Figure 2.11. Vibronic feature comparison .....	54
Figure 2.12. Impact of $\gamma_M$ or $C$ on the quantum yield with respect to energy gap .....	55
Figure 2.13. Labelled version of Figure 2.5.....	56
Figure 2.14. EQME slope versus the $\kappa$ estimation.....	60
Figure 2.15. Worked out example of the energy gap independent parameter .....	62
Figure 2.16. Energy gap independent parameter using Dye 4 as the standard .....	63
Figure 2.17. Impact of deuteration based on different EQME conditions .....	64
Figure 2.18. Synthesis of S1 .....	65
Figure 2.19. $^1\text{HNMR}$ of S1 (top) and $^{13}\text{CNMR}$ of S1 (bottom) .....	67

Figure 2.20. Synthesis of 3'	68
Figure 2.21. <sup>1</sup> HNMR of 3'	69
Figure 2.22. Mass spectra of 3'	69
Figure 2.23. Synthesis of 3''	70
Figure 2.24. <sup>1</sup> HNMR of 3''	71
Figure 2.25. Mass spectra of 3''	71
Figure 2.26. Steady state spectra of dye 3, 3' and 3''	72
Figure 2.27. Impact of solvent deuteration of fluorescence lifetime	75
Figure 3.1. Introduction to brightness in the NIR/SWIR	77
Figure 3.2. Structures of NIR/SWIR fluorophores	78
Figure 3.3. $E_{ST}$ and $E_{bc}$ and their impact on “equivalent” Gaussian lineshape	83
Figure 3.4. Impact of brightness based on energy using Kuhn’s “particle in a box” model	85
Figure 3.5. Overall brightness and quantum yield are maximized at small vibrational displacement	87
Figure 3.6. Deuteration of Flav7 and the impact on quantum yields and lifetimes	90
Figure 4.1. H-aggregation induced by cooling	93
Figure 4.2. Observation of color change and quick temperature probe set-up	94
Figure 4.3. Temperature dependence of Chrom5 and Chrom7	95
Figure 4.4. Impact of sulfur as heteroatom in polymethine dyes	98
Figure 4.5. Redshift in absorption and emission with increasingly heavier atom solvent molecules	99
Figure 4.6. Relative quantum yield for Flav5 and Flav7 in different solvents	100
Figure 4.7. Structure of linear 7 chain polymethine dyes	105
Figure 5.1. Synthetic approaches toward better SWIR chromophores	110
Figure 5.2. Examples of photophysical experiments to test assumptions associated with energy gap law for nonradiative rates	112

## LIST OF TABLES

Table 2.1. Experimentally Derived Values for the Energy Gap Laws.....	19
Table 2.2. Calculated Values for Dyes Studied.....	20
Table 2.3. Enhancement of Dyes Compared to Dye 4 (IR-27).....	29
Table 2.4. Unit Table.....	44
Table 2.5. Key for Figure 2.13.....	57
Table 2.6. Errors Used in t-tests.....	73
Table 2.7. Values of Other Dye Scaffolds for Comparison Method.....	74
Table 3.1. Photophysical Properties of Select NIR/SWIR Fluorophores of Different Classes....	80
Table 3.2. Deuteration Impacts Quantum Yield and Brightness for Polymethine Dyes.....	88
Table 4.1. Photophysical Properties of Chromenylium and Thiochromenylium Dyes.....	97
Table 4.2. Photophysical Properties of Flav7 and Flav5 in Different Solvents.....	101
Table 4.3. Lifetimes and Other Photophysical Properties of SiRos Dyes.....	104
Table 4.4. Steady State Photophysical Properties of Linear Polymethine Dyes.....	105
Table 4.5. Time Resolved Photophysical Properties of Linear Polymethine Dyes.....	106
Table 4.6. Instrument Response Function Fit Parameters.....	107

## ACKNOWLEDGEMENTS

I must first acknowledge my advisor Justin Caram for all the support. The journey of coworking together, going down tangents, as well as reigning in my detours was instrumental in helping me become a better scientist. Within the Caram lab, I would like to thank Dr. Timothy Atallah, a former postdoc, for being a strong second mentor in general and specifically with laser spectroscopy. Additionally, I would like to thank Anthony Sica and Ash Hua for their subsequent help with lifetime measurements. Dr. Ellen Sletten and her former student Dr. Emily Cosco were influential organic collaborators for Chapter 2, for the usage of their novel organic compounds but more importantly for their contributions to making the published version of Chapter 2 more accessible to synthetic chemists. Additionally, from the Sletten laboratory, I would like to thank Dr. Shang Jia (Chapter 2), Cesar Garcia (Chapter 3 and 4), and Anthony Spearman (Chapter 3 and 4) for additional novel compounds.

I would like to thank Dr. Jared Delcamp and his students, David Ndaleh and William Meador, from Ole Miss and Dr. Peter Štacko and his PhD student Hana Janeková from the University of Zurich for novel compounds to study the photophysics (Chapter 4). I would also like to thank Dr. Seogjoo Jang and Dr. Pablo Ramos from Queens College of CUNY for quantum mechanical calculations (Chapter 4).

I would like to thank my committee of Benjamin J Schwartz, Chong Liu, and Miguel Garcia-Garibay and the entire UCLA's Chemistry and Biochemistry department for invaluable support and advice.

Graduate school is a group effort even beyond science. I would like to thank Maya Segal and Cheylene Tanimoto for being my first friends and study buddies who helped me survive quantum and statistical mechanics. My deepest thanks for Arundhati Deshmukh and Timothy

Atallah who were my emotional rocks for most of my time within the Caram group, and Jill Williams for taking on that role in my final years. Outside of the department, organizations like Queers and Trans in STEM, CNSI education program, and the UCLA LGBT Campus Resource Center helped me put difficult days into perspective. I would like to thank my parents, Stella Biderman, Paul Sieminski, and many people from the internet for sending cute often fluffy or funny things to cheer me up. Pets are probably some of the biggest support systems for my mental health so I would like to thank Midnight, Percy, Joey, Chandler, Coco, Noodle, Jasper, Spot, and Peach for being the best boys and girls.

For personal funding I would like to acknowledge the UCLA Graduate Council Diversity Fellowship (2020) and the UCLA Chemistry and Biochemistry SG Fellowship (2020). I would like to thank project funding of NSF grant no. CHE-1905242, CHE-1945572, NIBIB grant no. 1R01EB027172, and instrumentation grants NSF no. CHE-1048804 and NIH no. 1S10OD016387.

Chapter 2 is adapted from “Friedman, H. C., Cosco, E.M., Atallah, T.L., Sletten, E.M., Caram, J. R., “Establishing design principles for brightly emissive organic SWIR emitters” *Chem.* 7(12). 3359-3376. (2021)” Copyright 2021 Elsevier Inc. Chapter 3 is from a manuscript in preparation discussing impact on steady state photophysical properties on brightness in the NIR. Chapter 4 is a compilation of thoughts from work with collaborators, discussion from experiments that do not fit into previous chapters.

## BIOGRAPHICAL SKETCH

### Education

2016 Bachelor of Science in Chemistry, *University of Chicago*, Chicago, IL

### Publications

1. **Friedman, H.C.**, Garcia, C., Hua, A.S., Sletten, E.M., Caram, J.R. “The Optimization Problem for Shortwave Infrared Fluorescence Chromophores”. In preparation.
2. Meader, W.E., Lin, E.Y., Lim, I., **Friedman, H.C.**, Ndaleh, D., Shaik, A.K., Hammer, N.I., Yang, B., Caram, J.R., Sletten, E.M., Delcamp, J.H. “Shortwave Infrared Absorbing and Emitting Silicon-Rosindolizine Fluorophores for *in vivo* Fluorescence Imaging”. In preparation.
3. Ramos, P., **Friedman, H.C.**, Caram, J.R. and Jang, S.J. “Elucidating energy gap dependences of nonradiative transition rates”. In preparation.
4. **Friedman, H. C.**, Cosco, E.M., Atallah, T.L., Sletten, E.M., Caram, J. R., “Establishing design principles for brightly emissive organic SWIR emitters”. *Chem.* **7**(12). 3359-3376. (2021). <https://doi.org/10.1016/j.chempr.2021.09.001>
5. Atallah, T.L., Sica, A. V., Shin, A.J., **Friedman, H.C.**, Kahrobai, Y.K., Caram, J.R., “Decay Associated Fourier Spectroscopy: Visible to Shortwave Infrared Time-Resolved Photoluminescence Spectra”. *J. Phys. Chem. A.* **123**(31). 6792-6798 (2019). <https://doi.org/10.1021/acs.jpca.9b04924>

### Presentations

- 2022 Electron Donor-Acceptor Interactions Gordon Research Seminar and Conference, Salve Regina University, Newport, RI (Oral and Poster)
- 2021 ACS Virtual Spring Meeting (Oral)



- 2019 ACS National Meeting, San Diego (Poster)
- 2019 Southern California Inorganic Photochemistry (Oral)
- 2019 Pacific Conference on Spectroscopy and Dynamics, San Diego (Poster)
- 2018 Seaborg Symposium, UCLA (Poster)

### **Awards and Honors**

- 2021 Mike Jung Excellence in Teaching Award, *UCLA*
- 2020 Graduate Council Diversity Fellowship, *UCLA*
- 2020-2022 Center for Diverse Leadership in Science (CDLS) Early Career Fellow, *UCLA*
- 2020 SG Fellowship, *UCLA Chem. and Biochem. Dept.*
- 2019 UCLA Research Showcase Fellowship Award, *UCLA Chem. and Biochem. Dept.*
- 2019 Pacific Conference on Spectroscopy and Dynamics Scholarship
- 2012-2016 University Scholarship, *University of Chicago*

### **Leadership and Service**

- 2020-2021 *Member, LGBTQ Advocacy Committee, UCLA*
- 2019-2020 *Member, Joint Research Safety Initiative, UCLA*
- 2019-2020 *Mentor, Undergraduate Students, UCLA*
- 2018 *Graduate Student Representative, UCLA LGBTQ Campus Resource Center for Hiring Committee*
- 2017-2022 *President (2019-2021), Queer and Trans, UCLA*
- 2017-2021 *Volunteer, Teacher training workshops and demos, CNSI Outreach program, UCLA*
- 2017-2021 *Volunteer, Exploring Your Universe, UCLA*

# Chapter 1

## Introduction to NIR/SWIR Photoluminescence

### 1.1. Introduction

When light interacts with an object, it is either absorbed, reflected, or scattered. In this thesis, I will focus on what happens to light after it has been absorbed, where the light energy can either be dissipated as heat (a nonradiative process) or can be re-emitted in all directions (a radiative process). Each result has wide applications, including driving chemical reactions, photodynamic and photothermal therapies for nonradiative processes, and biological imaging, forensics and lighting for radiative processes. My thesis work focuses on the interplay between radiative and nonradiative pathways in organic molecules with a particular focus on the shortwave infrared, the spectral window just beyond where our eyes can see.

### 1.2. What is Photoluminescence?

To understand light emission, or photoluminescence, one needs to understand the changes to electrons that underlie a molecule's interaction with light. Usually, the highest occupied molecular orbital of a physical system has a ground state where electrons are paired within an orbital with opposite spins, referred to as a singlet state ( $S_0$ ). When a single photon (or quantum particle of light) of enough energy interacts with the ground state it can promote an electron to an unoccupied molecular orbital. In most cases, the photon cannot flip the spin of the electron and thus this process creates an excited singlet state ( $S_n$ ). An exciton, or bound pair between the excited negatively charged electron and its positively charged hole left over in the highest unoccupied molecular orbital has multiple avenues to return to  $S_0$ . If it relaxes back to the ground state by dissipating energy into vibrational modes or the solvent, one says it underwent internal conversion.

If it decays back radiatively that process is called fluorescence. The excited electron can flip spin and transfer to the triplet state in a process called intersystem crossing. Intersystem crossing also applies when the triplet exciton nonradiatively decays to the ground state singlet. When a triplet exciton decays radiatively, it is called phosphorescence. This relaxation pathway, since it is considered spin forbidden, has longer lifetimes and is less probable than the spin allowed fluorescence. Figure 1.1 shows a Jablonski diagram of the energetic interplay of the different exciton states.

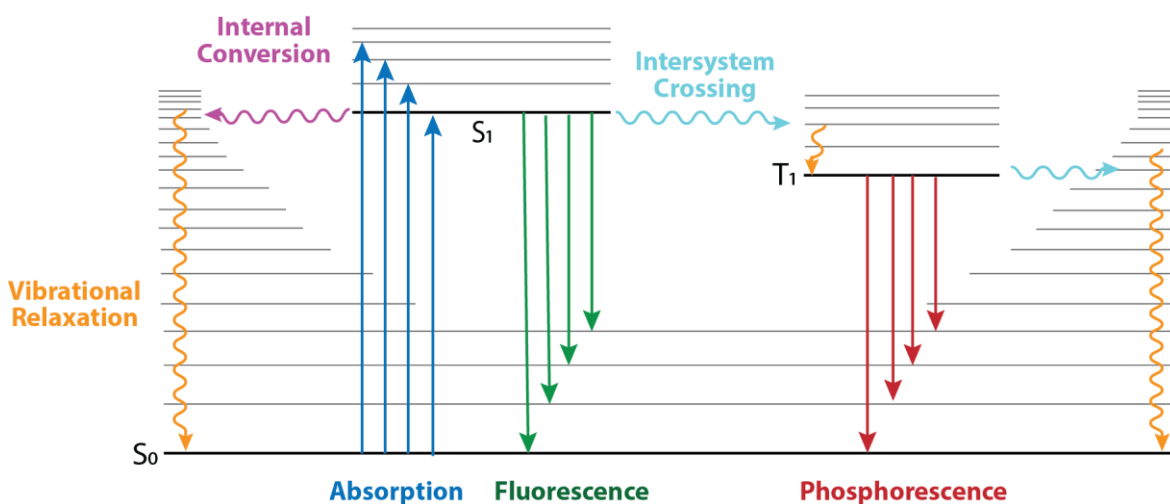


**Figure 1.1. Jablonski diagram.** This diagram shows the energetic relationship and the nonradiative and radiative pathways for a standard molecule.

### 1.3. What is NIR/SWIR and Why Do We Care?

The near infrared and shortwave infrared are sections of the electronic spectrum beyond the visible light spectrum (800-1000 nm for NIR I and 1000-2000 nm for SWIR, Figure 1.2a). This region is deemed “spectrally quiet” in that there are fewer compounds that absorb and emit light compared to the bluer (higher energy, shorter wavelength) visible spectrum where most molecules interact with light. Beyond the SWIR, i.e., the redder (lower energy, longer wavelength) infrared spectrum contains significant spectral congestion due to absorption by vibrational motions of molecules. Another factor is that light scattering is wavelength dependent. For example, dilute gas shows an

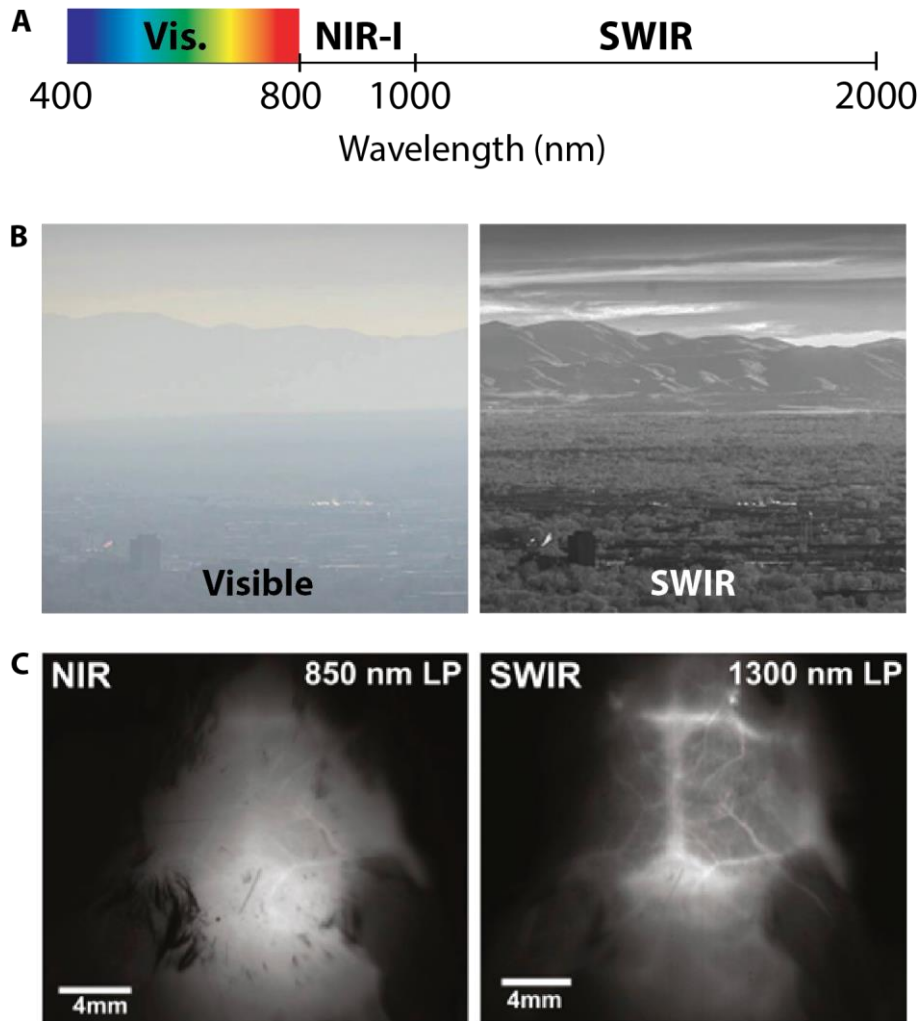


**Figure 1.2. Definition and applications of shortwave infrared light.** (a) Line chart defining NIR-I and shortwave infrared portion of the electromagnetic spectrum. (b) SWIR camera can resolve mountains on a foggy day. Adapted from laserfocusworld.com.<sup>5</sup> (c) SWIR light shows better vascular definition through a mouse skull using indocyanine green as the fluorescent dye. Adapted from Carr *et al.*<sup>3</sup>

inverse quartic relationship of scattering with wavelength (Rayleigh scatter). These factors make the NIR and SWIR sections of light of interest in both biological imaging<sup>1-3</sup> and satellite telemetry<sup>4,5</sup>, especially through inclement weather and foliage (Figure 1.2). In order to put these applications into practice one needs to have fluorescent materials (fluorophores) and photodetectors that can efficiently emit and accept light, respectively. In this thesis, I will use fundamental photophysics to evaluate and model SWIR fluorophores.

## 1.4. Photophysical Figures of Merit for Imaging: Quantum Yield and

### Brightness

To evaluate the effectiveness of fluorophores, I use quantum yield of fluorescence and brightness. Quantum yield of fluorescence,  $\phi_F$ , can most simply be defined as the ratio of the photons emitted over the total photons absorbed:

$$\phi_F = \frac{\textit{Photons emitted}}{\textit{Photons absorbed}}. \quad (\text{Eq.1.1})$$

Knowing that every photon absorbed needs to be emitted or transferred into other energy, one can think of the total photons absorbed as equivalent to a sum of radiative and nonradiative rates. From here, one can convert quantum yield of fluorescence,  $\phi_F$ , into a rate of emission,  $k_r$ , divided by the sum of nonradiative and radiative rates,  $k_{nr} + k_r$  :

$$\phi_F = \frac{k_r}{k_r + k_{nr}}. \quad (\text{Eq.1.2})$$

Another common metric for comparison is brightness,  $B$ , which is number of photons emitted when a molecule is excited at a specific wavelength (normalized for volume and concentration). Brightness,  $\Omega$ , is more colloquially defined as the product of the quantum yield,  $\phi_F$ , and the molar absorption coefficient,  $\epsilon$ :

$$\Omega = \frac{\textit{Photons emitted}}{\textit{Photons absorbed}} \times \frac{\textit{photons absorbed}}{\textit{path length} \times \textit{concentration}} = \phi_F \times \epsilon. \quad (\text{Eq.1.3})$$

## 1.5. Qualitative Relationship Between Energy Gap and Quantum Yield into

### SWIR

With the creation of NIR and SWIR dyes, quantum yields were observed to decline with redder fluorescence energy. This trend overall applies to inorganic materials like quantum dots

(Figure 1.3a).<sup>6</sup> Additionally, a qualitative inverse relationship for organic chromophores into the NIR has been shown for both quantum yield and brightness (Figure 1.3bc).<sup>7</sup> In this example across many dye types, it was demonstrated that around 700 nm there is a steep change in quantum yields, with pyrrolopyrrole cyanine dyes overall performing better in the NIR. Additionally, brightness does not seem to drop off substantially until 800 to 850 nm, though one can clearly see a drop off

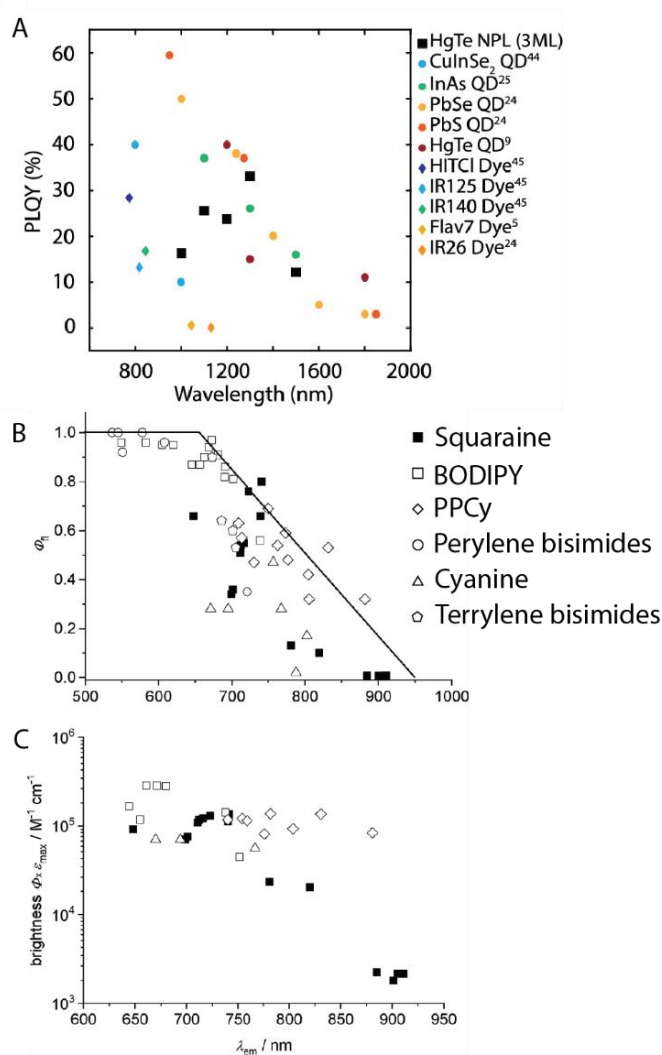


**Figure 1.3. Literature results showing energy gap with quantum yield and brightness.** (a) Photoluminescence quantum yield versus wavelength for quantum dots. Reproduced from Tenney *et al.*<sup>6</sup> (b) Fluorescence quantum yield compared to wavelength of emission. (c) Brightness versus wavelength emission energy for a variety of organic scaffolds. Figures b and c are reproduced from Mayerhoffer *et al.*<sup>7</sup>

around 750 for squaraine dyes (black squares) in the brightness metric (Figure 1.3c). With respect to brightness, newer organic dyes have brightness on the order of  $1 \times 10^3 \text{ M}^{-1} \text{ cm}^{-1}$  or less for dyes that emit past 1000 nm. This begs the question: *Is there a relationship between energy gap  $E_g$  and quantum yield/brightness?* The rest of this chapter will provide an overview of the derivation of known energy gap laws for radiative and nonradiative rates which will be combined into an energy gap law for quantum yield in Chapter 2:

$$\phi_F(E_g) = \left( 1 + K \frac{C^2}{n\mu_{21}^2 (E_M E_g^7)^{\frac{1}{2}}} \exp \left[ -\frac{E_g}{E_M} \left( \ln \frac{2E_g}{\gamma_M E_{ST}} - 1 \right) \right] \right)^{-1}. \quad (\text{Eq.1.4})$$

We will define each term in Chapter 2, but this gives the general form. This equation reveals that quantum yield quasi-exponentially decays with the energy gap of the transition ( $E_g$ ). This thesis will focus on the application of these laws to organic chromophores. In Chapter 2, I apply radiative and nonradiative energy gap laws to the quantum yields of polymethine dyes, a type of organic chromophore characterized by its near “particle in a box” properties.<sup>8</sup> I further use these energy gap laws to define useful parameters to improve quantum yields. Chapter 3 discusses more generally how brightness is affected by different molecular parameters. Chapter 4 tests assumptions made in the combined energy gap law to novel molecules and different solvent environments and Chapter 5 is a brief summary of the current state of the field of SWIR fluorophores.

## 1.6. Probability of Transition: Fermi’s Golden Rule

To understand the fundamental photophysics of fluorophores, one needs to mathematically define radiative and nonradiative rates. The transition rate for both absorption, emission, and some

nonradiative rates can be defined through Fermi's golden rule, which is the generalized first-order correction to time-dependent perturbation theory<sup>9</sup>:

$$\Gamma_{i \rightarrow f} = \frac{2\pi}{\hbar} |\langle f | H' | i \rangle|^2 \rho(E_f), \quad (\text{Eq.1.5})$$

where the matrix element  $|\langle f | H' | i \rangle|^2$  defines the overlap of the final wavefunction with a perturbed initial wavefunction, and  $\rho(E_f)$  is the density the states that couple ground and excited wavefunctions. When both the initial and final state are in the electronic manifold, this describes radiative or absorption events where the matrix element is the transition dipole moment (for dipole allowed transitions) which determines the strength of the transition. For nonradiative rates from internal conversion or intersystem crossing, the matrix element is based on vibrational coupling. I will use Fermi's golden rule throughout the discussion of radiative and nonradiative rates.

## 1.7. Primer on Radiative Rate Energy Gap Law

Understanding the relationship between absorption and emission of light goes back to the early 20<sup>th</sup> century, when Einstein developed the theory of atomic spectral lines.<sup>10</sup> He related the rate of absorption,  $B_{12}$ , to the rate of spontaneous emission,  $A_{21}$ , and the rate of stimulated emission,  $B_{21}$ , for individual particles in the gas phase, as shown below:<sup>10,11</sup>

$$B_{12}^E N_1 u(E) = B_{21}^E N_2 u(E) + A_{21} N_2, \quad (\text{Eq.1.6})$$

where  $u(E)$  is the energy density of radiation per unit energy, and  $N_1$  and  $N_2$  are the populations of molecules in  $\psi_1, S_0$ , and  $\psi_2, S_1$ , respectively. Following Einstein's<sup>10</sup> and Planck's<sup>12</sup> logic, to solve for spontaneous emission,  $A_{21}$ , one can utilize the energy density of blackbody radiation as well as relate  $B_{12}$  to an experimentally accessible molar absorption coefficient,  $\epsilon$  (full derivation of these steps is available in Section 2.5b) to reach:



$$A_{21} = \frac{g_1}{g_2} \frac{E_g^2 n^2}{\hbar^3 \pi^2 c^2} \sigma_0 = \frac{g_1}{g_2} \frac{1000 E_g^2 n^2}{N_A \log_{10}(e) \pi^2 \hbar^3 c^2} \int_{E_1}^{E_2} \epsilon(E) dE, \quad (\text{Eq.1.7})$$

where  $\frac{g_1}{g_2}$  is the ratio of degenerate states,  $E_g$  is the energy gap,  $\sigma_0$  is the integrated absorbance cross section,  $N_A$  is Avogadro's number,  $\hbar$  is Planck's constant divided by  $2\pi$ ,  $c$  is the speed of light in a vacuum, and  $n$  is the refractive index of the solvent. Within this thesis, I used an adaptation of the atomic based solution to Einstein's  $A_{21}$  coefficient. Since molecules have differences in absorption and emission energy, a treatment of Einstein's  $A_{21}$  coefficient was derived to account for the spectral shift by Strickler and Berg:<sup>13</sup>

$$\begin{aligned} A_{21} &= 2.88 \times 10^{-9} n^2 \langle \tilde{\nu}_f^{-3} \rangle^{-1} \frac{g_1}{g_2} \int_{\omega_1}^{\omega_2} \epsilon(\tilde{\nu}) d\ln(\tilde{\nu}) \\ &= \frac{8 \times 1000 \pi c n^2}{N_A \log_{10} e} n^2 \langle \tilde{\nu}_f^{-3} \rangle^{-1} \frac{g_1}{g_2} \int_{\omega_1}^{\omega_2} \epsilon(\tilde{\nu}) d\ln(\tilde{\nu}). \end{aligned} \quad (\text{Eq.1.8})$$

The energy that defines the rate of absorption,  $B_{12}$  is different than the energy of emission for  $A_{21}$  due to molecular vibrational displacements. Thus, two frequencies instead of one (eq 1.7) encompass the relevant photophysics for molecules, the mean vibrational frequency of fluorescence,  $\langle \tilde{\nu}_f^{-3} \rangle^{-1}$ , and the vibrational frequency of absorbance,  $\tilde{\nu}$ .

In this dissertation, I will use energy gap relationships for both radiative and nonradiative rates of organic molecules to understand general trends of quantum yield and brightness. For expedience in combining radiative and nonradiative rate energy gap laws, I used equation 1.7 (thus  $E_g$  which is defined as the midpoint between the absorption and emission energy). This assumption works well for organic molecules with little difference in maximum absorption and emission energy and allows one to use both absorption and emission band gaps on a consistent basis. Future

work should further analyze the impact of this choice and if there is a more appropriate way to include the vibronic displacement (eq. 1.8) within the radiative rate law.

Although the molar absorption coefficient is how chemists measure the strength of absorption of a molecule, the transition dipole moment,  $\mu_{12/21}$ , is the quantum mechanical based molecular parameter that sets the strength of absorption and emission for dipole allowed transitions. I apply a treatment of Fermi's golden rule (Eq 1.5) for  $A_{21}$ . In free space,  $\rho(E_g)$ , can be calculated by computing the number of photon modes in a cavity of volume  $V_0$ :

$$\rho(E_g) = \frac{E_g^2 V_0 n^3}{\pi^2 \hbar^2 c^3}. \quad (\text{Eq.1.9})$$

For a randomly oriented dipoles in free space, the transition matrix is:

$$|\langle f | H' | i \rangle|^2 = \frac{1}{3} \mu_{21}^2 \mathcal{E}_{vac}^2, \quad (\text{Eq.1.10})$$

where the magnitude of energy of the fluctuating electric field in a vacuum is defined as:

$$\mathcal{E}_{vac} = \left( \frac{E_g}{2\epsilon_0 V_0} \right)^{\frac{1}{2}}, \quad (\text{Eq.1.11})$$

where  $\epsilon_0$  is vacuum permittivity. Since the photophysics present in this thesis is done in solution, a refractive index correction was added to the permittivity,  $\epsilon = \epsilon_0 n^2$ . Combining equations 1.5, 1.9, 1.10, and 1.11 yields:

$$A_{21} = \frac{4\mu_{21}^2 E_g^3 n}{3\hbar^4 c^3}. \quad (\text{Eq.1.12})$$

This is the radiative rate law that I will be using to evaluate quantum yields with respect to a molecule's energy gap. Thus, there is a cubic relationship between energy gap and radiative rate.

Finally, one can relate the sum of the molar absorption coefficients to the transition dipole moment:

$$\int \epsilon(E) = \frac{\log_{10} e N_A}{1000} \frac{g_2 \pi E_g}{3g_1 \epsilon_0 n \hbar^2 c} |\mu_{21}|^2. \quad (\text{Eq.1.13})$$

This will be important toward relating the calculated quantum mechanical value for absorptivity to the experimentally determined value. This is especially critical for the analysis of brightness of a molecule.

## 1.8. Primer on Nonradiative Rate Energy Gap Law

There are many types of nonradiative rates, such as internal conversion, intersystem crossing, twisted internal charge transfer, and photochemical reactions. For this thesis, I assume that internal conversion is the predominant nonradiative rate in the SWIR (see Chapter 2.3). For this treatment of nonradiative rates, I will focus on Englman and Jortner's formulation of nonradiative rates for internal conversion and intersystem crossing in large molecules as the foundation for the theory behind this portion of the thesis.<sup>14</sup> They first give a general form of nonradiative decay probability derived from Fermi's golden rule:

$$W = \frac{2\pi}{\hbar} \sum_i \sum_j p(si) |V_{si,lj}|^2 \delta(E_{si} - E_{lj}), \quad (\text{Eq.1.14})$$

where:

$$V_{si,lj} \approx CS_{si,lj}, \quad (\text{Eq.1.15})$$

and  $S_{si,lj}$  is the Frank-Condon overlap factor, which reflects the vibrational overlap between states. The value  $C$  is known as the non-adiabatic derivative coupling, which mixes electronic and nuclear states causing the breakdown of the Born-Oppenheimer approximation.  $C$  depends on whether one is analyzing internal conversion or intersystem crossing by considering the effects of the nuclear kinetic energy operator. One can think of internal conversion and intersystem crossing

as analogous to the probability of tunneling between the excited state and a highly vibrationally excited ground state.

From here, Englman and Jortner generate two adiabatic potentials, which are defined by the normal coordinate between the two potentials,  $\Delta_j$ , the vibrational energy or frequency,  $\omega_j$ , and the energy gap between the two potentials  $\Delta E$  or  $E_g$  (Figure 1.4).<sup>14</sup> They then simplify by focusing on a combination of 4 limits which are based on mean vibration frequency  $\langle\omega\rangle = N^{-1}\sum_j\omega_j$  and Stokes shift, or difference between the maximum absorption energy and the maximum emission energy,  $E_{ST}$ , which they define as  $E_{ST} = \sum_j\hbar\omega_j\Delta_j^2$ , where  $\frac{1}{2}\Delta_j^2 = S$  or the Huang Rhys factor.<sup>i</sup> The four limits are:

1. High temperature, Strong coupling:

$$\beta\hbar\langle\omega\rangle \ll 1 \text{ and } E_{ST} \gg 2\hbar\langle\omega\rangle \tanh\left(\frac{1}{2}\beta\hbar\langle\omega\rangle\right)$$

2. Low temperature, Strong coupling:

$$\beta\hbar\langle\omega\rangle \gg 1 \text{ and } E_{ST} \gg 2\hbar\langle\omega\rangle \tanh\left(\frac{1}{2}\beta\hbar\langle\omega\rangle\right)$$

3. High temperature, Weak coupling:

$$\beta\hbar\langle\omega\rangle \ll 1 \text{ and } E_{ST} \leq 2\hbar\langle\omega\rangle$$

4. Low temperature, Weak coupling:

$$\beta\hbar\langle\omega\rangle \gg 1 \text{ and } E_{ST} \leq 2\hbar\langle\omega\rangle$$

---

<sup>i</sup>The relationship between the Stokes shift and the Huang Rhys factor has been found to be more complicated in recent years given the impact of temperature on Stokes shift.<sup>92</sup> The difference in energy between each barycenter, intensity weighted average, of absorption and emission defined throughout this thesis as  $E_{bc}$  is unaffected by temperature. This will be discussed further in Chapter 3.

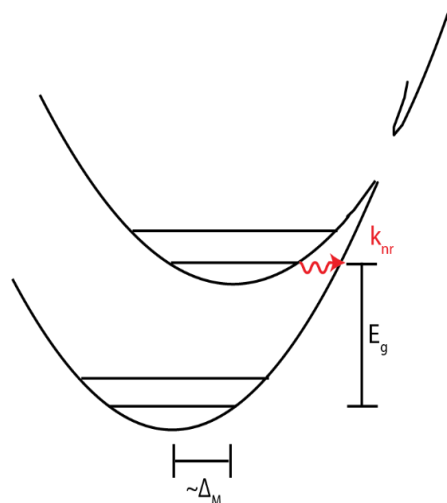


**Figure 1.4. Diagram of displaced harmonic oscillator with an avoided crossing in frequency space.**

In this thesis, I will focus on the low temperature, weak coupling limit which is applicable to typical organic chromophores. To stay outside of the high temperature limit at room temperature or  $\sim 300$  K, the mean vibrational energy would need to be greater than  $\sim 210 \text{ cm}^{-1}$  which is much lower than mean vibrational energy in organic molecules. To be in the weak coupling limit the Stokes shift must be less than twice the mean vibrational frequency  $\langle \omega \rangle$ . Again, in the case of organic molecules, a large density of high frequency modes is responsible for most of the Stokes shift, since Stokes shifts are less than  $1000 \text{ cm}^{-1}$  for most molecules studied here, I assert that most molecules are safely in the weak coupling limit.

For the weak coupling low temperature limit, Englman and Jortner arrive at the following equation in their manuscript:

$$W = \frac{C^2 \sqrt{2\pi}}{\hbar \sqrt{\hbar \omega_M \Delta E}} \exp \left[ -\frac{\Delta E}{\hbar \omega_M} \left( \ln \left( \frac{2\Delta E}{d\hbar \omega_M \Delta_M^2} \right) - 1 \right) \right]. \quad (\text{Eq.1.16})$$

$\Delta E$  is the fluorescence energy plus half the Stokes shift, or as defined in this dissertation  $E_g$ ;  $\omega_M$  is the maximum vibrational stretch;  $d$  is the number of degenerate stretches; and  $\Delta_M^2$  is the displacement from the maximum vibrational stretch. The maximum vibrational stretch is considered of most importance here since this nonradiative pathway is between the lowest vibrational level of the excited state to an energetically well matched upper vibrational level of the ground state (Figure 1.4). Thus, the larger vibrational stretch represents the closest approach between the ground and excited state, though edge cases have computationally been analyzed elsewhere.<sup>15</sup> An adaptation of this equation is used as the nonradiative energy gap law in this dissertation and is discussed further in Chapter 2. This energy gap law has been applied to many systems including gold nanoclusters<sup>16</sup>, metal to ligand charge transfer complexes,<sup>17,18</sup> aromatic thiones,<sup>19</sup> and platinum coated conjugated polymers.<sup>20</sup> Englman and Jortner proposed that deuteration of a compound (by changing  $\omega_M$ ) is a method to improve quantum yield without significantly altering the energy gap. This approach has previously been reported<sup>21-23</sup> and will be discussed throughout the dissertation.

In conclusion, the combined energy gap law at the focus of my thesis can be derived by inserting equations 1.12 and 1.16 into equation 1.2. This law will be tested with the polymethine chromophore class in Chapter 2. In Chapter 3, I recontextualize these laws in terms of brightness. In Chapter 4, I initiated methodologies to elucidate other photophysical pathways that were not included in the energy gap laws and apply these to new chromophore classes. In Chapter 5, I give a brief outlook on future directions in SWIR photophysics. Applications of this approach will enable better design of dyes through understanding the interplay between a molecule's structure and its photophysical properties, especially in the near and shortwave infrared.

## Chapter 2

# Establishing Design Principles for Emissive Organic SWIR

## Chromophores from Energy Gap Laws

Adapted with permission from: Friedman, H. C., Cosco, E.M., Atallah, T.L., Sletten, E.M., Caram, J. R., “Establishing design principles for brightly emissive organic SWIR emitters” *Chem.* 7(12). 3359-3376. (2021). Copyright 2021 Elsevier Inc.

### 2.1. Introduction

Shortwave infrared (SWIR, or NIR-II/III, ~1000–2000 nm) radiation offers imaging capabilities with superlative contrast and feature resolution. Reflective and fluorescent imaging in the SWIR has been shown to enable penetrative imaging—through fog, foliage, skin and bone,<sup>2,24,25</sup> enabling broad applications ranging from image-guided surgery to self-driving cars.<sup>1,4,26,27</sup> The SWIR spectral region has lower background due to few natural sources of radiation (e.g., blackbody radiation, tissue autofluorescence), compared to the visible (VIS, 350–700 nm) and near-infrared (NIR, 700–1000) regions. Expanding and improving the library of bright SWIR chromophores that can sense biological, chemical or physical changes in complex and opaque environments represents a fundamental technological aim.

While nanoscale emitters like quantum dots and lanthanide nanoparticles can achieve high quantum yields ( $\phi_F > 0.1$ ) in the SWIR, organic chromophores have thus far displayed very low emission past 1000 nm ( $\phi_F \leq 0.03$ ).<sup>28–32</sup> Nevertheless, organic emitters are biocompatible and provide a breadth of chemical functionalities that make them highly desirable for biological applications.<sup>33</sup> There is a clear trade-off between smaller HOMO-LUMO gaps and  $\phi_F$ . Even

among NIR/SWIR emitters, the higher  $\phi_F$  dyes tend to be those with maximum absorption wavelength ( $\lambda_{max}$ ) on the blue edge of the SWIR spectral window. In this manuscript, we apply experiment and theory to answer the questions: *What dictates fundamental limits on  $\phi_F$  for narrow HOMO-LUMO gaps? Can we compare enhancement of  $\phi_F$  due to a structural change between chromophores, independent of energy gap changes? What additional structural parameters provide a handle to overcome the current limits on  $\phi_F$ ?*

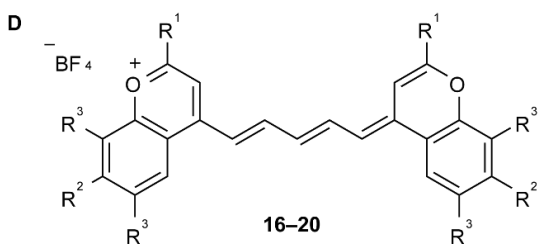
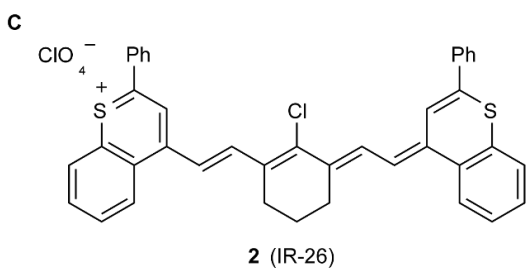
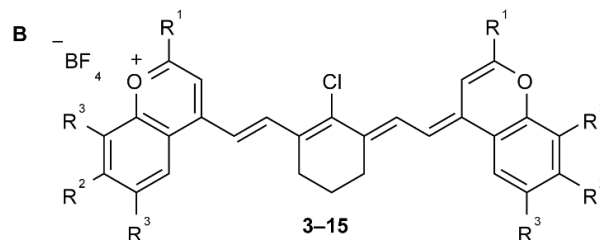
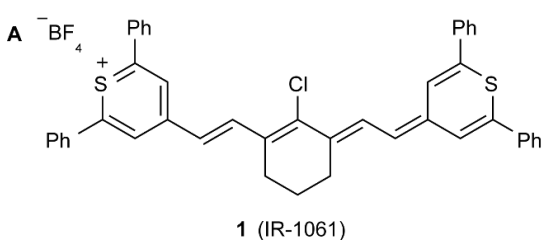
To address these questions, we must consider how the energy gap modulates the fluorescence quantum yield, or the ratio of the radiative rate ( $k_r$ ) to the sum of radiative rate and nonradiative rate ( $k_{nr}$ ):

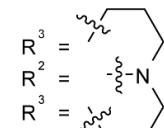
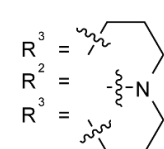
$$\phi_F = \frac{k_r}{k_r + k_{nr}}. \quad (\text{Eq. 2.1})$$

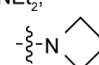
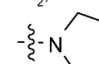
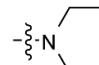
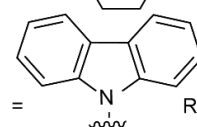
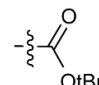
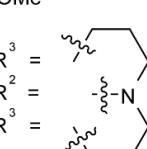
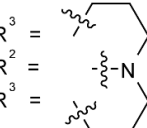
Known energy gap laws modulate the radiative/non-radiative rate, which, when combined with equation 2.1, allow us to derive an estimate of the maximum  $\phi_F$  as a function of singlet energy gap ( $E_g$ ) for any chromophore. This Energy gap law Quantum yield Master Equation (EQME) will allow us to frame changes in  $\phi_F$  in terms of  $E_g$  independent parameters, such as the transition dipole moment ( $\mu_{21}$ ), Stokes shift ( $E_{ST}$ ), and the strength of nonadiabatic coupling between excited and ground states ( $C$ ).

To parametrize and assess EQME, we utilize absorption cross sections, fluorescent spectra, excited state decay rates and quantum yields for 21 related symmetric polymethine fluorophores with absorption maxima ranging from 800–1100 nm (Figure 2.1).<sup>34,35</sup> This unique data set was acquired using sensitive superconducting nanowire single photon detectors (SNSPDs) which are capable of probing the often short excited state lifetimes of these chromophores in the SWIR, beyond the bandgap of silicon avalanche photodiodes (details in Chapter 2.5).<sup>35–37</sup>





Compound	R <sup>1</sup>	R <sup>2</sup>	R <sup>3</sup>
17 (Flav5),	R <sup>1</sup> = Ph;	R <sup>2</sup> = NMe <sub>2</sub> ;	R <sup>3</sup> = H
18 (Chrom5),	R <sup>1</sup> = <i>t</i> Bu;	R <sup>2</sup> = NMe <sub>2</sub> ;	R <sup>3</sup> = H
19,	R <sup>1</sup> = 1-adamantyl;	R <sup>2</sup> = NMe <sub>2</sub> ;	R <sup>3</sup> = H
20 (JuloFlav5),	R <sup>1</sup> = Ph;		
21 (JuloChrom5),	R <sup>1</sup> = <i>t</i> Bu;		

Compound	R <sup>1</sup>	R <sup>2</sup>	R <sup>3</sup>
3 (Flav7),	R <sup>1</sup> = Ph;	R <sup>2</sup> = NMe <sub>2</sub> ;	R <sup>3</sup> = H
4 (IR-27),	R <sup>1</sup> = Ph;	R <sup>2</sup> = H;	R <sup>3</sup> = H
5,	R <sup>1</sup> = 1-adamantyl;	R <sup>2</sup> = NMe <sub>2</sub> ;	R <sup>3</sup> = H
6 (Chrom7),	R <sup>1</sup> = <i>t</i> Bu;	R <sup>2</sup> = NMe <sub>2</sub> ;	R <sup>3</sup> = H
7,	R <sup>1</sup> = Ph;	R <sup>2</sup> = NEt <sub>2</sub> ;	R <sup>3</sup> = H
8,	R <sup>1</sup> = Ph;		R <sup>3</sup> = H
9,	R <sup>1</sup> = Ph;	R <sup>2</sup> = NPh <sub>2</sub> ;	R <sup>3</sup> = H
10,	R <sup>1</sup> = Ph;		R <sup>3</sup> = H
11,	R <sup>1</sup> = Ph;		R <sup>3</sup> = H
12,	R <sup>1</sup> = Ph;		R <sup>3</sup> = H
13,	R <sup>1</sup> = Ph;		R <sup>3</sup> = H
14 (MeOFlav7)	R <sup>1</sup> = Ph;	R <sup>2</sup> = OMe	R <sup>3</sup> = H
15 (JuloFlav7),	R <sup>1</sup> = Ph;		
16 (JuloChrom7),	R <sup>1</sup> = <i>t</i> Bu;		

<sup>a</sup> counterion = Cl<sup>-</sup>

**Figure 2.1. Chromophores studied in this chapter.** (a/b) Laser dyes IR-1061 (a) and IR-26 (b). (c/d) Flavylium and chromenylium heptamethine (c) and pentamethine (d). fluorophores.

Comparing our results to the quantum yield of an additional 33 reported NIR and SWIR polymethine dyes demonstrates the general applicability of EQME for determining maximum quantum yield for organic chromophores in the SWIR.

The EQME equation also allows us to develop an energy gap independent comparison methodology for SWIR chromophores, enabling practical quantitative exploration how changes within a dye scaffold can lead to improved  $\Phi_F$  independent of shifts in energy. Using this method, we show electron donating groups increase relative quantum yield while redshifting the  $\lambda_{max}$  for the flavylum polymethine scaffold, a relationship previously obscured due to redshifting energy gaps. Furthermore, EQME quantifies other avenues for increasing quantum yield, such as deuteration, increasing the transition dipole moment through J-aggregation, or increasing the radiative rate through plasmonic coupling. We experimentally demonstrate such improvement through partial deuteration of the Flav7 (chromophore **3**) scaffold. Our results define a metric and roadmap for overcoming limitations in SWIR quantum yields.

## 2.2. Results

In Figure 2.2, we show an example of the collected data used to define measured values and errors for quantum yield ( $\phi_F$ ),  $\lambda_{max}$ , energy gap ( $E_g$ ), total rate ( $k_{tot}$ ), and Stokes shift ( $E_{ST}$ ). All values are reported, which were taken in dichloromethane, DCM, in Table 2.1 and their measurement and fitting is detailed in Section 2.5a. For all derived values, we will use SI units, however the tables will report values in more conventional wavenumber units ( $\text{cm}^{-1}$ ). For convenience, the values in Table 2.1 can be used in each equation by converting to joules i.e., multiplying by  $\alpha_E = 10^2 hc \frac{\text{J}}{\text{cm}^{-1}}$  or  $1.986 \times 10^{-23} \frac{\text{J}}{\text{cm}^{-1}}$ .  $E_g$  is defined as  $\frac{hc}{\lambda_{max}} - \frac{1}{2} E_{ST}$  (Figure 2.2a). From the values in Table 2.1, we calculate the radiative and nonradiative rates ( $k_r$  and  $k_{nr}$

respectively), oscillator strengths of absorption and emission ( $f_{12}$  and  $f_{21}$ ), and the excited to ground transition dipole moment ( $\mu_{21}$ ,  $\mu'_{21}$ ), calculated from the emission lifetime and absorption cross section, respectively (Table 2.2). The procedure for calculating these parameters is described in Chapter 2.5b.

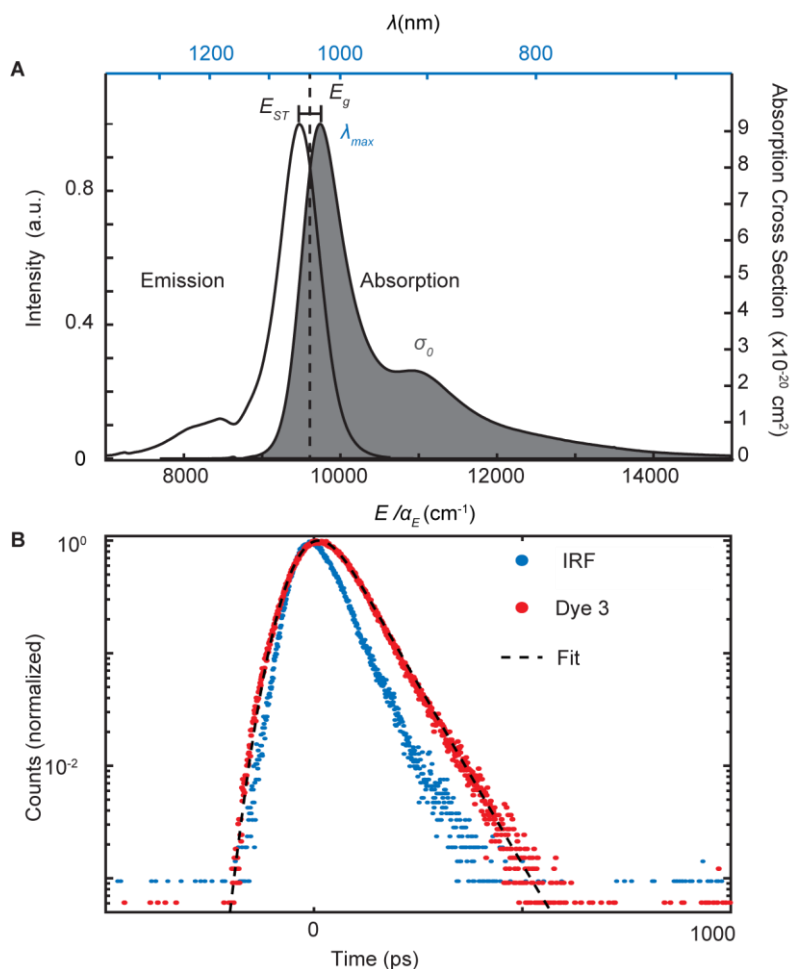


**Figure 2.2. Representative plots of photophysical measurements used to determine energy law constants.** (a) Absorption and emission spectra for dye **3** (Flav7) in dichloromethane is plotted.  $\lambda_{max}$  is defined as the maximum absorption point, the  $E_{ST}$  is defined as the difference between absorption and emission maxima and  $\sigma_0$  is the integrated absorption cross section.  $E_g$  is the midpoint between maximum absorption and emission values. (b) Fluorescent lifetime measurement for **3**, instrument response function (IRF), and the data fit curve.

**Table 2.1. Experimentally Derived Values for the Energy Gap Laws**

<b>Dye</b>	$\Phi_F$ ( $\times 10^{-2}$ )	$\frac{E_g}{\alpha_E}$ ( $\text{cm}^{-1}$ )	$\lambda_{max}$ ( $\text{nm}$ )	$k_{tot}$ ( $\times 10^8 \text{ s}^{-1}$ )	$\sigma_0$ ( $\times 10^{-39} \text{ m}^2$ )	$\frac{E_{ST}}{\alpha_E}$ ( $\text{cm}^{-1}$ )
<b>1</b>	$0.32 \pm 0.01$	9276	1063	$147 \pm 2$	$3.25 \pm 0.03$	258.2
<b>2</b>	$0.05 \pm .03$	9107	1080	$490 \pm 20$	$2.35 \pm 0.04$	298.7
<b>3</b>	$0.61 \pm 0.02$	9603	1027	$147 \pm 2$	$2.68 \pm 0.01$	267.7
<b>4</b>	$0.35 \pm 0.01$	10011	987	$192 \pm 4$	$2.37 \pm 0.04$	240.5
<b>5</b>	$1.61 \pm 0.02$	10148	975	$66.2 \pm 0.4$	$2.63 \pm 0.05$	216.3
<b>6</b>	$1.70 \pm 0.04$	10128	977	$68.6 \pm 0.5$	$2.58 \pm 0.03$	215.4
<b>7</b>	$0.62 \pm 0.02$	9560	1033	$144 \pm 2$	$2.07 \pm 0.07$	237.7
<b>8</b>	$0.51 \pm 0.02$	9585	1029	$160 \pm 3$	$2.86 \pm 0.05$	266.37
<b>9</b>	$0.58 \pm 0.02$	9414	1047	$147 \pm 2$	$2.76 \pm 0.01$	274.7
<b>10</b>	$0.48 \pm 0.02$	9548	1034	$151 \pm 2$	$2.91 \pm 0.01$	246.1
<b>11</b>	$0.54 \pm 0.01$	9571	1030	$151 \pm 2$	$2.48 \pm 0.09$	274.8
<b>12</b>	$0.45 \pm 0.01$	9668	1021	$161 \pm 3$	$1.46 \pm 0.08$	252.3
<b>13</b>	$0.42 \pm 0.02$	9902	998	$169 \pm 3$	$1.16 \pm 0.02$	235.3
<b>14</b>	$0.52 \pm 0.01$	10042	984	$155 \pm 2$	$2.03 \pm 0.03$	242.0
<b>15</b>	$0.46 \pm 0.01$	9308	1061	$180 \pm 3$	$2.59 \pm 0.02$	233.9
<b>16</b>	$1.58 \pm 0.02$	9814	1007	$84.7 \pm 0.7$	$2.51 \pm 0.05$	240.1
<b>17</b>	$6.1 \pm 0.1$	11468	862	$32.2 \pm 0.1$	$3.20 \pm 0.04$	276.9
<b>18</b>	$28 \pm 2$	12086	819	$9.79 \pm 0.01$	$3.46 \pm 0.05$	248.3
<b>19</b>	$28.3 \pm 0.5$	12077	819	$9.49 \pm 0.01$	$2.83 \pm 0.05$	262.6
<b>20</b>	$5.3 \pm 0.02$	10980	897	$33.8 \pm 0.1$	$2.66 \pm 0.03$	337.5
<b>21</b>	$18.3 \pm 0.4$	11602	852	$13 \pm 0.1$	$3.67 \pm 0.03$	269.2
<b>3'</b>	$0.63 \pm 0.03$	9626	1027	$141 \pm 2$	$4.35 \pm 0.07$	267.7
<b>3''</b>	$0.66 \pm 0.05$	9626	1027	$139 \pm 2$	$4.40 \pm 0.12$	267.7

<b>Table 2.2. Calculated Values for Dyes Studied</b>						
<b>Dye</b>	$k_r$ (eq 2.1) ( $\times 10^7 \text{s}^{-1}$ )	$k_{nr}$ (eq 2.1) ( $\times 10^8 \text{s}^{-1}$ )	$f_{12}$	$f_{21}$	$\mu'_{21}$ (eq 2.4) ( $D$ )*	$\mu_{21}$ (eq 2.3) ( $D$ )
<b>1</b>	4.7 ± 0.2	147 ± 5	2.09 ± 0.02	-0.58 ± 0.02	17 ± 1	11.5 ± 0.2
<b>2</b>	2.4 ± 1.4	476 ± 286	1.51 ± 0.03	-0.30 ± 0.18	15 ± 1	8.4 ± 3.0
<b>3</b>	9.0 ± .03	146 ± 5	1.72 ± 0.01	-1.02 ± 0.04	15 ± 1	15.0 ± 0.3
<b>4</b>	6.7 ± 0.2	192 ± 7	1.50 ± 0.02	-0.71 ± 0.02	14 ± 1	12.3 ± 0.3
<b>5</b>	10.6 ± 0.3	67 ± 2	1.69 ± 0.03	-1.14 ± 0.01	15 ± 1	15.4 ± 0.1
<b>6</b>	11.6 ± 0.3	65 ± 1	1.66 ± 0.02	-1.16 ± 0.03	15 ± 1	15.6 ± 0.2
<b>7</b>	9.0 ± 0.3	144 ± 5	1.33 ± 0.05	-1.04 ± 0.04	14 ± 1	15.2 ± 0.1
<b>8</b>	8.2 ± 0.2	160 ± 7	1.66 ± 0.01	-0.95 ± 0.04	15 ± 1	14.5 ± 0.4
<b>9</b>	8.5 ± 0.3	146 ± 5	1.59 ± 0.06	-1.02 ± 0.04	15 ± 1	15.2 ± 0.3
<b>10</b>	7.3 ± 0.3	151 ± 7	1.77 ± 0.01	-0.84 ± 0.04	16 ± 1	13.7 ± 0.4
<b>11</b>	8.2 ± 0.2	151 ± 4	1.88 ± 0.01	-0.94 ± 0.02	16 ± 1	14.5 ± 0.2
<b>12</b>	7.3 ± 0.2	161 ± 4	0.94 ± 0.05	-0.82 ± 0.02	11 ± 1	13.4 ± 0.2
<b>13</b>	7.2 ± 0.4	172 ± 9	0.74 ± 0.02	-0.78 ± 0.04	10 ± 1	12.9 ± 0.4
<b>14</b>	8.1 ± 0.2	155 ± 4	1.31 ± 0.01	-0.85 ± 0.02	13 ± 1	13.4 ± 0.2
<b>15</b>	8.2 ± 0.3	178 ± 5	1.84 ± 0.03	-1.00 ± 0.03	16 ± 1	15.2 ± 0.4
<b>16</b>	13.4 ± 0.6	83.4 ± 4	1.61 ± 0.03	-1.47 ± 0.08	15 ± 1	17.8 ± 0.5
<b>17</b>	19.7 ± 0.8	30 ± 1	2.05 ± 0.03	-1.66 ± 0.03	19 ± 1	17.5 ± 0.2
<b>18</b>	27.4 ± 0.5	7.0 ± 0.3	2.23 ± 0.03	-2.03 ± 0.14	19 ± 1	18.9 ± 0.8
<b>19</b>	26.8 ± 0.4	6.8 ± 0.1	1.82 ± 0.03	-1.95 ± 0.02	17 ± 1	18.5 ± 0.2
<b>20</b>	18.0 ± 0.8	32 ± 1	1.71 ± 0.01	-1.49 ± 0.01	17 ± 1	17.0 ± 0.1
<b>21</b>	24.3 ± 0.5	10.8 ± 0.02	2.35 ± 0.03	-1.91 ± 0.04	20 ± 1	18.7 ± 0.2
<b>3'</b>	8.9 ± 0.5	140 ± 2	1.76 ± 0.02	-1.02 ± 0.06	15 ± 1	15.0 ± 0.4
<b>3''</b>	9.2 ± 0.7	138 ± 2	1.78 ± 0.05	-1.06 ± 0.08	15 ± 1	15.3 ± 0.6
<b>*For 1–16 (17–21), <math>g_2/g_1 = 1.6 \pm 0.2</math> (<math>1.1 \pm 0.1</math>)</b>						

## 2.2a The First Energy Gap Law – Radiative Rates

The first law relates  $k_r$  to the density of photonic modes in vacuum and the transition dipole moment (details in Chapter 2.5b). Briefly, time dependent perturbation theory results in a spontaneous emission rate:

$$k_r = \frac{2\pi}{\hbar} |M_{21}|^2 g(E_g), \quad (\text{Eq. 2.2})$$

where  $M_{21}$  is the transition integral and  $g(E_g)$  is the density of photon states that bridge the transition energy between ground and excited states (e.g., Fermi's golden rule). In general, as one increases the energy gap, the density of photonic modes increases with  $g(E_g) \propto E_g^2$  while the matrix element that couples a dipole allowed transition between excited and ground state increases with  $|M_{21}|^2 \propto E_g$ , leading to a  $k_r$  which is proportional to  $E_g^3$ . For dipole allowed transitions in a solvent, the precise relationship in SI units is:

$$k_r = \frac{n\mu_{21}^2}{3\pi\epsilon_0\hbar^4c^3} E_g^3, \quad (\text{Eq. 2.3})$$

where  $\epsilon_0$  is the vacuum permittivity, and  $n$  is the refractive index of the solvent ( $n = 1.42$  for dichloromethane).

To assess the validity of the radiative rate energy gap law across different chromophores, we must normalize each rate by the molecule's squared transition dipole moment ( $\mu_{21}^2$ ) as assessed by a *separate measurement*, in this case the integrated absorption cross section:<sup>11</sup>

$$|\mu'_{21}|^2 = 3 \frac{g_1\epsilon_0 n \hbar^2 c}{g_2 \pi E_g} \sigma_0, \quad (\text{Eq. 2.4})$$

where,  $g_2/g_1$  is the ratio of oscillator strength of polymethines of absorption and emission, respectively, or  $-f_{12}/f_{21}$ . We note that in polymethine chromophores, the absorption oscillator

strength depends on the length of the methine bridge. For cyanine dyes with 7 methine units, prior reports show values between 2–3 and with shorter methine bridges values between 1.7–1.9 are reported.<sup>38–40</sup> We therefore use the average values  $g_2/g_1 = 1.6 \pm 0.2$  for 7-methines (**1–16**) and  $1.1 \pm 0.1$  for 5-methines (**17–21**), which though lower show a similar trend.<sup>ii</sup> In Figure 2.3, we plot the radiative rate divided by the transition dipole moment, and compare to the following universal gap law:

$$\frac{k_r}{\mu_{21}^2} = K_\mu \frac{n}{3\pi\epsilon_0\hbar^4 c^3} E_g^3. \quad (\text{Eq. 2.5})$$

Here,  $K_\mu = 1.11 \times 10^{-59} \text{C}^2 \text{m}^2 \text{D}^{-2}$  (a conversion factor which allows us to express  $\mu_{21}$  in more convenient Debye units). We observe that the transition dipole moment normalized radiative rate follows an approximate  $E_g^3$  power law. This is consistent with the change in the density of states as a function of gap.

---

<sup>ii</sup>We note the two primary outliers are **1** and **2** (commercially known as IR-1061 and IR-26). Both dyes have thiochromenylium derived heterocycles. Our results suggest that the presence of sulfur on the heterocycle leads to large deviations in the oscillator strength ratio from changes in  $f_{21}$ .

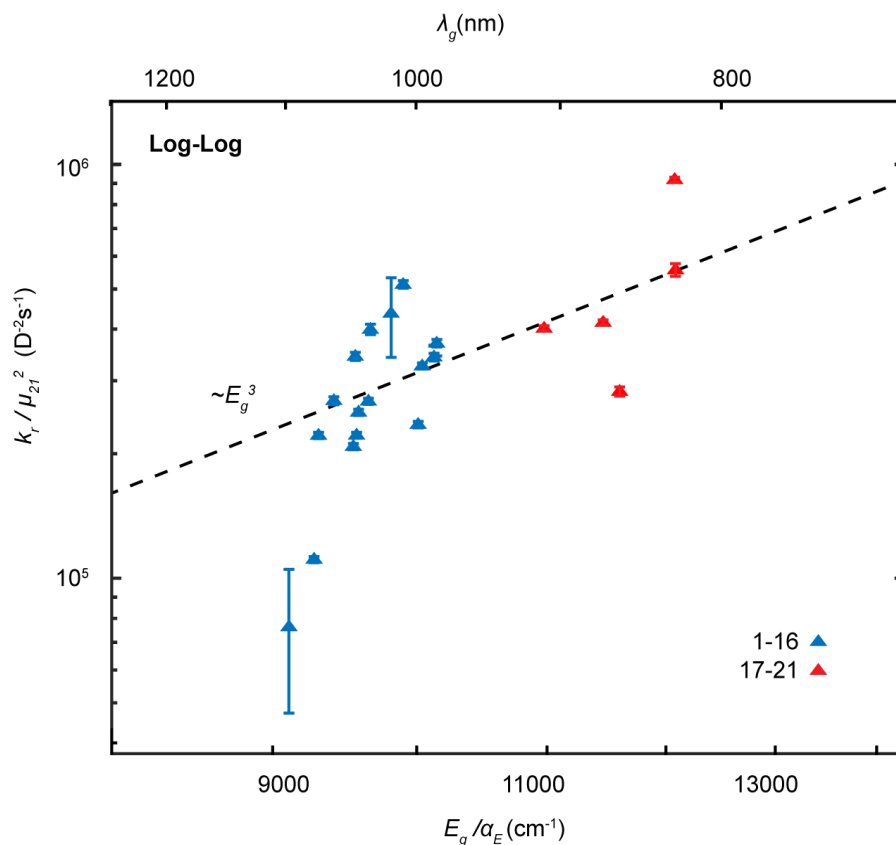


**Figure 2.3. Polymethines follow the radiative rate energy gap law.** Radiative rates from Table 2.2 divided by transition dipole moment from Equation 2.4 for heptamethines (blue) and pentamethines (red). Line represents Equation 2.5, the radiative rate gap law normalized to transition dipole moment, allowing us to compare the dyes independent of the specific molecular parameters.

## 2.2b. The Second Energy Gap Law – Nonradiative Rates

Nonradiative rates are governed by multiple excited state loss channels including internal conversion (decay through vibrational modes), intersystem crossing (decay through an intermediate triplet state), and nuclear reorganization (decay to a lower energy molecular configuration, for example through isomerization or proton transfer).<sup>14,41,42</sup> The *second energy gap law* states that nonradiative relaxation rates for intersystem crossing and internal conversion ( $k_{nr}$ ) exponentially decrease at higher  $E_g$ . Here, we focus on singlet states and thus nonradiative decay



through internal conversion, allowing us to establish a lower bound on  $k_{nr}$  for infrared chromophores.

The experimental values for nonradiative rates are compared to the expression derived by Englman and Jortner,<sup>14</sup> which provides the nonradiative gap law in systems that have small Stokes shifts ( $E_{ST}$ ) relative to their energy gap,  $E_g$ . We present a modified expression below (derived in the Section 2.5c) which relates this equation to values found in Table 2.1:

$$k_{nr} = \frac{C^2 \sqrt{2\pi}}{\hbar \sqrt{E_M E_g}} \exp \left[ -\frac{E_g}{E_M} \left( \ln \left( \frac{2E_g}{\gamma_M E_{ST}} \right) - 1 \right) \right]. \quad (\text{Eq. 2.6})$$

Here,  $C$  is the non-adiabatic coupling term between singlet ground and excited states and  $E_M$  is the energy of the deactivating vibrational mode.  $\gamma_M$  is a parameter representing the degree to which the deactivating mode contributes to the Stokes shift given by:

$$\gamma_M = \frac{SE_M}{E_{ST}}, \quad (\text{Eq. 2.7})$$

where  $S$  is the Huang-Rhys parameter for the collection of near degenerate vibrational modes at or near  $E_M$ . Over the range of energies considered, the nonradiative rate will exponentially decrease with increasing energy gap, as observed in many systems, including gold nanoclusters,<sup>16</sup> metal to ligand charge transfer complexes,<sup>17,18</sup> aromatic thiones,<sup>19</sup> and platinum containing conjugated polymers.<sup>20</sup>

To predict the energy gap dependence of nonradiative rates for polymethine chromophores studied here, we require semi-empirical estimates of  $E_M$ ,  $\gamma_M$ , and  $C$ . For all estimates, we will use the largest Stokes shift for 7-methine dyes in Table 1 (dye **2**,  $E_{ST} = 298.7 \text{ cm}^{-1}$ ).  $E_M$  is the energy of the vibration which contributes most strongly to the tunneling from excited to ground state. While a more detailed derivation is provided in Englman and Jortner's paper,<sup>14</sup> conceptually the gap law arises from the overlap between ground and excited state potentials, which varies

nonlinearly with the vibrational energy. If the energy gap and Stokes shift are fixed, the tunneling distance between potentials decreases with the vibrational curvature (energy) of the mode. In the limit of large  $E_g$  relative to  $E_{ST}$ , higher energy vibrations dominate contributions to the overlap integral between ground and excited states. As Englman and Jortner's paper, we will use  $E_M = 3000 \text{ cm}^{-1}$  for equation 2.7, the approximate energy of the collection of C-H vibrational modes.<sup>14</sup>

In order to reinforce the assumption that the highest frequency vibrational mode would dominate the nonradiative rate, we note the linear change in  $\log(k_{nr})$  as a function of energy gap in Figure 2.4. Despite a large variance in quantum yield among these dyes, this linear trend strongly implies that energy gap law considerations dominate the nonradiative relaxation rates in the SWIR. We plot the nonradiative rate estimate from equation 2.6 using the parameters described in the preceding section ( $E_{ST} = 298.7 \text{ cm}^{-1}$ ,  $C = 1623 \text{ cm}^{-1}$ ), which shows good agreement with the nonradiative rate data. We also perform a linear fit of the data from which we extract the slope, which corresponds to:

$$\frac{d \log(k_{nr})}{dE_g} = -\log(e) \left( \frac{1}{2E'_g} - \frac{\ln\left(\frac{2E'_g}{Y_M E_{ST}}\right)}{E_M} \right). \quad (\text{Eq. 2.8})$$

For simplicity, we will use the midpoint  $E'_g = 10,000 \text{ cm}^{-1}$ , which leads to a fit for the deactivating vibrational mode of  $E_M^{fit} = 4086 \text{ cm}^{-1}$ . Taken together, both the agreement of the model and the slope from the linear fit agree with the apparent dominance of *high-frequency vibrational* modes ( $\geq 3000 \text{ cm}^{-1}$ , i.e., C-H stretches) in setting the non-radiative rate limit in SWIR-emitting polymethines.

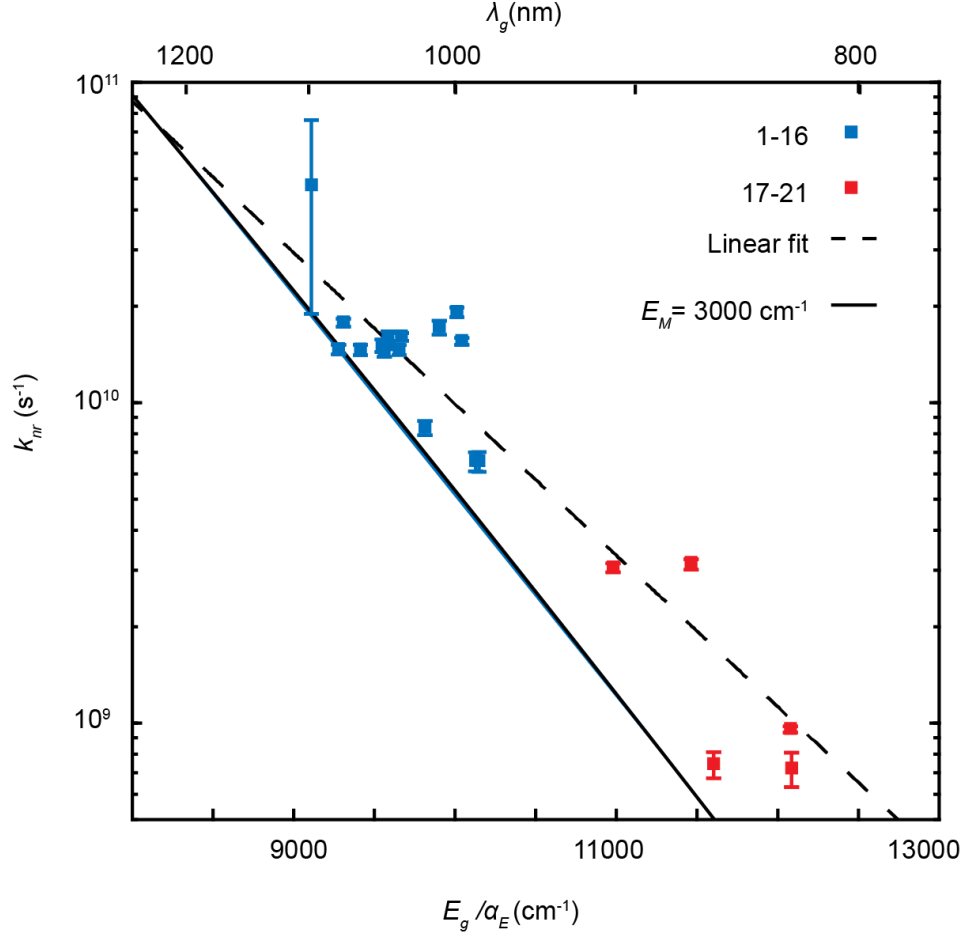


**Figure 2.4.**  $k_{nr}$  are governed by high-frequency vibrational mode  $E_M > 3000 \text{ cm}^{-1}$ . Nonradiative rates from Table 2.2 are plotted against a linear fit for  $\log(k_{nr})$ , and equation 2.6, evaluated using the parameters described in the text.

### 2.2c. Energy Gap Quantum Yield Master Equation

We can combine equations 2.1, 2.3 and 2.6 to derive EQME, which sets the maximum quantum yield of as function of energy gap, dielectric and molecular parameters:

$$\phi_F(E_g) = \left( 1 + K \frac{C^2}{n\mu_{21}^2 (E_M E_g^7)^{\frac{1}{2}}} \exp \left[ -\frac{E_g}{E_M} \left( \ln \frac{2E_g}{\gamma_M E_{ST}} - 1 \right) \right] \right)^{-1}, \quad (\text{Eq. 2.9})$$

where  $K = \left( \frac{3\epsilon_0 c^2}{(2^5 \pi^3)^{1/2}} \right)$ . In Figure 2.5, we plot the functional form of the predicted “highest” quantum yield using  $\gamma_M = 1$ ,  $C_1 = 1623 \text{ cm}^{-1}$ ,  $\mu_{21} = 18 \text{ D}$  and  $E_{ST} = 298.7 \text{ cm}^{-1}$ . We also include a more optimistic limit, using  $C_2 = 798 \text{ cm}^{-1}$  (which approximates a median value for the derivative coupling from literature on polyacenes and polyenes)<sup>43,44</sup> and a smaller coupling to the

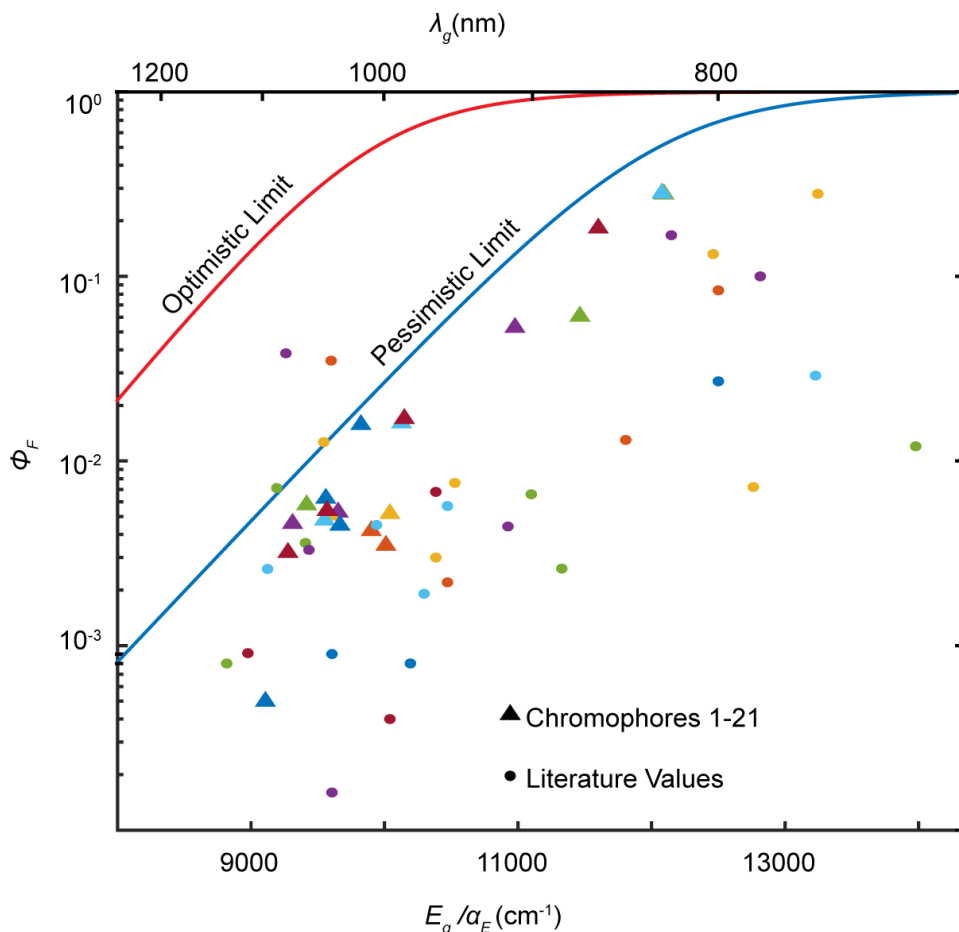


**Figure 2.5. EQME provides consistent upper bounds for SWIR quantum yields.** Comparison of quantum yields of 54 NIR and SWIR polymethine chromophores to the prediction of EQME (Equation 2.9).

high frequency stretches ( $\gamma_M = 0.5$ ) (Figure 2.12 shows effects of changes  $C$  and  $\gamma_M$  independently). We plot both our measured quantum yields from this work and 33 additional dyes from literature reports (see Figure 2.13 for labeled points).<sup>26,33–35,45–51</sup> Our results demonstrate that

even under pessimistic assumptions, quantum yields of almost all observed polymethine dyes do not exceed our predicted maximum line, with an exception of the LZ series of dyes recently reported by Li *et al.*<sup>32,52</sup> Given that our pessimistic estimation likely over-estimates the impact of nonadiabatic coupling, a few outliers can be expected. What is clear is that the model demonstrates that the precipitous falloff in quantum yields around 900 nm is an unavoidable consequence of energy gap laws applied to organic chromophores.

## 2.2d. Comparing Chromophore Quantum Yield while Accounting for Energy Gap Changes

It is challenging to predict how structural modifications of a chromophore will alter the quantum yield. We hypothesize that the dearth of predictive metrics (particularly in the SWIR) arises from the contribution of energy gap QY changes which disguise the underlying effects of molecular change. Using EQME, we can establish an *energy-gap independent* parameter ( $\xi$  or ‘xi’) to study the effect of structural changes on quantum yields within a chromophore family.

We first define a conventional improvement factor ( $\chi$  or ‘chi’) as the fractional change in quantum yield, i.e.,  $\chi = \phi_b/\phi_a - 1$  ( $\chi > 0$  indicates a direct improvement in  $\phi_F$ ). To create an energy gap independent metric, we first note that when  $k_{nr} \gg k_r$  (e.g., when  $\phi_F < 0.1$ ),  $\log(\phi_F)$  is approximately linear with respect to  $E_g$  changes. We therefore can extrapolate  $\phi_F$  of a chromophore at one  $E_g$  to its equivalent value at another point in the SWIR. Comparing the extrapolated quantum yield of the standard fluorophore (**a**) to a second fluorophore (**b**) at the  $E_g$  of **b** gives us an energy-gap independent improvement factor,  $\xi$ .  $\xi$  is defined as:

$$\xi = \frac{\phi_b}{\phi_a} e^{-\kappa(E_b - E_a)} - 1, \quad (\text{Eq. 2.10})$$

where  $\kappa$  is:

$$\kappa = \frac{\ln(2E_{g,a}/\gamma_M E_{ST,a})}{E_M} + \frac{7}{2E_{g,a}}. \quad (\text{Eq. 2.11})$$

$\xi > 0$  indicates an improvement in the quantum yield factoring in the effect of changing the energy gap. The differences between  $\chi$  and  $\xi$  are illustrated in Figure 2.6a; equation 2.11 is derived in section 2.5e of the supporting materials, with Figure 2.14 showing the validity of our constant  $\kappa$ , and section 2.5e.i and Figure 2.15 shows a worked example using  $\xi$ .

<b>Table 2.3. Enhancement of Dyes Compared to Dye 4 (IR-27)</b>		
<b>Dye</b>	<b><math>\xi</math></b>	<b><math>\chi</math></b>
<b>1</b>	1.73	-0.09
<b>2</b>	-0.45	-0.86
<b>3*</b>	1.97	0.74
<b>5</b>	2.75	3.60
<b>6</b>	3.08	3.86
<b>7*</b>	2.47	0.77
<b>8*</b>	1.75	0.46
<b>9*</b>	3.03	0.66
<b>10*</b>	1.73	0.37
<b>11*</b>	1.97	0.54
<b>12</b>	1.14	0.29
<b>13*</b>	0.41	0.20
<b>14*</b>	0.42	0.49
<b>15*</b>	2.75	0.31
<b>16</b>	5.05	3.51
<b>*included in Figure 2.6</b>		

Having established a comparative metric for SWIR fluorophore quantum yield that is independent of energy gap, we compare across heptamethine fluorophores with systematic changes at the 7-position of the flavylium ring (dyes **3, 4, 7–11, 13–15**). Using Equation 2.10, we

computed  $\xi$  values using the unsubstituted IR-27 (**4**) as the comparative fluorophore (i.e., fluorophore **a**). These values are in Table 2.3 (see Figure 2.16 for all values plotted). The  $\xi$  parameter reveals large energy gap independent changes in quantum yield hidden in the direct improvement factor. Using  $\xi$  we sought to correlate the energy gap independent improvement factor with the Hammett  $\sigma_m$  parameter.<sup>53</sup> Prior work demonstrated that the absorption and emission maximum correlated well to  $\sigma_m$  ( $R^2 = 0.96$ ); however, the quantum yield showed no direct correlation.<sup>34</sup> In Figure 2.6b, we show no correlation between  $\sigma_m$  and  $\chi$  (blue line,  $R^2 = 0.015$ ). However, when  $\xi$  is plotted against  $\sigma_m$  values, a linear correlation emerges (Figure 2.6b, red line,  $R^2 = 0.757$ ).

Our results suggest that electron donation enhances the quantum yield. In Figure 2.6c, we show that transition dipole moment,  $\mu_{21}$ , also increases with decreasing  $\sigma_m$  ( $R^2 = 0.452$ ). We therefore hypothesize that electron donating groups appended to the heterocycle functionally increase the delocalization length of the excitation, leading to redshifting chromophores and larger transition dipole moments. The redshift induced by adding electron donating groups would lead to lower quantum yields, but the effect is partially compensated by increasing transition dipole moment, and thus increased quantum yields.

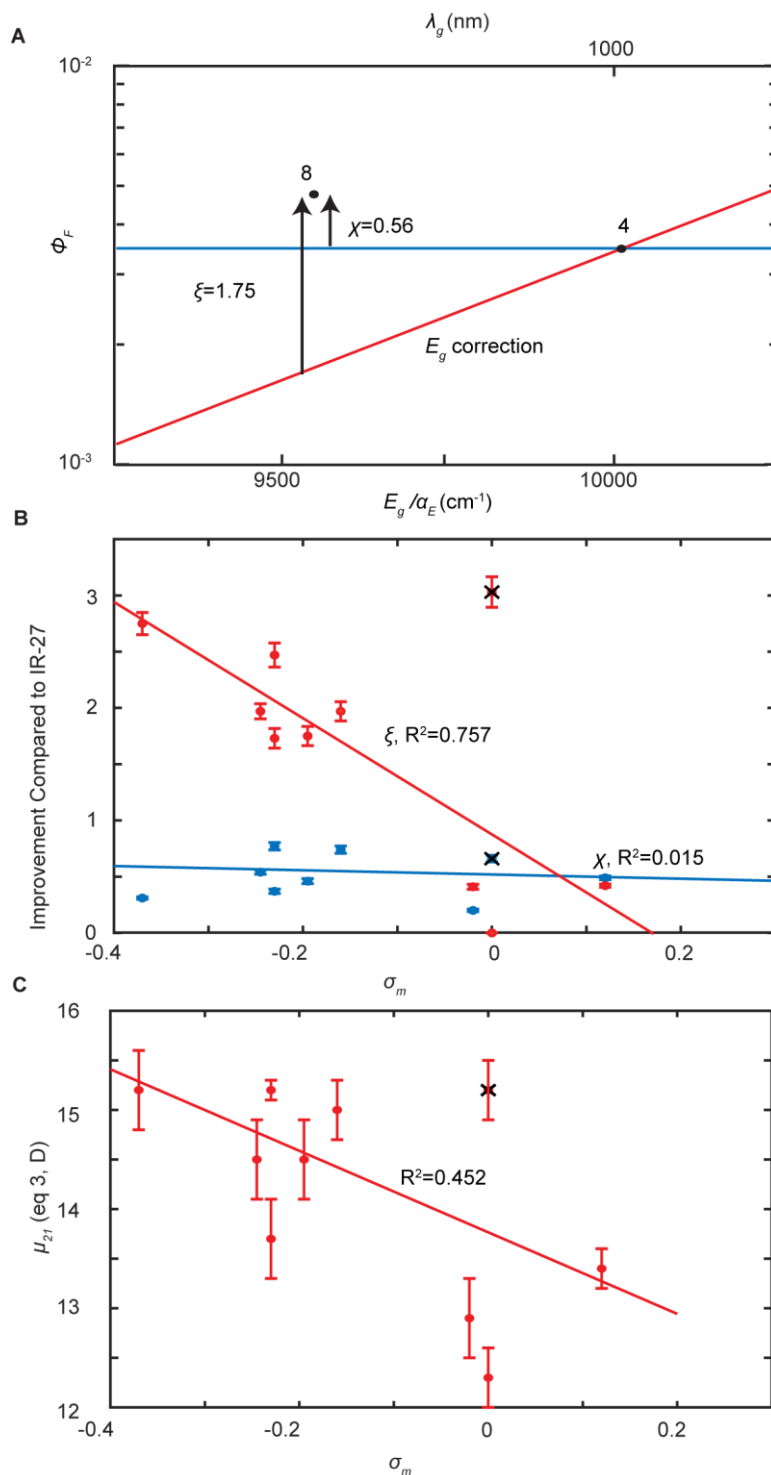


**Figure 2.6. Energy gap free QY comparator,  $\xi$  uncovers a linear free energy relationship.** (a) Example of the difference between  $\xi$  and  $\chi$ . (b)  $\xi$  shows correlation with Hammett parameter while  $\chi$  shows negligible correlation. X through points denotes dye 9 which is excluded from all fits as done in Cosco *et al.*<sup>34</sup> (c) There is a negative correlation between Hammett parameter  $\sigma_m$  and transition dipole moment.



## 2.2e. Overcoming Energy Gap Laws

The EQME suggests pathways to directly improve the quantum yield of organic chromophores through changes in radiative and nonradiative rates (Figure 2.7a). To alter the radiative rate of the chromophore, one can either A) alter the transition dipole moment,  $\mu_{12}$ , or B) control the local photon density of states ( $g(E_g)$ ). For (A), a potential approach is molecular J-aggregation in which coupled chromophores collectively interact with an electric field, resulting in superradiant emission.<sup>54</sup> Furthermore, J-aggregation has the advantage of both modulating the radiative rate and redshifting the absorption and emission. Indeed, several groups have had success in using this strategy to access highly redshifted organic chromophores though superradiance has not been shown.<sup>55,56</sup> Sun et al. demonstrated that FD-1080 J-aggregates when encapsulated in a phospholipid nanoparticle and has a  $\lambda_{max}$  of 1370 nm and a quantum yield of  $5.45 \times 10^{-4}$  compared to the monomer values of 1046 nm and  $\phi_F = 3.1 \times 10^{-3}$  in ethanol.<sup>48,56</sup> The aggregate thus has a  $\chi$  value of -0.8, but a  $\xi$  value of 7.3, again demonstrating that aggregation improved the relative quantum yield when taking into account the energy gap laws. For (B), the most common path discussed is through incorporation of photonic cavities or coupling to plasmonic nanoparticles.<sup>57-59</sup> Historically, microdroplets have been shown to modulate the radiative rate; for

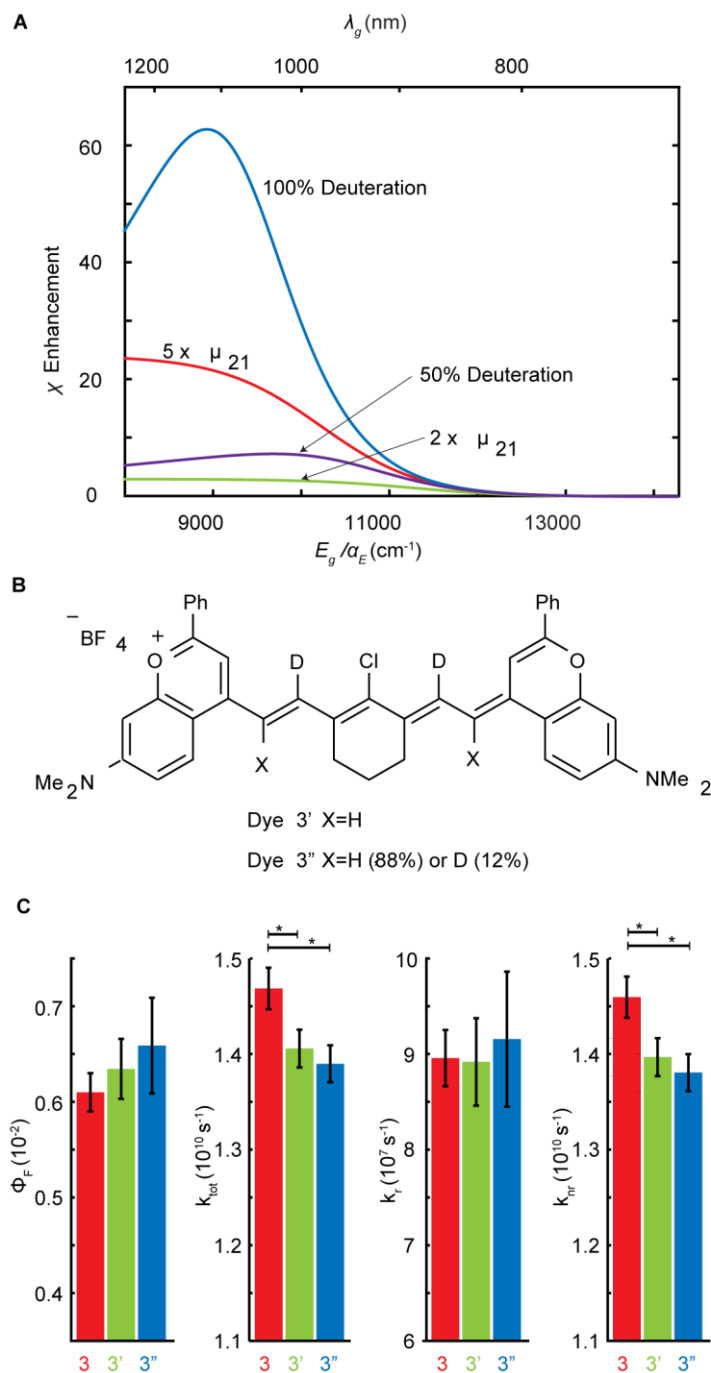


**Figure 2.7. Deuteration and increased transition dipole moment enhances PLQY in SWIR.**

(a) Ratiometric enhancement in quantum yield as a function of energy gap for different strategies for circumventing the energy gap laws including complete deuteration of the alkenyl CH stretches (blue), 50 percent deuteration (purple), increasing the transition dipole moment by 5 and 2 (red and yellow). (b) Structures of dye 3' and 3''. (c) Deuteration on the polymethine scaffold increases but not significantly quantum yield, decreases total rate, has negligible effect on radiative rate, and decreases nonradiative rate. The asterisk indicates that the difference between dyes is significant  $p < 0.05$ .

example, Rhodamine-6G showed an improvement of 2 in smaller droplet compared to larger droplets, including a change in fluorescence rate.<sup>57,58</sup> Srinivasan and Ramamurthy showed that Rhodamine-6G in cermet nanocavities had greater than 50-fold fluorescence enhancement.<sup>60</sup> Though these pathways are promising, the impact of plasmonic/photonic modifications may also simultaneously increase nonradiative rates.<sup>61–63</sup>

For nonradiative rates, the highest vibrational frequency plays a large role in setting  $k_{nr}$ , typically the alkenyl C-H stretch at  $3000\text{ cm}^{-1}$ . Complete substitution of H for D would change the highest vibrational energy to  $2200\text{ cm}^{-1}$ . Assuming no change in the Huang-Rhys parameter ( $S = 0.1$ ) we predict a maximum  $\sim 60$  fold enhancement in quantum yield, using the pessimistic assumptions (Figure 7a,  $\sim 40$  under optimistic assumptions (Figure S9)). Prior work on iridium complexes,<sup>22</sup> benzene,<sup>23</sup> oxazine,<sup>64</sup> and small molecule for blue LEDs<sup>65</sup> also demonstrated increased quantum yields with deuteration suggesting deactivation through these modes is a common feature in chromophores.

To test the effect of deuteration on polymethine chromophores, we synthesized two partially deuterated Flav7 (**3**), derivatives, **3'** and **3''** (structures in Figure 2.7b, synthetic details in Section 2.5f). We hypothesized that partial deuteration will only have a modest effect on the nonradiative rate by decreasing the collective Huang-Rhys parameter of the highest energy mode. Measuring absorption, quantum yield, and time resolved photoluminescence lifetime we observe that dyes **3'** and **3''** have nearly identical absorption and emission spectra (Figure 2.18) but may display a slight quantum yield enhancement. While the changes of quantum yield and radiative rate changes are within the error of the measurement, the change in  $k_{tot}$  and  $k_{nr}$  are significant ( $p < 0.05$  for both compared to dye **3**, Figure 2.7c, and details in Section 2.5f). The trend suggests that further deuteration may significantly enhance  $\phi_F$ .

## 2.3. Discussion

Every chromophore system is subject to the same energy gap laws described above, however, our data suggests that polymethine dyes have some of the best intrinsic properties for SWIR absorption and emission, including high transition dipole moments and small Stokes shifts.<sup>66</sup> To show this in comparison to other chromophores, we plot the energy where  $k_r = k_{nr}$  (or  $\phi_F = 0.5$ ) for fixed  $C$ , but variable  $\mu_{12}$  and  $E_{ST}$  in Figure 2.8. For simplicity, we assume the Stokes shift largely arises due to coupling to the  $3000\text{ cm}^{-1}$  C-H stretches (details in Section 2.5g). We then overlay the transition dipole moments and Stokes shifts of other common dye classes.<sup>67-70</sup> Within this model our results suggest that common chromophore scaffolds (e.g., BODIPY and xanthene derivatives such as fluorescein) may be challenging to shift into the SWIR while retaining high quantum yields, though squaraines provide a potential avenue for further exploration. Donor-acceptor dyes with fused ring acceptors have SWIR  $\phi_F$  emission at 0.03 and are intriguing given their large Stokes shift ( $1000 - 3000\text{ cm}^{-1}$ ), which would seem to be deleterious to the quantum yield.<sup>28,71,72</sup> However, the  $E_g$  of these SWIR emitting chromophores are bluer than other scaffolds. For example, COTIC-4F in toluene has  $\lambda_{em} = 915\text{ nm}$  and  $\phi_F = 0.055$ , but its  $E_g$  of  $11474\text{ cm}^{-1}$  is comparable to that of dye **17**, which has a quantum yield of 0.061, demonstrating that its impressive quantum yields in the SWIR is a balancing act between large Stokes shifts could be equivalent or slightly deleterious to quantum yield as shown in the example direct  $E_g$ . Nevertheless, large Stokes shifts may have a smaller effect on quantum yields than smaller energy gaps, and thus the tradeoff may be favorable, depending on application space and wavelength range.

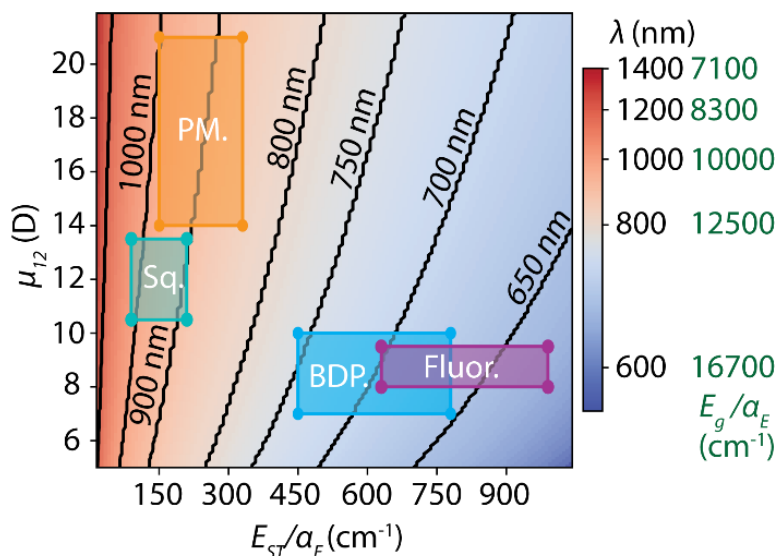


**Figure 2.8. 50% quantum yield energy map.** Solving for EQME=0.5 using two varying  $\mu_{21}$  and  $E_{ST}$ , demonstrates that high transition dipole moments and low Stokes shifts are necessary for scaffolds to have SWIR fluorescence. The predicted range for different dye scaffolds is in boxes as follows: polymethine (PM., orange), squaraine (Sq., teal), BODIPY (BDP., blue), and fluorescein (xanthene) (Fluor., purple).

Even with these favorable properties, the energy gap laws imply emission quantum yields of NIR/SWIR organic fluorophores will remain around 3% or less unless fundamental changes to the radiative and non-radiative pathways are realized. Stated succinctly, *a chromophore is only as good as its worst non-radiative decay pathway*. For visible chromophores, chemists have developed powerful tools to systematically improve quantum yields (e.g., rigidification), but these decay channels are no longer the limiting pathways for NIR/SWIR chromophores, with the vibrational relaxation as the limiting pathway. For example, conformationally restricted cyanine dyes (the CyB class) has shown dramatic increases to  $\phi_F$  in the visible (e.g 0.09 to 0.85 for Cy3 and Cy3B<sup>73-75</sup>, 0.15 to 0.69 for Cy5 and Cy5B)<sup>76</sup> but very small changes in the NIR (0.24 to 0.29 for Cy7 and Cy7B)<sup>39</sup> Though all have a decrease in Stokes shift with rigidification, they also notice

less impact of viscosity of solvent in Cy7 versus Cy5 indicative less impact of torsional rotation.<sup>39,76</sup> The decreased Stokes shift does suggest that the contribution of the highest frequency mode to the Stokes shift is not 1, and adds credence to the optimistic limit in EQME. Nevertheless, high frequency deactivation does appear to be the limiting factor. In the NIR/SWIR, decreased energy gaps lead to short tunneling barriers and concomitant high  $k_{nr}$ . Eliminating these pathways requires fundamentally altering the high-frequency vibronic manifold (through deuteration or fluorination), or short circuiting the radiative pathways for the chromophore. On the other hand, deuteration may not significantly improve quantum yields in the visible, as other nonradiative pathways govern excited state dissipation. Energy gap law analysis may help determine the theoretical maximum quantum yield, and help researchers decide the appropriate path toward systematic quantum yield improvement.

We find that SWIR chromophores are deactivated via omnipresent vibronic coupling which directly connects ground and excited states through tunneling, mediated by C-H stretches. However, identifying precisely which C-H stretches should be modified remains an open question. Recent work by Hirata *et al.* on deuteration of *N,N'*-diphenyl-*N,N'*-(3-methyl phenyl)-1,1'-biphenyl-4,4'-diamine suggests that the location of the deuteration will have differential effects on the vibronic manifold, suggesting that some stretches are privileged in dissipative dynamics.<sup>65</sup> Further supporting this view, systems with high quantum yields in the SWIR (Pb and Hg chalcogenide nanocrystals, lanthanide f-orbital centers), have transitions which couple mostly to low-frequency phonon modes, i.e.,  $E_M/a_E \leq 300 \text{ cm}^{-1}$ ,<sup>29</sup> consistent with higher QYs and considerably weaker direct nonradiative decay pathways. Mode-specific chemical transformations should be further explored as a pathway to improve quantum yields.

Many studies have made note of the deleterious effect of water as a solvent for quantum yields.<sup>77,78</sup> EQME only considers solvent refractive index and its effect on radiative rates (water has a lower refractive index of 1.33 vs 1.41 for DCM, resulting in a small decrease in radiative rates and quantum yields). However, this is insufficient to explain both the magnitude of quenching in water compared to other solvents, and the effect of deuterated water which increases quantum yields. Recent work has suggested that FRET into overtone vibrational bands of O-H stretches can impact quantum yields.<sup>77,79</sup> This is supported by prior work on SWIR emissive quantum dots<sup>78</sup> and preliminary data in Section 2.5h. This latter solvent effect is an additional deactivation pathway so for most cases the trend from EQME that we see in organics will transfer into water and other biologically relevant solvents. Still, further research exploring the effect of solvent environment in the SWIR will be fruitful.

## **2.4. Conclusion**

To make systematic improvements to SWIR chromophores, we first explore the validity of energy gap laws for radiative and nonradiative rates and apply it to analyze a large data set of NIR/SWIR polymethine dyes. We derive an energy gap quantum yield master equation which demonstrates that the precipitous drop in quantum yields in the SWIR is consistent with the exponentially increasing nonradiative decay rates and decreasing radiative rates, with the former mediated by the presence of high frequency vibrational modes. Energy gap laws must be considered when comparing NIR/SWIR chromophores as improvements to quantum yield are directly correlated to the energy gap. By creating energy gap neutral comparators, we elucidate the impact of simple structural derivatives on quantum yield. We thus assess the natural limits of quantum yield in chromophores and provide a path forward in the inverse design problem. The presence of organic alkenyl C-H stretches likely limits the maximum possible quantum yield for

SWIR emitters, but our preliminary results suggest that deuteration and judicious chromophore design may provide a path forward. We believe that a general and unified framework will enable the design of novel SWIR chromophore systems beyond the polymethine chromophore class and enable rational optimization of fluorescence in these systems.

## 2.5. Supporting Information

### 2.5a. Methods

#### 2.5a.i. Materials

Chromophore structures are shown in Figure 2.1. IR-1061(**1**) was purchased from Sigma Aldrich. IR-26 (**2**) was purchased from Exciton. Dichloromethane (DCM, HPLC grade), ethanol (anhydrous) and ethanol-d1 (99.5%) were purchased from Fisher scientific. IR-27 (**4**) and dyes **3–4**, **7–15**,<sup>34</sup> and **5–6** and **16–21**<sup>35</sup> were prepared following reported procedures.

#### 2.5a.ii. Absorption coefficient

Absorption coefficients were calculated with serial dilutions in DCM in volumetric glassware. Error was taken as the standard deviation of the triplicate measurement. Absorbance spectra were collected on a JASCO V-770 UV-VIS/NIR spectrophotometer. The total molar absorption coefficient was numerically integrated over the NIR/SWIR absorption.

To find the integrated absorption cross section of the  $S_0 \rightarrow S_1$  electronic state including its vibrational progression (Figure 1) in units of absorption ( $\sigma(\omega)$ ) per unit angular frequency we numerically integrate using linear interpolation and Simpson's rule (Equation 2.12):

$$\int_{x_0}^{x_N} f(x)dx \approx \frac{x_n - x_0}{3n} \sum_{i=1}^{\frac{n}{2}} f(x_{2i-2}) + f(x_{2i-1}) + f(x_{2i}). \quad (\text{Eq. 2.12})$$



Standard error was calculated by repeating this method for the upper bound and lower bound of each point from repeat measurements. The number of points used for the interpolation was twice that of the original points in that range.

### **2.5a.iii. Fluorescence quantum yield**

Photoluminescence spectra were obtained on a Horiba Instruments PTI QuantaMaster™ Series fluorometer with 90° collection. For dyes **1–16**, relative quantum yields were taken with IR-26 as the standard in DCM (detailed methodology in references).<sup>34,35</sup> The  $\Phi_F$  of IR-26 (**2**) was taken to be  $5 \times 10^{-4}$  in accordance with several recent measurements.<sup>26,29,30</sup> Dyes **17–21** were found using absolute quantum yield with an integrating sphere.<sup>35</sup> Quantum yield for **3'** and **3''** were determined using the relative method compared to **3** [ $\Phi_F = (0.61 \pm 0.02) \times 10^{-2}$ ].<sup>35</sup> For each compound, five solutions and a solvent blank were prepared and measured for their absorbance (890 nm) and emission spectra (excitation: 890 nm, emission collected between 920 – 1500 nm, no filter, excitation slit width: 0.77 nm, emission slit width: 11.52 nm, integration time: 0.3 s, step size: 4 nm) to plot integrated fluorescence intensity versus absorbance. Error calculation of quantum yield was propagated from the error in slope of both the reference and the unknown.

### **2.5a.iv. Time correlated single photon counting**

We recorded PL lifetimes using a home-built, all-reflective epifluorescence setup.<sup>37</sup> For dyes **1–15**, we used a pulsed 970 nm ( $70 \frac{\mu J}{cm^2}$ , IRF =  $44 \pm 1$  ps) excitation; for dyes **16–20**, we used a pulsed 780 nm ( $900 \frac{\mu J}{cm^2}$ , IRF =  $59 \pm 1$  ps) excitation; for the comparison of dye **3**, **3'**, **3''** we used a pulsed 785 nm ( $0.19 \frac{\mu J}{cm^2}$ , IRF =  $68 \pm 1$  ps) excitation. Emission was then collected and filtered with a 90:10 beamsplitter and appropriate excitation filters finally reflectively coupled

into a single-mode fiber (F-SMF-28-C-10FC, Newport) and detected using an SNSPD (Quantum Opus One™).<sup>35,37,80</sup>

Given the short lifetimes of these dye, lifetimes were fit with a convolution of the instrument response function and an exponential. To determine the lifetime (or decay rate,  $k$ ) for each TCSPC trace we fit each curve to a convolution of Gaussian with a single exponential decay:

$$I(t) = \frac{I_0}{2} e^{-k\left((t-t_0) - \frac{\sigma^2 k}{2}\right)} \left(1 + \operatorname{erf}\left(\frac{(t-t_0) - \sigma^2 k}{\sqrt{2}\sigma}\right)\right) \quad (\text{Eq. 2.13})$$

The width,  $\sigma$ , of the Gaussian was determined using the instrument response function (IRF) which was measured as the backscatter off of a cuvette with solvent (e.g., DCM) without the longpass filters. The initial peak amplitude,  $I_0$ , and the rate,  $k$ , were free fitting parameters, while the time offset,  $t_0$ , and the IRF width,  $\sigma$  were fixed variables. We use a conservative error of 1 ps (the instrument resolution) for our lifetimes except where noted in our statistics. Figure 2.9 shows the lifetime fitting of the Dye **3**, **3'**, **3''**.

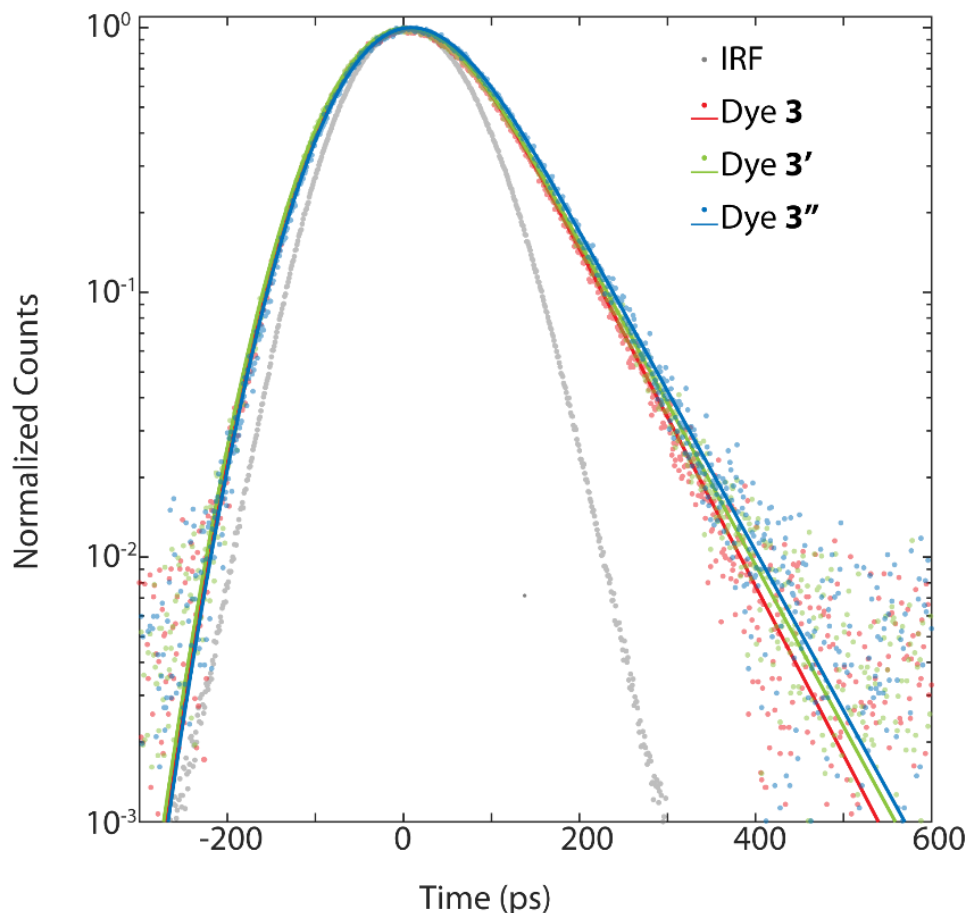


**Figure 2.9. Example lifetime fit.** Fitted lifetimes for dye **3**, **3'**, **3''**.

### 2.5b. Modeling Absorption and Emission

This manuscript establishes the relationship between the energy gap and quantum yield of molecular systems in the shortwave infrared. In this supporting information, we will outline or derive the expressions that relate spectroscopic and structural observables to the radiative and non-radiative rates of a molecular chromophore, separating molecular details (e.g., transition dipole moment, number of/coupling to vibrations, and excited/ground state degeneracy) from photonic degrees of freedom (e.g., index of refraction and density of photon states as a function of energy gap).

### 2.5b.i. Einstein coefficients, absorption, and emission.

There is considerable ambiguity when describing how spectroscopic observables such as the molar absorptivity, lifetime and quantum yield relate to intrinsic molecular properties such as transition dipole moment and oscillator strength. Much of the literature defines these relationships in terms of gas-phase atomic transitions, and while the physics is identical for molecular systems, the presence of a Stokes shift between absorption and emission, broader more complex lineshapes, a dielectric environment, and more complex excited state degeneracy complicates numerical comparison between chromophores.<sup>11,13,67,81,82</sup> Several papers clarify this discussion and we simply elaborate on their work below, keeping notation and unit consistency with our manuscript, and including solvent dielectric effect in all cases.<sup>11,13,67,81,82</sup> To guide the discussion, we provide a table of units for each of the terms given in both Gaussian and SI unit systems (Table 2.4).

To relate the molar absorptivity to the rate of absorption (and ultimately the rate of emission), we will use the Einstein formalism, depicted in Figure 2.10. In steady state the change in population is zero ( $N_1' = 0$ ), which allows us to express the following equation:

$$B_{12}^E N_1 u(E) = B_{21}^E N_2 u(E) + A_{21} N_2, \quad \text{Eq. (2.14)}$$

where  $B_{12}$ ,  $B_{21}$  and  $A_{21}$  are the rate constants for absorption, stimulated emission and spontaneous emission respectively,  $u(E)$  is the energy density of radiation per unit energy, and  $N_1$  and  $N_2$  are the population of molecules in  $\psi_1$  and  $\psi_2$  respectively. The superscript omega denotes that these  $B$  coefficients include units of angular frequency as it is the rate of absorption or stimulated emission at a given excitation energy.

<b>Table 2.4. Unit Table</b>		
<b>Variable</b>	<b>Gaussian (cgs)</b>	<b>SI units</b>
$B_{12}$ or $B_{21}$	$\frac{cm}{g}$	$10 \frac{m}{kg}$
$A_{21}$	$s^{-1}$	$s^{-1}$
$I$	$\frac{g}{s^2 cm}$	$10 \frac{kg}{s^2 m}$
$\sigma_0$	$cm^2 erg$	$10^{-3} m^2 J$
$\epsilon$	$mol \cdot cm^2$	$10^4 mol \cdot m^2$
$u(E)$ (black body)	$\frac{g}{cm} erg$	$10^{-7} \frac{kg}{m} J$
$\langle U \rangle$	$\frac{g}{s^2 \cdot cm}$	$0.1 \frac{kg}{s^2 \cdot m}$
$\mu_{21}$	$D$	$3.335 \times 10^{30} C \cdot m$

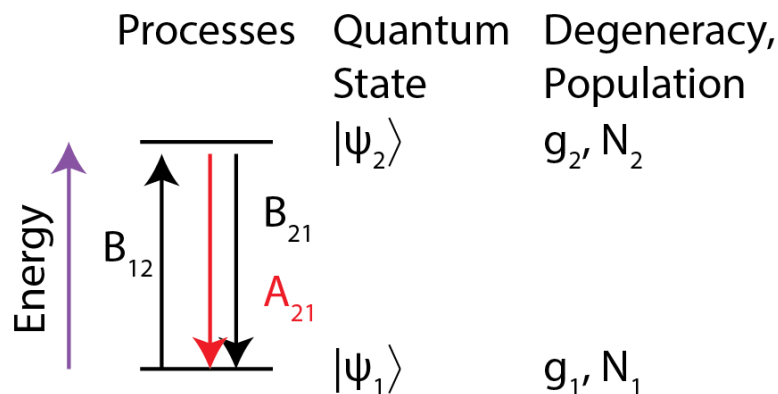


**Figure 2.10. Depiction of Einstein coefficients.** Defining induced absorption, stimulated emission, and spontaneous emission for a 2-level system.

### 2.5b.ii. Absorption parameters to Einstein coefficients

The absorption cross section ( $SI: m^2$ ) is measurable using a conventional UV-VIS spectrometer. The cross section is defined as the energy absorbed by the chromophore per unit time divided by the energy per unit area per unit time of incident light (i.e., intensity). The energy absorbed per second is given by the rate of absorption,  $(B_{12}^E u(E))$  (total units of  $s^{-1}$ ), multiplied by the energy of each photon absorbed ( $E_g$ ). The intensity is given by the average energy density of monochromatic light as  $\langle U \rangle$  (energy per unit volume). The input intensity is therefore  $I_0 = v \langle U \rangle$ , where  $v$  is the speed of light in a dielectric medium, i.e.,  $v = c/n$ . We arrive at the following expression for cross section:

$$\sigma(E) = \frac{nEB_{12}^E u(E)}{c \langle U \rangle}, \quad (\text{Eq. 2.15})$$

which simplifies to:

$$\sigma(E)dE = \frac{nEB_{12}^E}{c}, \quad (\text{Eq. 2.16})$$

where  $\langle U \rangle = u(E)dE$ . The change in intensity as a function of penetration depth of this incident light is:

$$\frac{dI}{dx} = -N_1\sigma(E)I(x)dI, \quad (\text{Eq. 2.17})$$

which for a fixed path length,  $l$ , leads naturally to:

$$\frac{I_{final}}{I_0} = e^{-N_1\sigma(E)l}. \quad (\text{Eq. 2.18})$$

A standard absorption spectrometer measures the intensity transmitted of absorbed light as a function of input frequency for a monochromatic beam. By chemistry convention the absorbance is:

$$A(E) = -\text{Log}_{10} \frac{I(E)}{I_0(E)} = \epsilon(E)ML. \quad (\text{Eq. 2.19})$$

where  $\epsilon(E)$  is the molar absorptivity (or attenuation),  $M$  is the concentration of sample (commonly in units of molarity), and  $L$  is the path length. This translates to cross section as follows:

$$\sigma(E) = \frac{1000}{N_A \log_{10} e} \epsilon(E) \approx 1.66 \times 10^{-21} \epsilon(E). \quad (\text{Eq. 2.20})$$

In this paper, we will consider uniform illumination over the entire lowest energy absorption feature (usually well separated in the NIR or SWIR). Our coefficient therefore corresponds to the overall absorption of the lowest energy transition(s). We thus define single absorption coefficient  $\sigma_0$  corresponding to the following integral:

$$\sigma_0 = \int_{\omega_1}^{\omega_2} \sigma(E)dE. \quad (\text{Eq. 2.21})$$

We can also define a simple lineshape function  $g(E) = \sigma(E)/\sigma_0$ . This allows us to use either the overall Einstein coefficient  $B_{12}$ , or the coefficient at a specific wavelength  $B_{12}^E = B_{12}g(E)$ . To relate the measured total absorption cross section with emission, we will use the rest of the relevant Einstein coefficient relations. Without external illumination, (at thermal equilibrium) the population at each energy level is  $\frac{N_2}{N_1} = \frac{g_2}{g_1} e^{-\beta E_g}$ , where  $\beta = (kT)^{-1}$ ,  $E_g$  is the energy gap, and  $g_1$  and  $g_2$  are the degeneracy of ground and excited state respectively. Here, we can use  $u(\omega)$  the energy density of a blackbody at temperature  $T$  and  $\nu$ :

$$u(E) = \frac{E_g^3}{\pi^2 \nu^3 \hbar^2 (e^{\beta E} - 1)}. \quad (\text{Eq. 2.22})$$

Through substitution of  $N_2$ ,  $u(E)$ , and  $\nu$  in S3 we arrive at:

$$\frac{B_{12} E_g^3 n^3}{\pi^2 \hbar^2 c^3} = \frac{g_2 B_{21} E_g^3 n^3}{g_1 \pi^2 \hbar^2 c^3} e^{-\beta E_g} + A_{21} \frac{g_2}{g_1} (1 - e^{-\beta E_g}). \quad (\text{Eq. 2.23})$$

Equation 2.23 is true at all temperatures which allows us to relate absorption and spontaneous emission. For the low temperature limit (appropriate when  $kT \ll \hbar\omega$ ), then  $T \rightarrow 0, \beta \rightarrow \infty$ :

$$B_{12} = \frac{g_2 \pi^2 \hbar^2 c^3}{g_1 E_g^3 n^3} A_{21}. \quad (\text{Eq. 2.24})$$

Therefore, one can calculate the radiative rate from the absorption cross section, assuming we know the relevant energy gap ( $E_g$ ) and the ratio of the degeneracy between ground and excited states:

$$\sigma_0 = \frac{n \hbar E_g B_{12}}{c} = \frac{g_2 A_{21} \pi^2 \hbar^3 c^2}{g_1 E_g^2 n^2}. \quad (\text{Eq. 2.25})$$



We obtain  $A_{21}$  independently by measuring the lifetime and quantum yield of each dye (see Section 2.5a), we can compare each to determine the degeneracy ratio  $\frac{g_2}{g_1}$  for each dye.

In this chapter, to compare absorption and emission measurements we assume a common energy gap for all photophysical measurements, in this case the midpoint between absorption and emission. Within the displaced harmonic oscillator model,  $E_g$  is the energy difference between harmonic wells. As cyanine dyes have small Stokes shifts and low Huang Rhys factors, we believe this simplification will introduce minimal relative errors. We can therefore relate our absorption cross section to the spontaneous (radiative) rate:

$$A_{21} = \frac{g_1}{g_2} \frac{E_g^2 n^2}{\hbar^3 \pi^2 c^2} \sigma_0 = \frac{g_1}{g_2} \frac{1000 E_g^2 n^2}{N_A \text{Log}_{10}(e) \pi^2 \hbar^3 c^2} \int_{E_1}^{E_2} \epsilon(E) dE. \quad (\text{Eq. 2.26})$$

### 2.5b.iii. Comparison to the Strickler-Berg equation

The spontaneous radiative rate coefficient derived here matches that derived by Strickler and Berg with appropriate unit conversions (reproduced below in both the common condensed form and its expanded form):<sup>13</sup>

$$A_{21} = 2.88 \times 10^{-9} n^2 \langle \tilde{\nu}_f^{-3} \rangle^{-1} \frac{g_1}{g_2} \int_{\omega_1}^{\omega_2} \epsilon(\tilde{\nu}) d \ln(\tilde{\nu})$$

$$= \frac{8 \times 1000 \pi c n^2}{N_A \log_{10} e} n^2 \langle \tilde{\nu}_f^{-3} \rangle^{-1} \frac{g_1}{g_2} \int_{\omega_1}^{\omega_2} \epsilon(\tilde{\nu}) d \ln(\tilde{\nu}). \quad (\text{Eq. 2.27})$$

Note that in this equation, energy is defined in wavenumber not energy defined in Joules as described above. Additionally, the Strickler-Berg equation accounts for the molecular band gap differently by differentiating between the emission energy and the absorption energy such that the carrier frequency is defined by the fluorescence spectra. While this is a reasonable approximation,

it renders absorption and emission metrics of radiative rates internally inconsistent, so we will use the mid-gap point instead.

#### 2.5b.iv. Relating Einstein coefficients to transition dipole moments

The transition dipole moment is the molecular parameter which sets the strength of absorption and the rate of emission for dipole allowed transitions. We can derive the relationship between the transition dipole moment and radiative rate through an application of Fermi's Golden rule. The transition rate comes from first order perturbation theory:<sup>83</sup>

$$A_{21} = \frac{2\pi}{\hbar} |M_{21}|^2 g(E_g). \quad (\text{Eq. 2.28})$$

In free space,  $g(E_g)$ , can be computed by computing the number of photon modes in a cavity of volume  $V_0$ :

$$g(E_g) = \frac{E_g^2 V_0}{\pi^2 \hbar^2 v^3}. \quad (\text{Eq. 2.29})$$

For a randomly oriented dipole in free space, the transition matrix is:

$$|M_{12}|^2 = \frac{1}{3} \mu_{21}^2 \epsilon_{vac}^2, \quad (\text{Eq. 2.30})$$

with the magnitude of energy of the fluctuating electric field in a vacuum defined as:

$$\epsilon_{vac} = \left( \frac{E_g}{2\epsilon_0 V_0} \right)^{\frac{1}{2}}. \quad (\text{Eq. 2.31})$$

Combining equations 2.28-2.30 leads to:

$$A_{21} = \frac{\mu_{21}^2 E_g^3}{3\pi \hbar^4 v^3 \epsilon}. \quad (\text{Eq. 2.32})$$

We modify this slightly by including the refractive index  $\varepsilon = \varepsilon_0 n^2$  (in cgs units  $\varepsilon = \frac{1}{4\pi} n^2$ ). With this correction, we arrive at:

$$A_{21} = \frac{4\mu_{21}^2 E_g^3 n}{3\hbar^4 c^3}, \quad (\text{Eq. 2.33})$$

which is identical to the equation found in the prior literature with the addition of the refractive index correction.<sup>11</sup> We can therefore relate transition dipole moment to the absorption cross section using equations 2.25 and 2.33 as follows:

$$\mu_{21}^2 = \frac{g_1}{g_2} \frac{3\hbar n c}{4E_g \pi^2} \sigma_0. \quad (\text{Eq. 2.34})$$

### 2.5b.v. Oscillator strength

Oscillator strength is defined as the comparison of the absorption or emission rate to the rate of absorption or emission of a classical oscillator. The classical oscillator rate of transition is defined as:

$$\gamma_{cl} = \frac{q^2 E_g^2 n}{6\pi \varepsilon_0 m \hbar^2 c^3}, \quad (\text{Eq. 2.35})$$

where  $m$  is the mass of an electron and  $q$  is electron charge. We then can define the emission oscillator strength as:

$$f_{21} = -\frac{\frac{1}{3} A_{21}}{\gamma_{cl}}. \quad (\text{Eq. 2.36})$$

We use the radiative rate found through use of quantum yield and total lifetime to determine the oscillator strength of emission. Similar to how  $B_{12}$  and  $B_{21}$  are related by the degeneracy ratio so

are  $f_{12}$  and  $f_{21}$ . We can solve for  $f_{12}$  with the relationship between the classical oscillator cross section,  $\sigma_{oc}$ , compared to the experimental absorption cross section:<sup>11</sup>

$$\sigma_{oc} = \int_{-\infty}^{\infty} \frac{\frac{\gamma_{cl}}{2\pi}}{\left(\frac{E}{\hbar} - \frac{E_0}{\hbar}\right)^2 + \left(\frac{\gamma_{cl}}{2}\right)^2} \frac{\pi q^2}{2\varepsilon_0 mc} dE, \quad (\text{Eq. 2.37})$$

and

$$f_{12} = \frac{\sigma_0}{\sigma_{oc}} \Rightarrow \frac{2\varepsilon mc}{\pi \hbar q^2} \sigma_0. \quad (\text{Eq. 2.38})$$

## 2.5c. Nonradiative Rate Estimation

### 2.5c.i. Exponential rate law assumptions.

We summarize the nonradiative rate energy gap law as derived in Englman and Jortner (E&J) and shown in equation 2.6. E&J notes that internal conversion in large molecules closely resembles the mutiphonon relaxation in semiconductors. In short, the large number of vibrational frequencies resembles a quasicontinuum of transitions which can weakly couple the ground and excited states. They then derive the rate equations in two limits, the first applicable for systems with large Stokes shifts relative to the energy gaps (appropriate for systems with avoided crossing or conical intersections), and the other applicable with small Stokes shifts relative to the energy gap (relevant to our work). Within the latter limit, it is possible to evaluate the rate as defined below for first order perturbation theory (or Fermi's Golden Rule). Therefore, the rate is as follows:

$$W = \frac{2\pi}{\hbar} \sum_i \sum_j p(si) |V_{si,lj}|^2 \delta(E_{si} - E_{lj}), \quad (\text{Eq. 2.39})$$

where  $p(si)$  is the occupation of a given mode on the excited state. They further simplify this equation to:

$$V_{si,lj} \approx CS_{si,lj}, \quad (\text{Eq. 2.40})$$

where  $C$  is the coupling term between ground and excited states, and  $S_{si,lj}$  are the Franck Condon overlap factors:

$$S_{si,lj} = \prod_t \left\langle X_{e,t} \left( Q_t^{(e)}, \nu_{e,t} \right) \middle| X_{g,t} \left( Q_t^{(g)}, \nu_{g,t} \right) \right\rangle, \quad (\text{Eq. 2.41})$$

where  $X_{(e,g)t} \left( Q_t^{(e,g)}, \nu_{(e,g),t} \right)$  are the excited or ground nuclear wavefunctions.

$C$  is derived in a previous paper,<sup>41</sup> and is the total derivative or Hertzberg-Teller coupling,<sup>84,85</sup> the largest perturbation to the Born-Oppenheimer approximation which couples ground and excited states. While this is challenging to calculate or experimentally determine, estimates typically range from  $10^2 \text{ cm}^{-1}$  to  $10^4 \text{ cm}^{-1}$ , for which we use  $798 \text{ cm}^{-1}$  and  $1628 \text{ cm}^{-1}$  in this chapter.

E&J arrive at a method for evaluating the Franck-Condon overlap factors through the use of the displaced harmonic oscillator model combined with a generating function method.<sup>86</sup> Within the weak coupling limit (where the Stokes shift is small) they evaluate the summation using the method of steepest descent, arriving at the expression shown in equation 2.6. Within this estimate, they find that the highest energy vibration contributes the most to the summed overlap integral, which for organic molecules is typically the C-H stretch.

To allow for clarity between E&J equation and the version used in the text in order to simplify and allow for it to be combined with radiative rate expressions.

E&J denotes the equation as:

$$k_{nr} = \frac{C^2\sqrt{2\pi}}{\hbar\sqrt{\hbar\omega_M\Delta E}} \exp\left[-\frac{\Delta E}{\hbar\omega_M}\left(\ln\left(\frac{2\Delta E}{d\hbar\omega_M\Delta_M^2}\right) - 1\right)\right], \quad (\text{Eq. 2.42})$$

where,  $\Delta E$  is the energy at the HOMO-LUMO gap,  $\omega_M$  is the maximum vibration,  $d$  is the number of degenerate or near degenerate modes,  $\Delta_M$  is the reduced displacement of the maximum transition.  $\hbar\omega_M$  and  $\Delta E$  are changed to  $E_M$  and  $E_g$ , respectively. The main changes are made to the  $d\hbar\omega_M\Delta_M^2$  terms, as these relate to parameters to more spectroscopic variables.

We can relate these vibrational displacement parameters to the Stokes shift,  $E_{ST}$ , as a summation of all the vibrations coupled to the electronic transition:

$$E_{ST} = \sum_j \hbar\omega_j\Delta_j^2 \geq d\hbar\omega_M\Delta_M^2. \quad (\text{Eq. 2.43})$$

We can thus recast the  $d\hbar\omega_M\Delta_M^2$  as a proportion of the total Stokes shift,  $\gamma_M$ , such that  $\gamma_M = \frac{d\hbar\omega_M\Delta_M^2}{E_{ST}}$ .

Plugging into equation 2.42, we get the equation in the text:

$$k_{nr} = \frac{C^2\sqrt{2\pi}}{\hbar\sqrt{\hbar\omega_M E_g}} \exp\left[-\frac{\Delta E}{\hbar\omega_M}\left(\ln\left(\frac{2E_g}{\gamma_M E_{ST}}\right) - 1\right)\right]. \quad (\text{Eq. 2.44})$$

We also tested if the Huang Rhys parameter of 0.1 for a C-H mode would be observable. Based

on a simple Frank Condon model, we see that under the ideal pessimistic scenario this peak could be resolved though the intensity is considerably under the background (Figure 2.11). Our results suggest that a 0.1 H-R coupled 3000  $\text{cm}^{-1}$  vibronic feature is plausible under the absorption envelope.

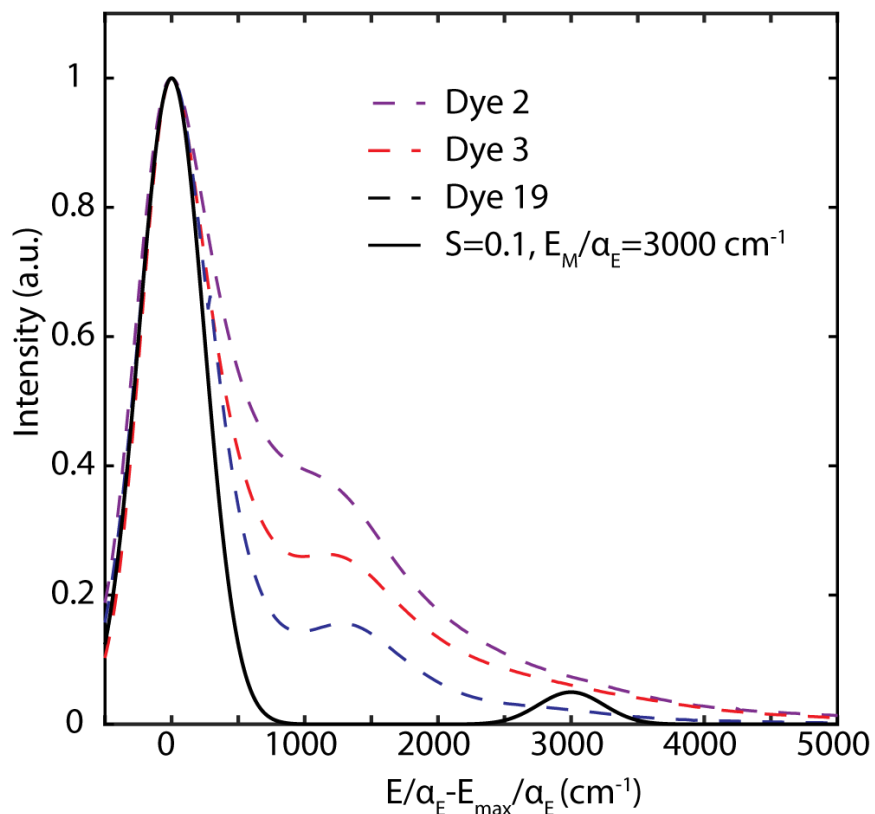


**Figure 2.11. Vibronic feature comparison.** Comparison of a 3000  $\text{cm}^{-1}$  vibronic feature with an  $S=0.1$  to a selection of dyes that are centered to their maximum peak energy.

### 2.5c.ii. Impact of $\gamma_m$ and $C$ on quantum yield

In Figure 2.12, we test the how variance in  $\gamma_M$  and  $C$  affect the quantum yield fit (equation 2.9). Decreasing both parameters, shifts the energy at which the quantum yield precipitously falls off further into the red as both parameters impact the amount of coupling to the vibrational relaxation manifold.

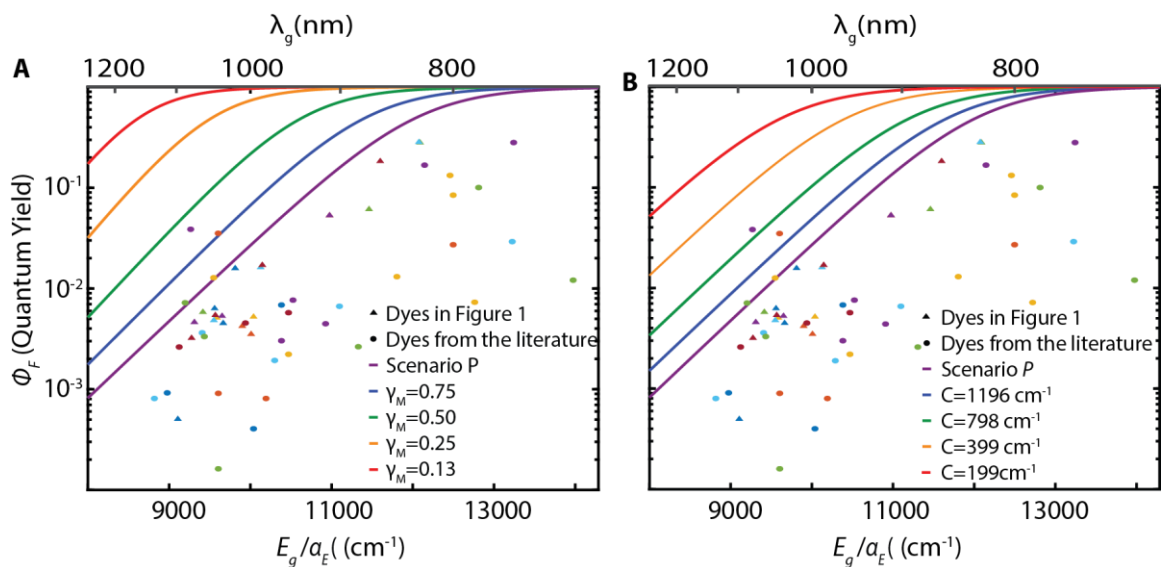


**Figure 2.12. Impact of  $\gamma_M$  or  $C$  on the quantum yield with respect to energy gap.** Plots showing the impact of changing (a) the degree to which the high frequency mode couples to the quantum yield ( $\gamma_m$ ) and (b) the nonadiabatic coupling ( $C$ ) on the quantum yield while keeping the other value held constant. Scenario P represents the pessimistic case.



### 2.5d. EQME with Labelled Polymethine Dyes

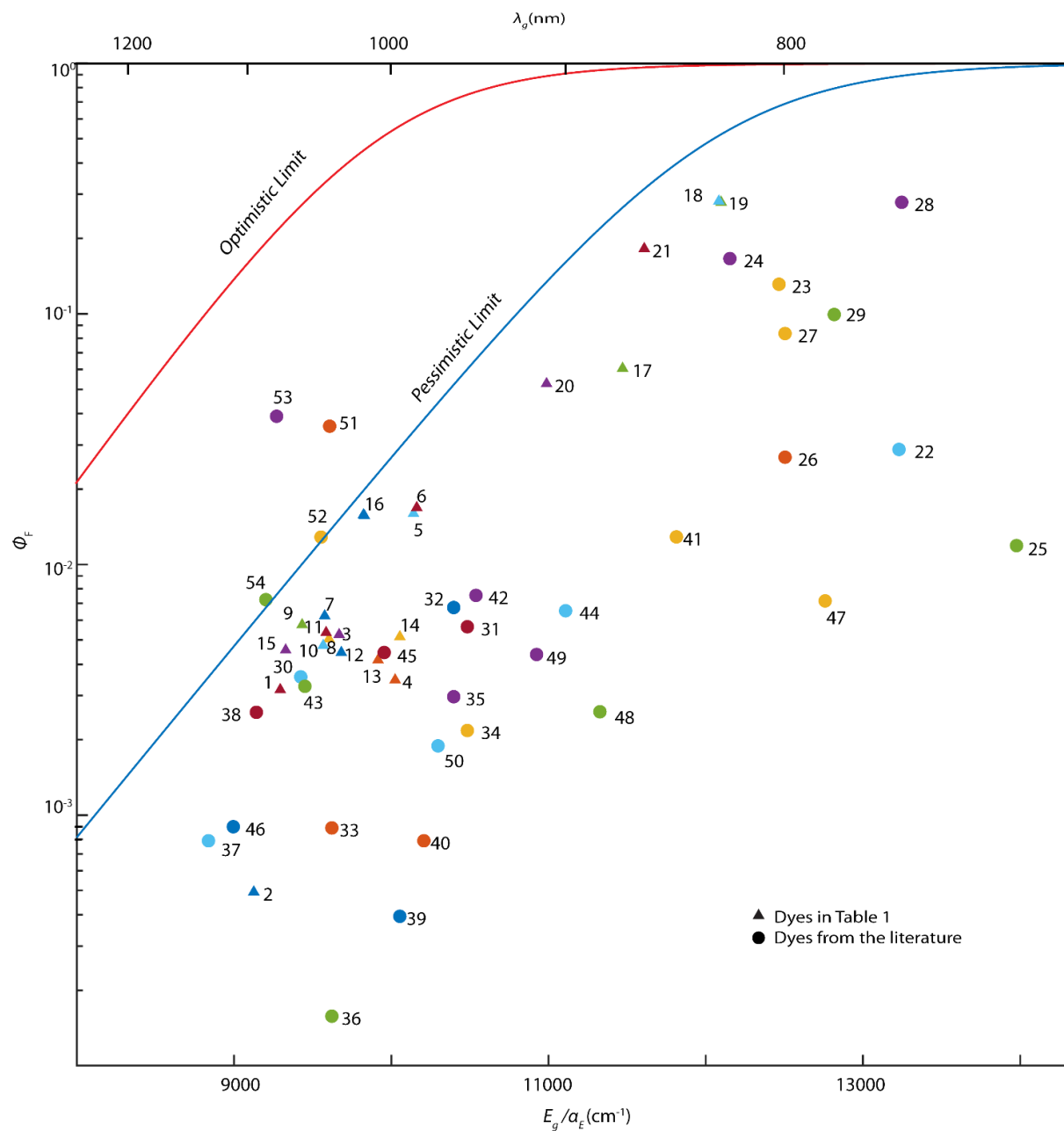


**Figure 2.13.** Labelled version of figure 2.5. Combined Energy Gap Law for optimistic and pessimistic cases, with a key for the points in Table 2.5.

**Table 2.5. Key for Figure 2.13**

<b>Label</b>	<b>Dye</b>	<b>Label</b>	<b>Dye</b>	<b>Label</b>	<b>Dye</b>
<b>1</b>	IR-1061 <sup>26</sup>	<b>19</b>	8 <sup>35</sup>	<b>37</b>	5L5 in DCE <sup>33</sup>
<b>2</b>	IR-26 <sup>34</sup>	<b>20</b>	4 <sup>35</sup>	<b>38</b>	5H5 in DCE <sup>33</sup>
<b>3</b>	1(Flav 7) <sup>34</sup>	<b>21</b>	10 <sup>35</sup>	<b>39</b>	6L6 in DCE <sup>33</sup>
<b>4</b>	11(IR-27) <sup>34</sup>	<b>22</b>	Flav3 <sup>26</sup>	<b>40</b>	6H6 in DCE <sup>33</sup>
<b>5</b>	7 <sup>35</sup>	<b>23</b>	IR-125 <sup>46</sup>	<b>41</b>	Rh824 <sup>50</sup>
<b>6</b>	5 <sup>35</sup>	<b>24</b>	IR-140 <sup>46</sup>	<b>42</b>	Rh923 <sup>50</sup>
<b>7</b>	2 <sup>34</sup>	<b>25</b>	Cryptocyanine <sup>46</sup>	<b>43</b>	Rh1093 <sup>50</sup>
<b>8</b>	4 <sup>34</sup>	<b>26</b>	ICG in PBS <sup>45</sup>	<b>44</b>	CX1 in CHCl <sub>3</sub> <sup>51</sup>
<b>9</b>	7 <sup>34</sup>	<b>27</b>	ICG in 70:30 EtOH:H <sub>2</sub> O <sup>45</sup>	<b>45</b>	CX2 in CHCl <sub>3</sub> <sup>51</sup>
<b>10</b>	5 <sup>34</sup>	<b>28</b>	HITC <sup>45</sup>	<b>46</b>	CX3 in CHCl <sub>3</sub> <sup>51</sup>
<b>11</b>	6 <sup>34</sup>	<b>29</b>	IR-800 <sup>47</sup>	<b>47</b>	8 <sup>80</sup>
<b>12</b>	8 <sup>34</sup>	<b>30</b>	FD-1080 in EtOH <sup>48</sup>	<b>48</b>	7 <sup>80</sup>
<b>13</b>	9 <sup>34</sup>	<b>31</b>	BTC980 in DCE <sup>49</sup>	<b>49</b>	10 <sup>80</sup>
<b>14</b>	10 <sup>34</sup>	<b>32</b>	BTC982 in DCE <sup>49</sup>	<b>50</b>	11 <sup>80</sup>
<b>15</b>	3(JuloFlav7) <sup>34</sup>	<b>33</b>	BTC1070 in DCE <sup>49</sup>	<b>51</b>	LZ-1060 in CH <sub>3</sub> OH <sup>32</sup>
<b>16</b>	9 <sup>35</sup>	<b>34</b>	BTC980 in PBS <sup>49</sup>	<b>52</b>	LZ-1092 in CH <sub>3</sub> OH <sup>32</sup>
<b>17</b>	2 <sup>35</sup>	<b>35</b>	BTC982 in PBS <sup>49</sup>	<b>53</b>	LZ-1105 in CH <sub>3</sub> OH <sup>32</sup>
<b>18</b>	6 <sup>35</sup>	<b>36</b>	BTC1070 in PBS <sup>49</sup>	<b>54</b>	LZ-1118 in CH <sub>3</sub> OH <sup>32</sup>

## 2.5e. Derivation of Comparison Equation

We desire a method to compare chromophores with different energy gaps. We observe that the log of the quantum yield varies linearly in the NIR and SWIR for our parameters. Therefore, we will use a linear model to develop an energy-gap independent quantum yield comparator.

We will assume that we have two chromophores,  $a$  and  $b$  with quantum yields  $\phi_a$  and  $\phi_b$ , and energy gaps  $E_a$  and  $E_b$ . Here, we define  $\phi_a^\dagger$  as the prediction of what the quantum yield of  $a$  would be at  $E_b$ . We define improvement factor as  $\zeta = \frac{\phi_b - \phi_a^\dagger}{\phi_a^\dagger}$ . Values greater than zero indicate improvement relative to the energy gap law expectation. We can predict  $\phi_a^\dagger$  is the quantum yield prediction of chromophore  $b$  given the molecular properties from chromophore  $a$  and the linear approximation of this energy gap law such that:

$$\ln(\phi_a^\dagger) = \kappa(\Delta E) + \ln(\phi_a) \quad (\text{Eq. 2.45})$$

and:

$$\phi_a^\dagger = \phi_a e^{\kappa \Delta E}, \quad (\text{Eq. 2.46})$$

where  $\Delta E = E_b - E_a$ .

Plugging back into our improvement factor we have the improvement factor as defined in the main text:

$$\frac{\phi_b}{\phi_a} e^{-\kappa \Delta E} - 1. \quad (\text{Eq. 2.47})$$

The slope  $\kappa$  can be found from taking the natural log of equation 2.8 leading to the following expression:

$$\ln \phi(E_g) = \ln \left( 1 + \frac{3\epsilon_0 c^2 C^2}{2^{\frac{5}{2}} \pi^{\frac{3}{2}} \mu_{12}^2 n E_M^{\frac{1}{2}} E_g^{\frac{7}{2}}} \exp \left[ -\frac{E_g}{E_M} \left( \ln \frac{2E_g}{\gamma_M E_{ST}} - 1 \right) \right] \right)^{-1}. \quad (\text{Eq. 2.48})$$

Combining constants, we arrive at:

$$\ln \phi(E_g) = \ln \left( 1 + a E_g^{-\frac{7}{2}} \exp[-b E_g (\ln(c E_g) - 1)] \right)^{-1}. \quad (\text{Eq. 2.49})$$

If the second term in equation 2.46 is larger than 1, (true for low QY samples), we consider the following equation which we will take the derivative of to find the slope:

$$\frac{d \ln \phi(E_g)}{d E_g} = \frac{d}{d E_g} \left( -\ln \left( a E_g^{-\frac{7}{2}} \exp[-b E_g (\ln(c E_g) - 1)] \right) \right). \quad (\text{Eq. 2.50})$$

upon simplification, we reach:

$$\frac{d \ln \phi(E_g)}{d E_g} = \frac{7}{2 E_g} + b (\ln(c E_g)). \quad (\text{Eq. 2.51})$$

Assuming that  $\gamma_M = 1$  we arrive at the following expression:

$$\frac{d \ln \phi(E_g)}{d E_g} = \kappa = \frac{7}{2 E_g} + \frac{1}{E_M} \ln \left( \frac{2 E_g}{\gamma_M E_{ST}} \right). \quad (\text{Eq. 2.52})$$

We show that  $\kappa$  slightly overestimates the numerically evaluated slope in Figure 2.14 from 950 to 1200 nm This indicates that our numbers evaluate a conservative estimate of improvement

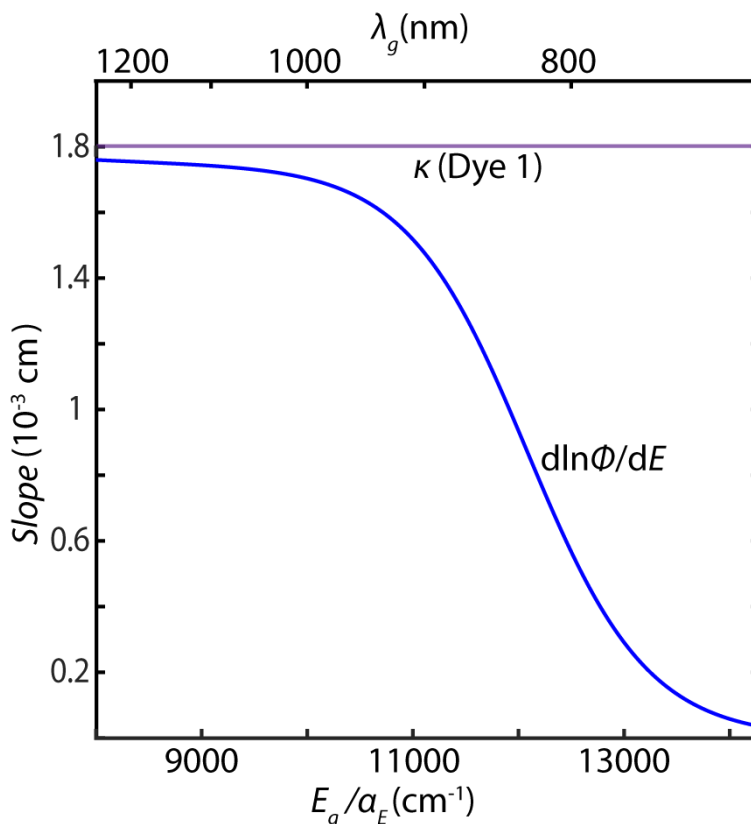


**Figure 2.14. EQME slope versus the  $\kappa$  estimation.** Comparison of the slope estimation described above to a numerical derivative of the natural log of the slope and the inverse of the nonradiative rate.

### 2.5e.i. Enhanced worked example

In Figure 2.15 we compare dyes **2–4** (common names, IR-26, Flav7, and IR-27, respectively). While all of the dyes have identical methine bridges, they differ in their heterocycle, which leads to large changes in quantum yield and absorption energy. For simplicity, we chose dye **2** to be chromophore *a*. When we plug in  $\frac{E_{g,a}}{\alpha_E} = 9107 \text{ cm}^{-1}$ ,  $\gamma_M = 1$ ,  $\frac{E_{ST}}{\alpha_E} = 298.7 \text{ cm}^{-1}$  and  $\frac{E_M}{\alpha_E} = 3000 \text{ cm}^{-1}$  into equation 2.11 or 2.44 and reproduced below,  $\kappa\alpha_E$  0.0014 cm, for this analysis.

IR-26 is the reddest chromophore in our dataset ( $\lambda_{max} = 1080$ ,  $\phi_F = 5 \times 10^{-4}$ ), while IR-27 substitutes the oxygen for sulfur in the heterocycle, resulting in a 93 nm blueshift and an increase in quantum yield  $\phi_F = 3.2 \times 10^{-3}$ . Previously, we hypothesized that the improvement in quantum yield arises from a decreased heavy atom effect, leading to lower intersystem crossing rates.<sup>26</sup> However, to fully assess this claim we need to deconvolute the effect of the change in  $E_g$  in resultant  $\phi_F$ . Using values defined above and  $\frac{E_{g,b}}{\alpha_E} = 100011 \text{ cm}^{-1}$  into equation 2.10 or 2.47 We find that the energy gap independent improvement factor for IR-26 to IR-27 of  $\xi = 0.9$ , i.e., IR-27 is 1.9 times ( $\xi + 1$ ) more emissive, even when adjusted for its blue-shifted energy gap, still an improvement, but considerably less impressive than the apparent  $\chi = 6$  improvement factor. Flav7 adds an additional dimethyl amino group and replaces sulfur in the IR-26 scaffold. These structural changes both increase the quantum yield to  $6.1 \times 10^{-3}$  and blue shift the chromophore 53 nm, leading to a direct improvement of  $\chi = 11.2$  in  $\phi_F$  relative to IR-26. However, the adjusted improvement is only  $\xi = 4.6$ .

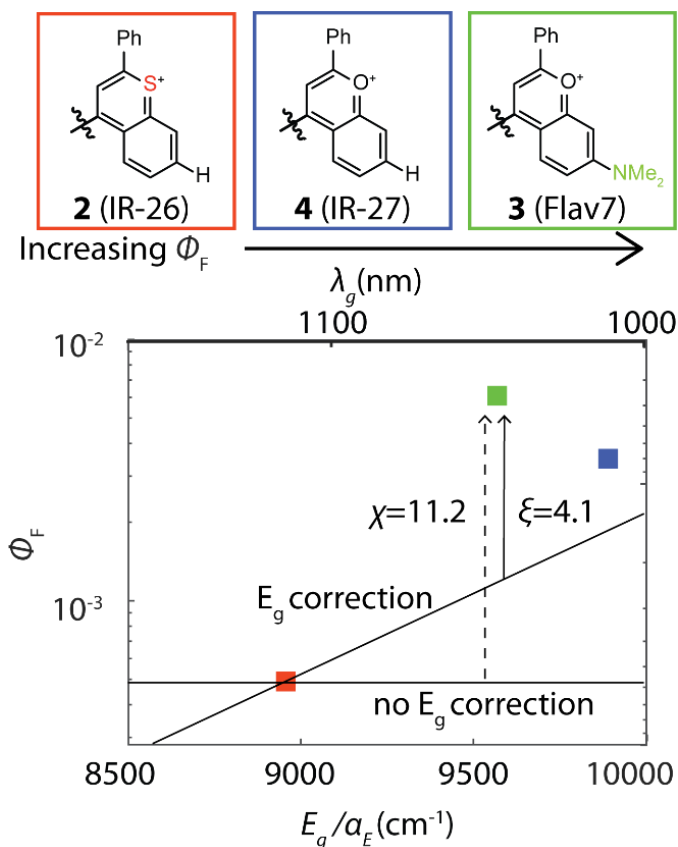


**Figure 2.15. Worked out example of the energy gap independent parameter.** IR-26, IR-27 and Flav7 show increasing quantum yields. To compare these dyes, we apply an energy gap independent comparator,  $\xi$ , which factors in the change in  $E_g$ .

### 2.5e.ii. Comparison relative to IR-27 (dye 4)

We compared all the dyes with an energy gap above 950 nm (7-methine family) in the main text to Dye 4 (Figure 2.16 and Table 2.3). These results confirm that the energy gap dependence can account for significant improvements in QY. We note that scaffolds that remove alkenyl C-H stretches compared to Dye 3, especially removal of the 2-position phenyl group (**5**, **6**), seem to improve even with energy gap.

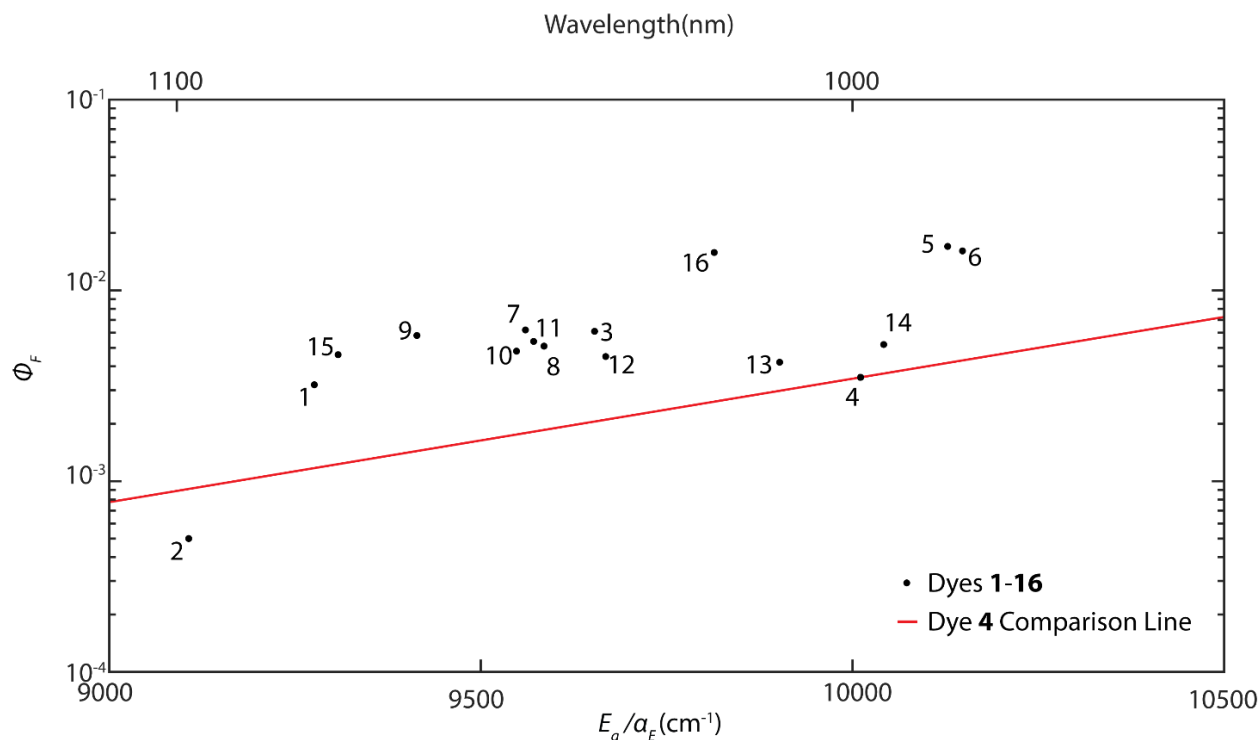


**Figure 2.16. Energy gap independent parameter using Dye 4 as the standard.** Simplified energy gap law assuming that dye 4 is the point of comparison for the 16 dyes analyzed in the manuscript table with values below.

## 2.5f. Overcoming Energy Gap Laws

### 2.5f.i. Enhancement from changing maximum vibrational stretch comparing parameters

We show how our methods of improvement changed depending on our pessimistic (scenario *P*) compared to our optimistic (scenario *O*) parameter. Given that only changing the maximum energy vibronic stretch impacted the location of maximum enhancement that is produced in Figure 2.14. Decreasing  $\gamma_m$  and  $C$  compared to scenario *P* both redshifted our peak enhancement to the red as well as decreasing the amount of enhancement (Figure 2.17). For the change in transition dipole, we see a similar trend, where the onset of the increase in enhancement is redshifted. Thus, experimental verification of  $\gamma_m$  and  $C$  is necessary to fully understand the full impact of changing the maximum vibrational character on quantum yield.



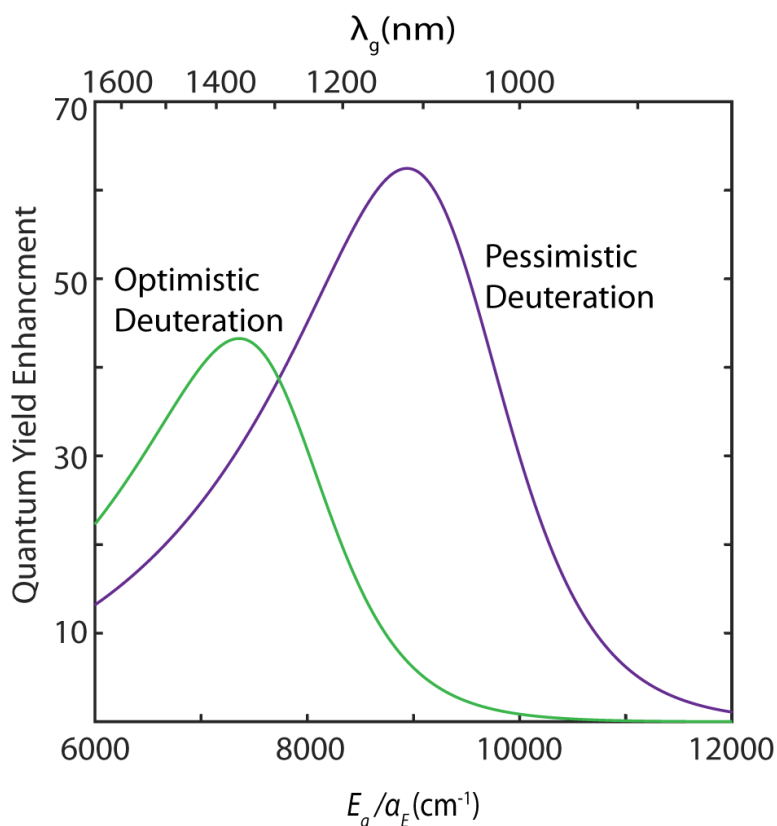


**Figure 2.17. Impact of deuteration based on different EQME conditions.** Enhancement by switching all  $E_{\text{vib}}$  from C-H stretch to C-D stretch for scenario O and P.

### 2.5f.ii. Synthesis and characterization of dye 3' and 3"

**General synthetic procedures.** Chemical reagents were purchased from Sigma-Aldrich (cyclohexanone, acetyl chloride and phosphoryl chloride), Fisher Scientific (solvents, sodium acetate and acetic anhydride), TCI America (aniline), and Cambridge Isotope Laboratory (deuterated compounds). 7-(Dimethylamino)-4-methyl-2-phenylchromenylium tetrafluoroborate (**S2**) was synthesized according to published procedure.<sup>34</sup> THF was dispensed from a Grubb's-type Phoenix Solvent Drying System constructed by JC Meyer. Nuclear magnetic resonance ( $^1\text{H}$  NMR,  $^{13}\text{C}$  NMR) spectra were taken on a Bruker DRX500 or AV500 spectrometer. All chemical shifts in  $^1\text{H}$  NMR and  $^{13}\text{C}$  NMR are reported in the standard notation of ppm relative to residual solvent

peak (DMSO- $d_6$  H=2.50, C=39.52). High resolution mass spectrometry was acquired on a Thermo Scientific Q Exactive™ Plus Hybrid Quadrupole-Orbitrap™ with Dionex UltiMate™ 3000 RSLCnano System. Absorption spectra were collected on a JASCO V-770 UV–visible/NIR spectrophotometer after blanking with the appropriate solvent. Photoluminescence spectra were obtained on a Horiba Instruments PTI QuantaMaster™ Series fluorometer equipped with InGaAs detector. Samples were dissolved in HPLC grade CH<sub>2</sub>Cl<sub>2</sub> and measured in Quartz cuvettes (2 mm × 10 mm) for absorption and photoluminescence measurements. All spectra were obtained at ambient temperature.

**Synthesis of *N*-((2-chloro-3-((phenylimino)methyl-*d*)cyclohex-2-en-1-ylidene)methyl-*d*)aniline hydrochloride salt (S1; Figure 2.18):** *N,N*-Dimethylformamide- $d_7$  (1.00 g, 12.5 mmol, 2.5 equiv.) was cooled in ice bath and phosphoryl chloride (1.0 mL, 11 mmol, 2.2 equiv.) was added dropwise. The mixture was stirred for 0.5 h to form a white, thick suspension. To this mixture was added cyclohexanone (0.52 mL, 5.0 mmol, 1.0 equiv.) and the mixture was heated at 90 °C for 1 h. After cooling to room temperature, aniline (0.91 mL, 9.9 mmol, 2.0 equiv.) was added and further stirred for 1 h. The dark red mixture was transferred into a separatory funnel, diluted with H<sub>2</sub>O (50 mL) and neutralized with NaHCO<sub>3</sub>. The aqueous phase was extracted with

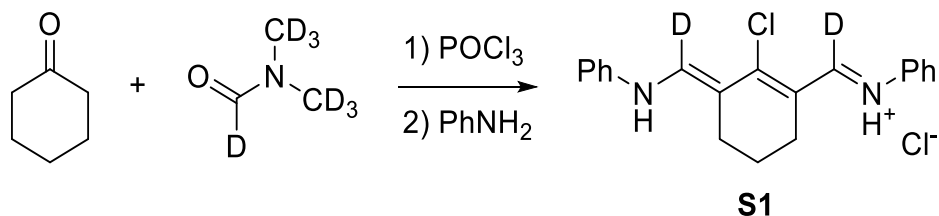


**Figure 2.18. Synthesis of S1.**

CH<sub>2</sub>Cl<sub>2</sub> (3 × 50 mL). The combined organic layer was dried (Na<sub>2</sub>SO<sub>4</sub>), concentrated and purified by column chromatography (1:10 ethyl acetate / hexanes). Collected yellow fractions were

acidified by dry HCl in MeOH prepared by dissolving acetyl chloride (0.36 mL, 10 mmol, 2.0 equiv.) in MeOH (5 mL), concentrated to dryness and further washed with diethyl ether to afford **S1** as a dark red solid (454 mg, 1.26 mmol, 25%).  $R_f = 0.7$  in 1:2 ethyl acetate/hexanes.  $^1\text{H}$  NMR (500 MHz,  $\text{DMSO-}d_6$ )  $\delta$  11.61 (s, 2H), 7.64 (d,  $J = 8.4$  Hz, 4H), 7.44 (q,  $J = 7.3$  Hz, 4H), 7.25 (t,  $J = 7.4$  Hz, 2H), 2.77 (t,  $J = 6.0$  Hz, 4H), 1.87–1.78 (m, 2H) (Figure 2.19).  $^{13}\text{C}$  NMR (126 MHz,  $\text{DMSO-}d_6$ )  $\delta$  139.6, 129.7, 126.2, 119.0, 114.9, 48.6, 24.9, 19.5. HRMS (ESI<sup>+</sup>)  $m/z$  calculated for  $\text{C}_{20}\text{H}_{18}\text{D}_2\text{ClN}_2^+$  [M+H<sup>+</sup>]: 325.1435, found 325.1433 (Figure 2.19).

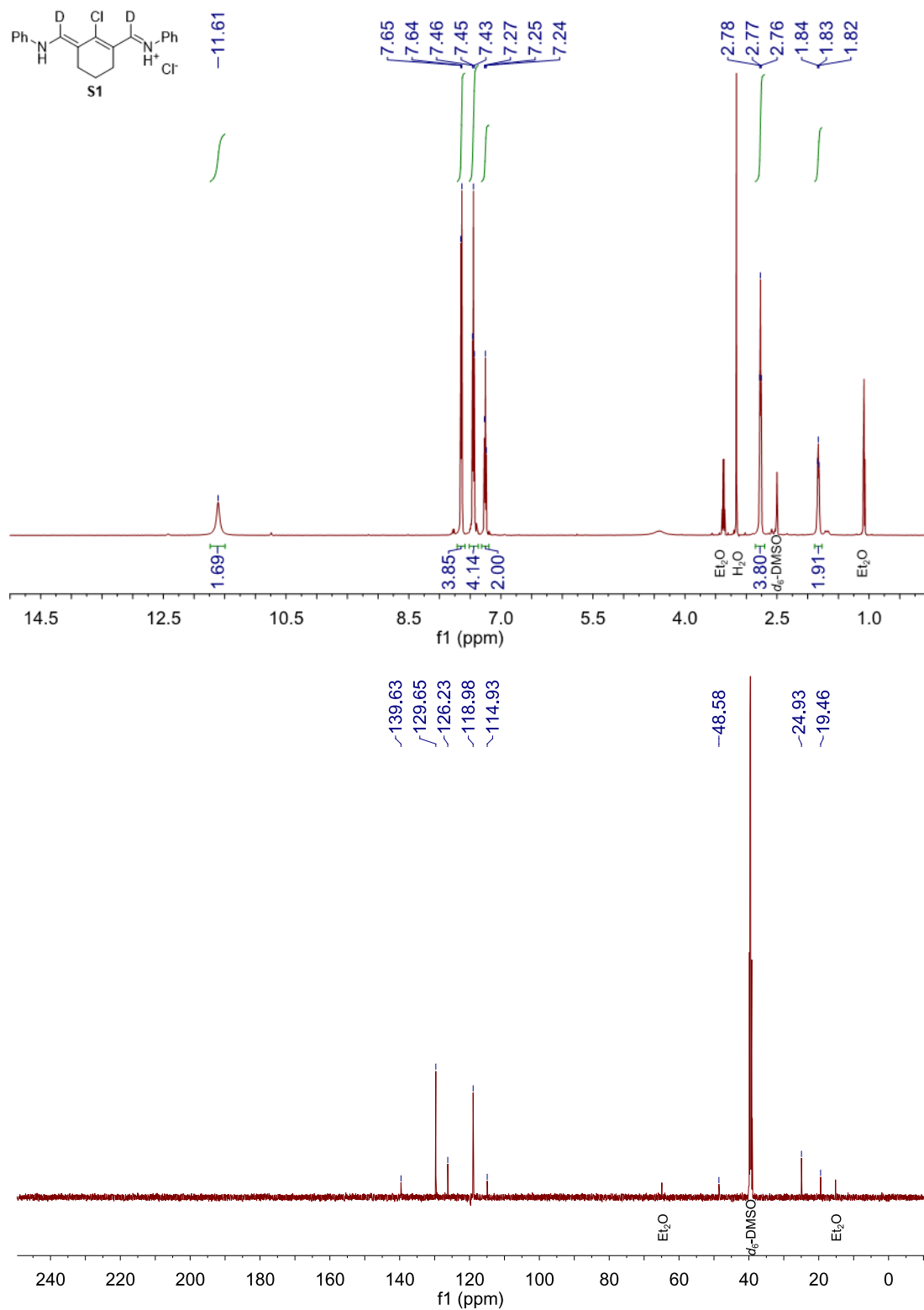
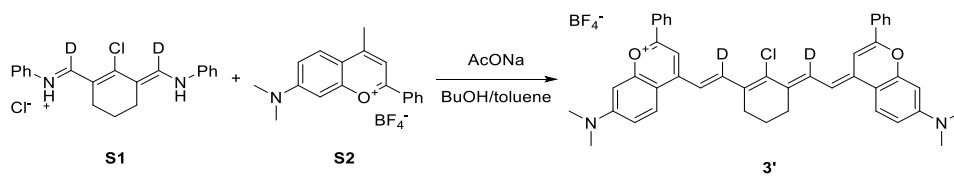


Figure 2.19. <sup>1</sup>H NMR of S1 (top) and <sup>13</sup>C NMR of S1 (bottom).

**Synthesis of 4-(2-(2-Chloro-3-(2-(7-(dimethylamino)-2-phenyl-4H-chromen-4-ylidene)ethylidene)cyclohex-1-en-1-yl)vinyl)-7-(dimethylamino)-2-phenylchromenylium tetrafluoroborate-*d*<sub>2</sub> (**3'**; Figure 2.20):** To a 4 mL vial containing **S1** (31 mg, 0.085 mmol, 0.45 equiv.), **S2** (66 mg, 0.19 mmol, 1.0 equiv.) and sodium acetate (46 mg, 0.56 mmol, 3 equiv.) was added 3:7 butanol / toluene (2 mL) followed by immediate freeze-pump-thaw × 3. The mixture was stirred at 100 °C under N<sub>2</sub>, cooled and concentrated to dryness. The dark mixture was separated by column chromatography (1:50 EtOH/CH<sub>2</sub>Cl<sub>2</sub>) to give **3'** as a dark purple solid (17 mg, 0.022 mmol, 27%). <sup>1</sup>H NMR (500 MHz, DMSO) δ 7.99 (s, 6H), 7.61 – 7.50 (m, 6H), 7.45 (s, 2H), 6.90 (s, 2H), 6.85 (d, *J* = 9.0 Hz, 2H), 6.65 (s, 2H), 3.08 (s, 12H), 2.76 (s, 4H), 1.88 (s, 2H). Absorbance (CH<sub>2</sub>Cl<sub>2</sub>): 523, 917, 1027 nm. Absorption coefficient  $\epsilon_{max} = (2.3 \pm 0.1) \times 10^5 \text{ M}^{-1}\text{cm}^{-1}$  (n = 2, average ± range) Emission (CH<sub>2</sub>Cl<sub>2</sub>, ex. 900 nm): 1053 nm (Figure 2.21). HRMS (ESI<sup>+</sup>) m/z calcd for C<sub>44</sub>H<sub>38</sub>D<sub>2</sub>ClN<sub>2</sub>O<sub>2</sub><sup>+</sup> [M<sup>+</sup>]: 665.2898, found 665.2907 (Figure 2.22).



**Figure 2.20. Synthesis of 3'.**

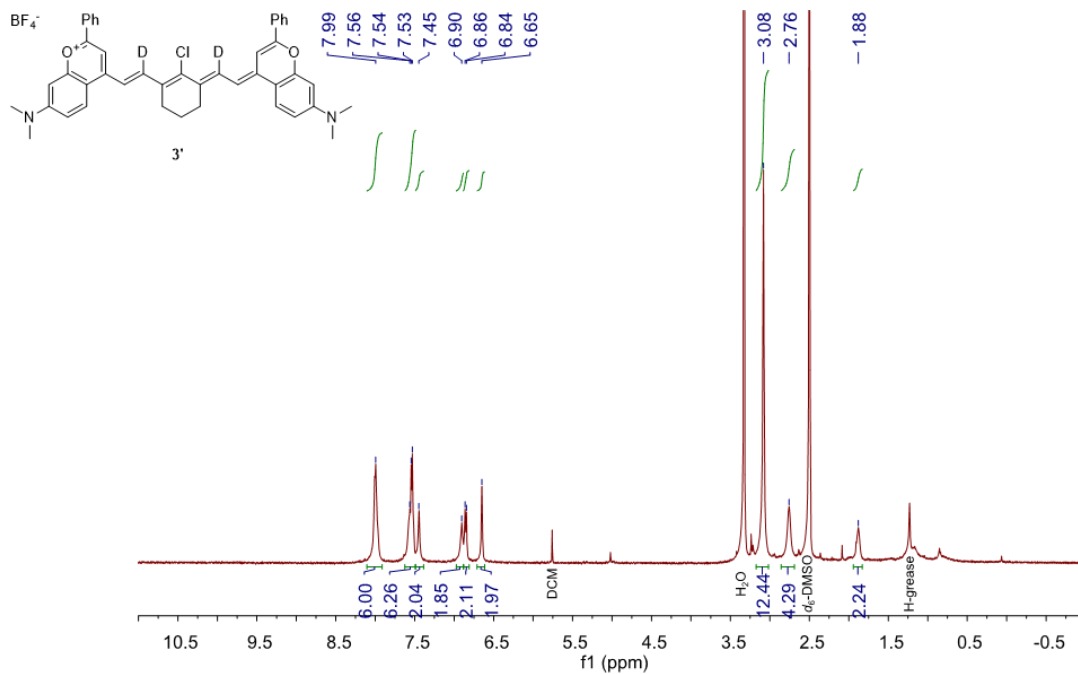


Figure 2.21. <sup>1</sup>H NMR of 3'.

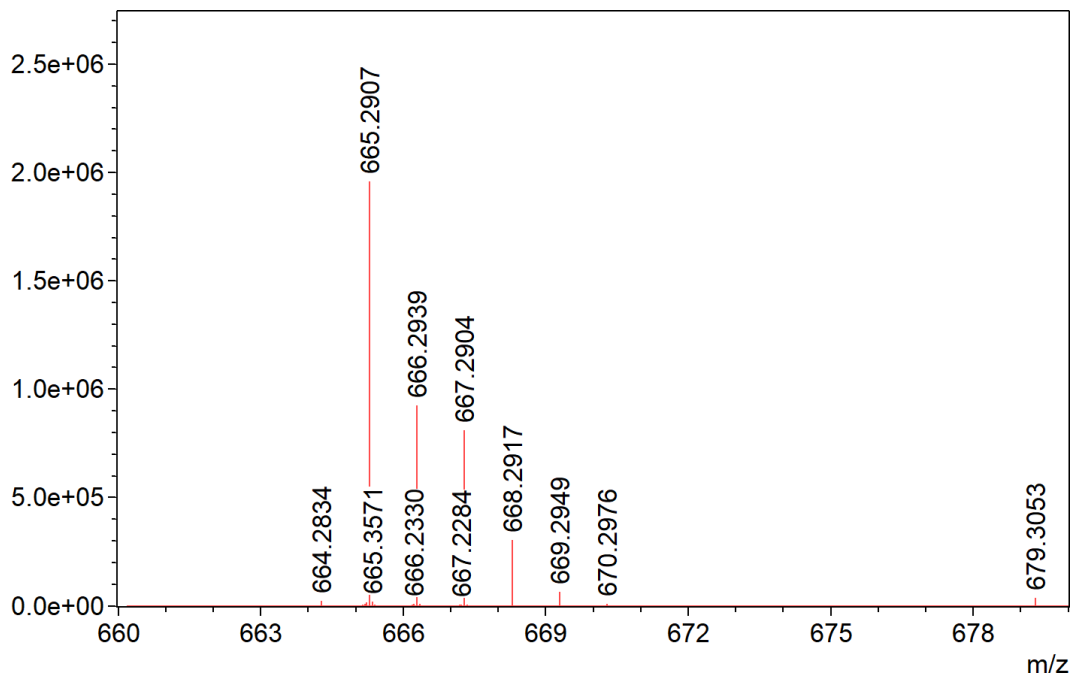
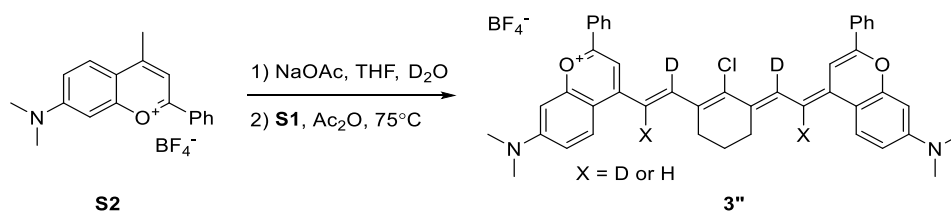


Figure 2.22. Mass spectra 3'.

**Synthesis of 4-(2-(2-Chloro-3-(2-(7-(dimethylamino)-2-phenyl-4H-chromen-4-ylidene)ethylidene)cyclohex-1-en-1-yl)vinyl)-7-(dimethylamino)-2-phenylchromenylium tetrafluoroborate-*d*<sub>2-4</sub> (**3''**); Figure 2.23): **S2** (50 mg, 0.14 mmol, 1.0 equiv.) and sodium acetate (35 mg, 0.43 mmol, 3.0 equiv.) were dissolved in D<sub>2</sub>O (1.3 mL) and dry THF (1.3 mL) followed by immediate freeze-pump-thaw × 3. The mixture was heated at 40 °C under N<sub>2</sub> for 4 h. The solvent was then lyophilized, and this procedure was repeated to maximize deuterium exchange. At this point, mass spectra suggest >80% methyl hydrogen atoms were exchanged to deuterium atoms. To the dried mixture was added **S1** (23 mg, 0.064 mmol, 0.45 equiv.) and acetic anhydride (3 mL) followed by immediate freeze-pump-thaw × 3. The mixture was stirred at 75 °C under N<sub>2</sub> for 15 min, cooled and concentrated to dryness. The dark mixture was washed with toluene and separated by column chromatography (1:75 EtOH/CH<sub>2</sub>Cl<sub>2</sub>) to give **3''** as a dark purple solid (8.0 mg, 0.011 mmol, 17%). *R<sub>f</sub>* = 0.5 in 1:10 EtOH/CH<sub>2</sub>Cl<sub>2</sub>. <sup>1</sup>H NMR (500 MHz, DMSO-*d*<sub>6</sub>) δ 8.17 (d, *J* = 6.3 Hz, 6H), 7.67 (s, 2H), 7.62 – 7.59 (m, 6H), 7.10 (s, 2H), 7.01 (d, *J* = 9.3 Hz, 2H), 6.86 (s, 2H), 3.16 (s, 12H), 2.87 – 2.81 (m, 4H), 1.93 – 1.87 (m, 2H). Absorbance (CH<sub>2</sub>Cl<sub>2</sub>): 524, 916, 1027 nm.  $\epsilon_{max} = (2.3 \pm 0.1) \times 10^5 \text{ M}^{-1}\text{cm}^{-1}$  (*n* = 2, average ± range). Emission (CH<sub>2</sub>Cl<sub>2</sub>, ex. 900 nm): 1056 nm (Figure 2.24). HRMS (ESI<sup>+</sup>) *m/z* calculated for C<sub>44</sub>H<sub>38</sub>D<sub>2</sub>ClN<sub>2</sub>O<sub>2</sub><sup>+</sup> [*M*<sup>+</sup>]: 665.2898, found 665.2903; isotopic pattern suggests 72% *d*<sub>2</sub>-, 15% *d*<sub>3</sub>- and 12% *d*<sub>4</sub>-product (Figure 2.25).**



**Figure 2.23. Synthesis of 3''.**

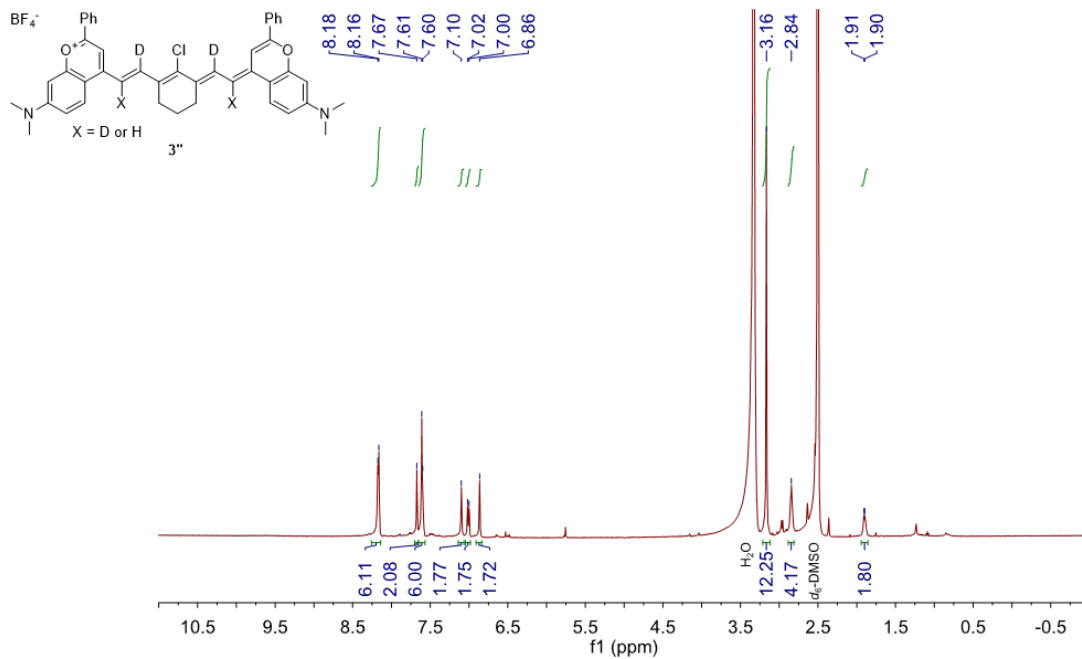


Figure 2.24. <sup>1</sup>H NMR of **3''**.

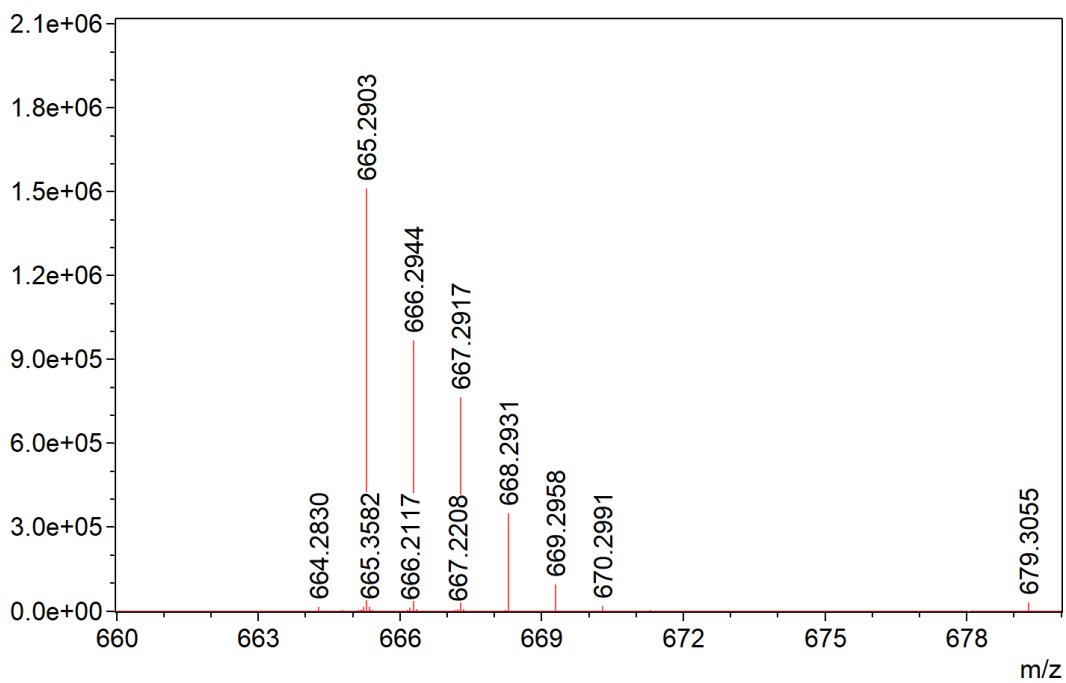
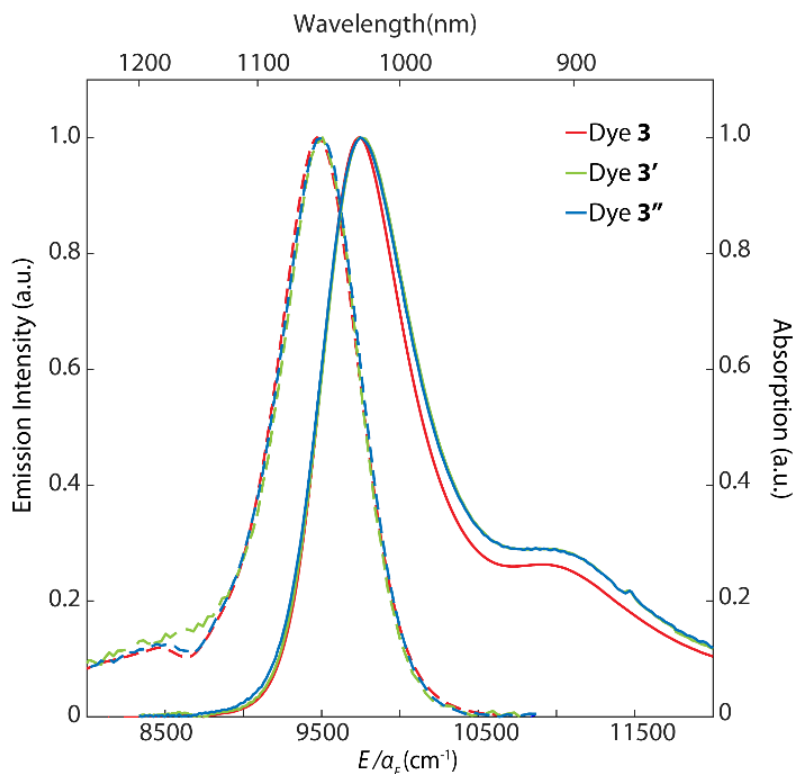


Figure 2.25. Mass spectra of **3''**.



### 2.5f.iii. Comparison of dyes 3, 3', and 3'' spectral properties

Absorption and emission data to compare how deuteration of the scaffold impacts spectral properties show good overlap near the HOMO-LUMO gap (Figure 2.26).



**Figure 2.26. Steady state spectra of dye 3, 3', and 3''.** Normalized absorption and emission of dye 3', and 3'' show a minimal peak shifting.

### 2.5f.iv. T-test and error propagation

For all t-tests, we used an independent samples t-test, with different variances. We used a population of one and the assumption that our error propagation in the text was for 95 percent confidence and used only one degree of freedom when converting the t-value. Additionally, for the total rate error, we used the confidence interval from the fitting. Table 2.6 shows the deviation used for the t-tests.

<b>Table 2.6. Errors Used in t-tests</b>			
<b>Dye</b>	<b><math>k_{\text{tot}}</math> error</b>	<b><math>k_r</math> error</b>	<b><math>k_{nr}</math> error</b>
<b>3</b>	$3.2 \times 10^7$	$2.9 \times 10^6$	$3.2 \times 10^7$
<b>3'</b>	$3.7 \times 10^7$	$4.5 \times 10^6$	$3.7 \times 10^7$
<b>3''</b>	$4.3 \times 10^7$	$7.0 \times 10^6$	$4.4 \times 10^7$

### 2.5g. 50% Quantum Yield Scaffold Comparison

To compare across scaffolds, we numerically solve for when EQME equals 0.5 i.e., when  $k_{nr} = k_r$ . For all points we use  $n = 1.5$ ,  $C = 1000 \text{ cm}^{-1}$ ,  $E_M = 3000 \text{ cm}^{-1}$ , and  $\gamma = 1$ . For the other dye classes, we found transition dipole moments using equation 2.3. Examples for each chromophore class are shown in Table 2.7.

<b>Table 2.7. Values of Other Dye Scaffolds for Comparison Method</b>			
<b>Dye Class</b>	<b>Dye</b>	$\mu_{12}$	$E_{ST} (cm^{-1})$
<b>Squaraines</b>			
	SQA <sup>68</sup>	10.6	190
	SQA2 -r <sup>68</sup>	13.3	100
<b>BODIPY</b>			
	BODIPY 2 Cl <sup>69</sup>	9.9	585
	BODIPY 2O <sup>69</sup>	8.5	571
	BODIPY 2 S <sup>69</sup>	9.2	570
	BODIPY 2Se <sup>69</sup>	9.6	580
	BODIPY 2Te <sup>69</sup>	8.5	776
	PM546 (BODIPY) <sup>67</sup>	7.1	461.4
<b>Fluorescein</b>			
RFL	butyl <sup>70</sup>	8.5	806
	5COOH <sup>70</sup>	8.1	916
	6 COOH <sup>70</sup>	8.1	806
	5 SCN <sup>70</sup>	8.0	1013
	SCN <sup>70</sup>	8.0	973
FLX2	Cl <sup>70</sup>	8.2	840
	Br <sup>70</sup>	8.2	843
	I <sup>70</sup>	8.5	769
	H <sup>70</sup>	8.3	843
FLX4	Cl <sup>70</sup>	8.2	639
	Br <sup>70</sup>	8.5	802
	Br Na Et <sup>70</sup>	8.7	738
	I <sup>70</sup>	8.6	827
R4FLX4	R=Cl X=H <sup>70</sup>	8.6	639
	R=Cl, X=I <sup>70</sup>	8.7	623
	R=Br, X=Cl <sup>70</sup>	9.5	704
	R=H, X=Cl <sup>70</sup>	8.4	639

### 2.5h. Solvent Deuteration Impact on Fluorescence Lifetime.

To analyze O-H overtone stretch impact on lifetime of a SWIR polymethine dye, we took fluorescence lifetimes of IR-1061 in ethanol (EtOH) and ethanol-d<sub>1</sub> (EtOD) with 785 laser light (IRF, 80 ps, Figure 2.27). Deuteration of the O-H stretch increased the lifetime from  $14 \pm 1$  to  $25 \pm 1$  ps is in part indicative of suppression of nonradiative rate. Quick photodegradation of IR-1061 made relative quantum yield measurements difficult.

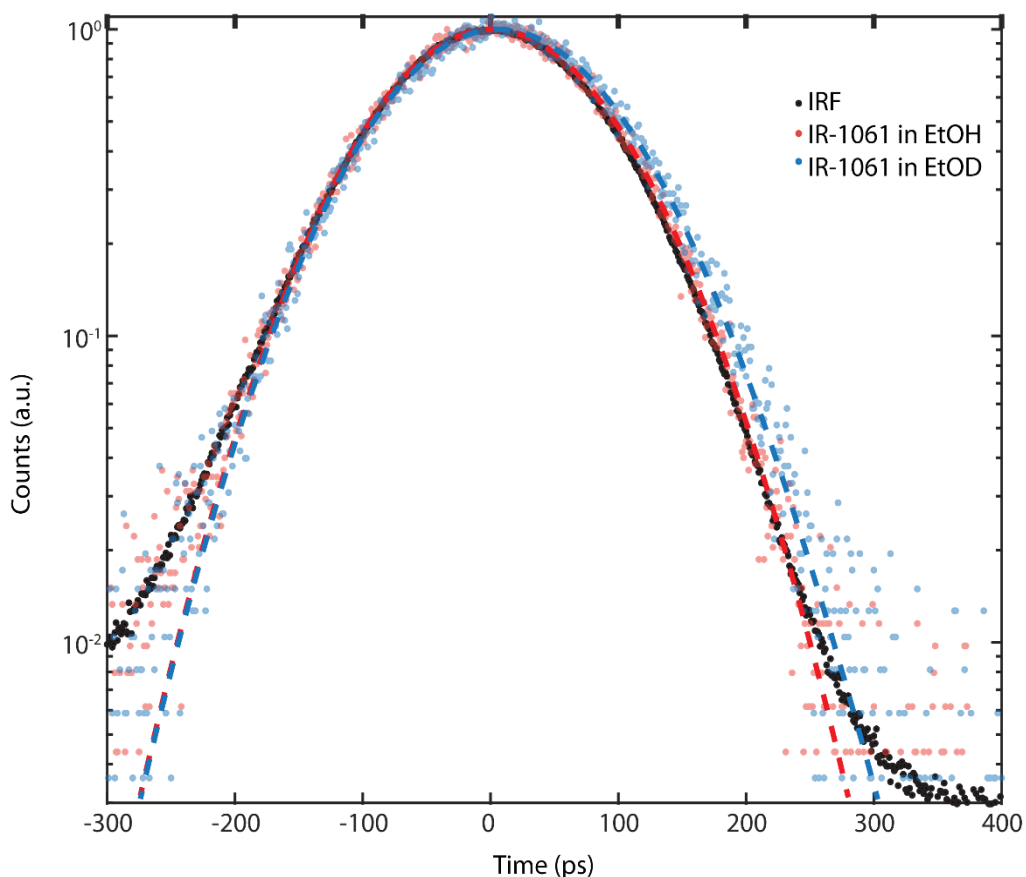


**Figure 2.27. Impact of solvent deuteration on fluorescence lifetime.** Graph represents fluorescence lifetime of IR-1061 in ethanol and ethanol-d<sub>1</sub>.

## Chapter 3

# The Optimization Problem for Shortwave Infrared

## Fluorescence Chromophores

### 3.1 Introduction

Penetrative biological fluorescence imaging requires two considerations, the ability of light to excite the chromophore of interest, and the amount of emitted light that exits the tissue without being absorbed or scattered. Shortwave infrared light (SWIR, 1000-2000 nm, Figure 3.1a) is privileged along both dimensions, owing to the decreased scattering of longer wavelength photons, and the lack of natural interfering sources of absorption and emission (autofluorescence). However, this lack of natural chromophores hints at the challenge of producing organic chromophores that fit the needs of the imaging community.<sup>87,88</sup> Simply put, the design parameters that govern highly redshifted electronic absorption and high quantum yield emission are non-obvious, and often unpredictable.

This chapter aims to provide a chemical physics informed basis of comparison of brightness across different fluorophore classes which access the near or shortwave infrared, with a focus on the photophysical constraints required by penetrative biological imaging. We focus very broadly on the question of chromophore “brightness”, a quantity defined as the maximum absorption cross section ( $\epsilon_{max}$ ) multiplied by the quantum yield ( $\phi_F$ ). Brightness (here  $\Omega_{max}$ ) is a valuable metric for *in vivo* imaging because it connects volume/dosage of fluorophore to the subsequent photon economy, i.e., the input/output of photons in an imaging system. Our goal is to illustrate the interplay between energy gap,  $E_g$ , vibrational relaxation energy, transition dipole

moment,  $\mu_{21}$ , and to discuss design strategies and tradeoffs for maximizing brightness (Figure 3.1b). Chromophore photophysics is defined by measured quantities, including structure/molecular weight, absorption spectrum, Stokes shift, fluorescent lifetimes and quantum yields. Relating foundational properties to each of these parameters is a requirement of optimizing imaging materials.

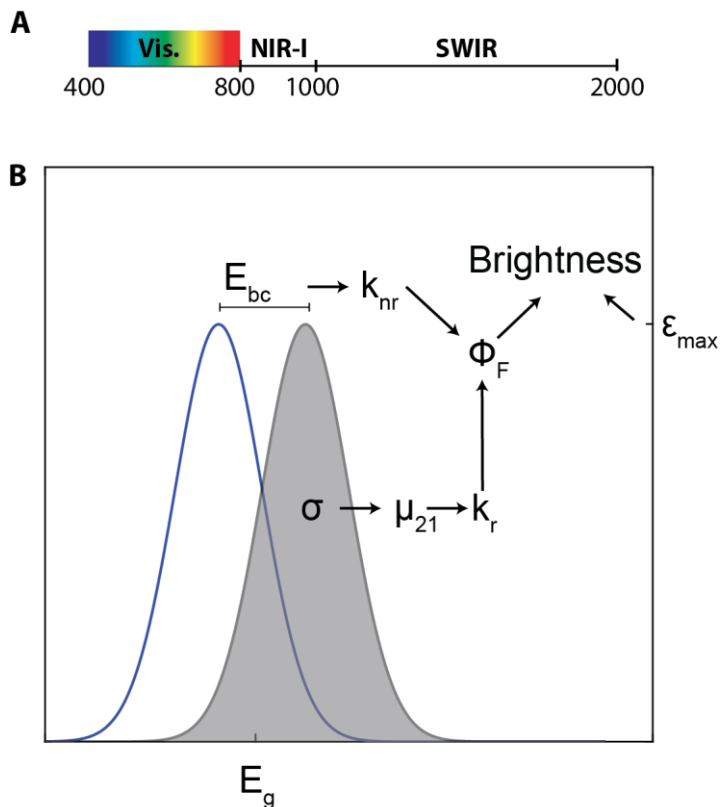


**Figure 3.1. Introduction to brightness in the NIR/SWIR.** (a) Representation of the Vis-NIR-SWIR spectra in nanometers. (b) Illustration of absorption and fluorescence spectra assuming that they are Gaussians and the pathway from steady state measurements to brightness.

## Select NIR/SWIR Fluorophores

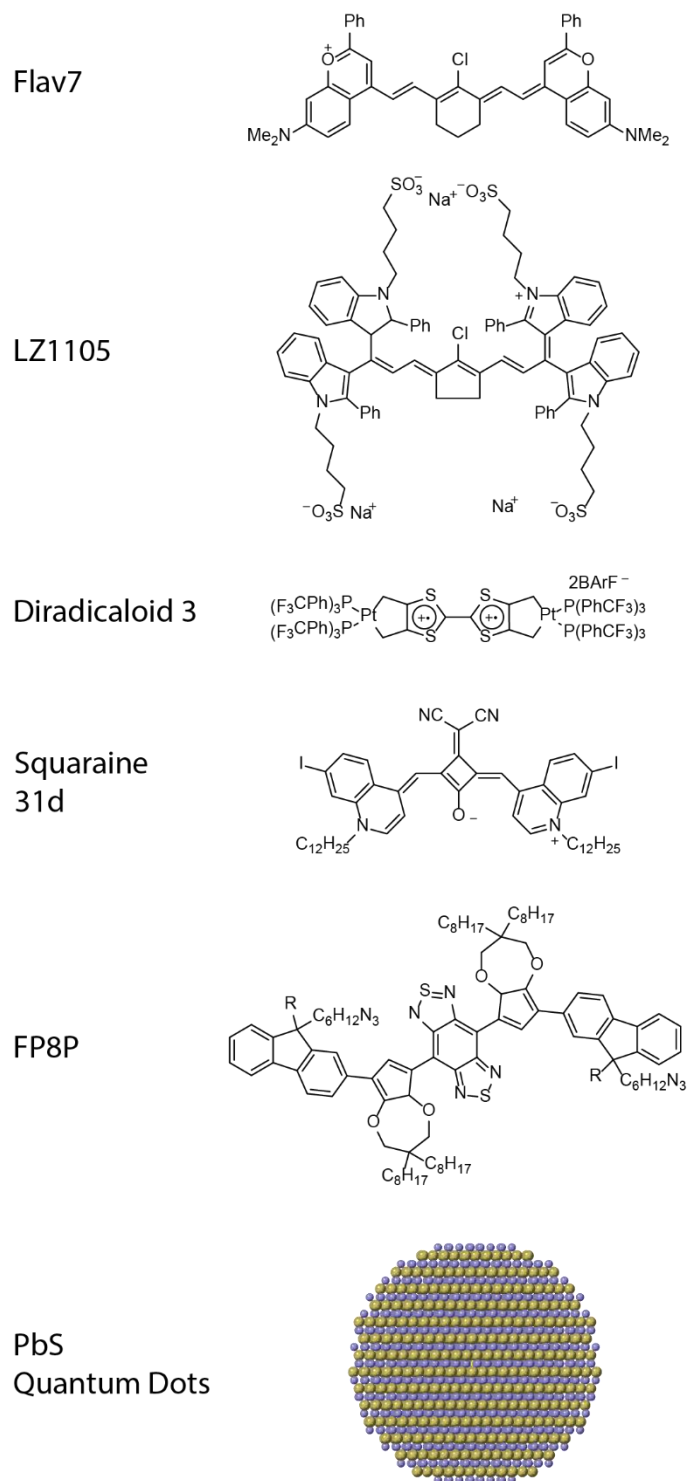


**Figure 3.2. Structures of NIR/SWIR fluorophores.**  
Structures of NIR/SWIR dyes discussed in Table 3.1.

Different organic SWIR chromophore frameworks are illustrated in Table 3.1 and Figure 3.2. Flav7 and LZ-1105 are polymethine dyes, with sub-1000  $cm^{-1}$  Stokes shift. 31d is a squaraine dye with even smaller Stokes shift than the polymethine dyes. The donor-acceptor dye (DAD), IRFP8P, and diradicaloid 3 have much larger Stokes shifts than squaraine or polymethine dyes. Lead sulfide (PbS) quantum dots have orders of magnitude higher quantum yields compared to organic chromophores in the SWIR but lower molar absorption coefficients at the first excitonic peak than polymethine and squaraine dyes, especially when normalized by unit cell. Immediately, a few trends appear obvious. For organic dyes, the Stokes shift is inversely correlated with higher brightness, with Flav7, LZ-1105, and the squaraine 31d having a  $\Omega_{max}$  at least an order of magnitude larger than the donor-acceptor and diradicaloid dyes, due to a higher  $\epsilon_{max}$ . Lead sulfide nanocrystals with higher quantum yields still have higher brightness than organic chromophores, on a per dot basis, but their brightness on a per unit cell level is closer to that of the diradicaloid and donor-acceptor dyes. This chapter will primarily focus on organic chromophores given their applicability to *in vivo* applications.



**Table 3.1. Photophysical Properties of Select NIR/SWIR Fluorophores of Different Classes**

Fluorophore	$E_g$ ( $cm^{-1}$ )	$\lambda_{max}$ ( $nm$ )	$E_{ST}$ ( $cm^{-1}$ )	$\epsilon_{max}$ ( $M^{-1} cm^{-1}$ )	$\phi_F$ ( $\times 10^{-2}$ )	$\Omega_{max}$ ( $M^{-1} cm^{-1}$ )	cit.
Flav7 (polymethine)	9617	1027	240	241000	0.61	1470	34
LZ1105 (polymethine)	9328	1041	556	101000	1.69	1710	52
Diradicaloid 3	9186	1023	1177	~80000	0.43	~343	89
31d (squaraine)	11063	897	171	271000	0.8	2170	7
IRFP8P (DAD thiophene)	11492	748	3754	13000	0.6	78	90
PbS (per dot at peak) (per unit cell)	9255	1130	766	88000 1060	27	22002 286	29,91

### 3.2 Defining Maximum Brightness

In its most fundamental form maximum brightness is:

$$\Omega_{max} = \epsilon_{max} \times \phi_F, \quad (\text{Eq. 3.1})$$

where:

$$\epsilon_{max} = g(E_{max}) \times \int \epsilon(E) dE, \quad (\text{Eq. 3.2})$$

and  $g(E)$  is a lineshape function and the integral is over the  $S_0 \rightarrow S_1$  transition:

$$\int \epsilon(E) = \frac{\log_{10} e N_A}{1000} \frac{g_2 \pi E_g}{3g_1 \epsilon_0 n \hbar^2 c} |\mu_{21}|^2. \quad (\text{Eq. 3.3})$$

To find a maximum value for  $\epsilon$ , we need to define a generic line shape function to approximate trends. We will use a single Gaussian to be agnostic to coupling to specific Frank-Condon modes (and other effects which are molecule specific):

$$g(E) = \frac{1}{\sqrt{2\pi\langle E^2 \rangle}} \exp \left[ -\frac{1}{2} \frac{(E - E_g - \langle E \rangle)^2}{\langle E^2 \rangle} \right]. \quad (\text{Eq. 3.4})$$

To use this, we must create an “equivalent” Gaussian lineshape that represents the absorption linewidth without considering specific high-frequency vibrations. We will thus assert the high temperature approximation, which asserts that the spectral shift on the excited state (the reorganization energy) is equal to the thermally averaged distribution of accessible vibrational states, i.e.,  $\langle E \rangle = \sqrt{\langle E^2 \rangle}$ . For this to work, we will define the reorganization energy as half the energy difference between the barycenters of absorption and emission,  $E_{bc}$  (contrary to our prior definition of  $\frac{1}{2}$  the Stokes shift,  $E_{ST}$ ).<sup>92</sup> The barycenters are the intensity averaged absorption/fluorescence energies which means it takes into account all vibrational states accessible. The difference between  $E_{bc}$  and  $E_{ST}$  in both value and effect on gaussian lineshape is illustrated in Figure 3.3. For Flav7 the value for  $E_{bc}$  is  $964.5 \text{ cm}^{-1}$ , while the  $E_{ST}$  is  $298.7 \text{ cm}^{-1}$  (Figure 3.3a). The “equivalent” Gaussian lineshape is:

$$g(E) = \frac{2}{E_{bc}\sqrt{2\pi}} \exp \left[ -2 \frac{\left( E - E_g - \frac{1}{2} E_{bc} \right)^2}{E_{bc}^2} \right]. \quad (\text{Eq. 3.5})$$

As we are only interested in the maximum value of brightness, the maximum value for this line shape function is:

$$g(E)_{max} = \frac{2}{E_{bc}\sqrt{2\pi}}. \quad (\text{Eq. 3.6})$$

We shall also recast the combined energy gap law from Chapter 2<sup>93</sup> using the barycenter definition:

$$\phi_F(E_g) = \left( 1 + K \frac{C^2}{n\mu_{21}^2 (E_M E_g^7)^{\frac{1}{2}}} \exp \left[ -\frac{E_g}{E_M} \left( \ln \frac{2E_g}{\gamma_M E_{bc}} - 1 \right) \right] \right)^{-1}, \quad (\text{Eq. 3.7})$$

where  $K = \left( \frac{3\epsilon_0 c^2}{(2^5 \pi^3)^{1/2}} \right)$ , highest energy vibrational stretch  $E_M = 3000 \text{ cm}^{-1}$ , and the proportion of  $E_{bc}$  due to  $E_M$ , is  $\gamma_M$  (which should be smaller using the barycenter definition).

Plugging in equations 3.2, 3.3, 3.6, plus the combined energy gap law equation (EQME, equation 3.7) into equation 3.1, we arrive at:

$$B_{max} = L \frac{\mu_{21}^4 (E_M E_g^9)^{1/2}}{E_{bc} \left( n \mu_{21}^2 (E_M E_g^7)^{1/2} + 3\sqrt{2\pi^3} \epsilon_0 (\hbar c)^3 C^2 \exp \left[ -\frac{E_g}{E_M} \left( \ln \frac{2E_g}{\gamma_M E_{bc}} - 1 \right) \right] \right)}, \quad (\text{Eq. 3.8})$$

where  $L = \frac{g_2 \sqrt{2\pi} N_A \log_{10} e}{g_1 3000 c \epsilon_0 \hbar^2}$ . Though both EQME and brightness will be dominated by the exponential dependence of nonradiative rate on  $E_g$ , brightness changes should be less stark than for quantum yield given the additional transition dipole moment and energy gap terms in the numerator. One can make some general observations about the tradeoffs in brightness. Firstly, smaller barycenter shifts have stronger than an inverse relationship with brightness, influencing both the nonradiative rate and the linewidth (and thus the maximum absorption cross section). Second, increasing transition dipole moments ( $\mu_{21}$ ) will increase brightness's dependence on transition dipole moment from quadratically to quartically, depending on the energy gap and highest frequency mode. Taken together, this strongly implies high transition dipole moments and small Stokes shifts should be privileged for achieving a high brightness for a given energy gap. This notion is supported by in-extant chromophores (see Table 3.1).

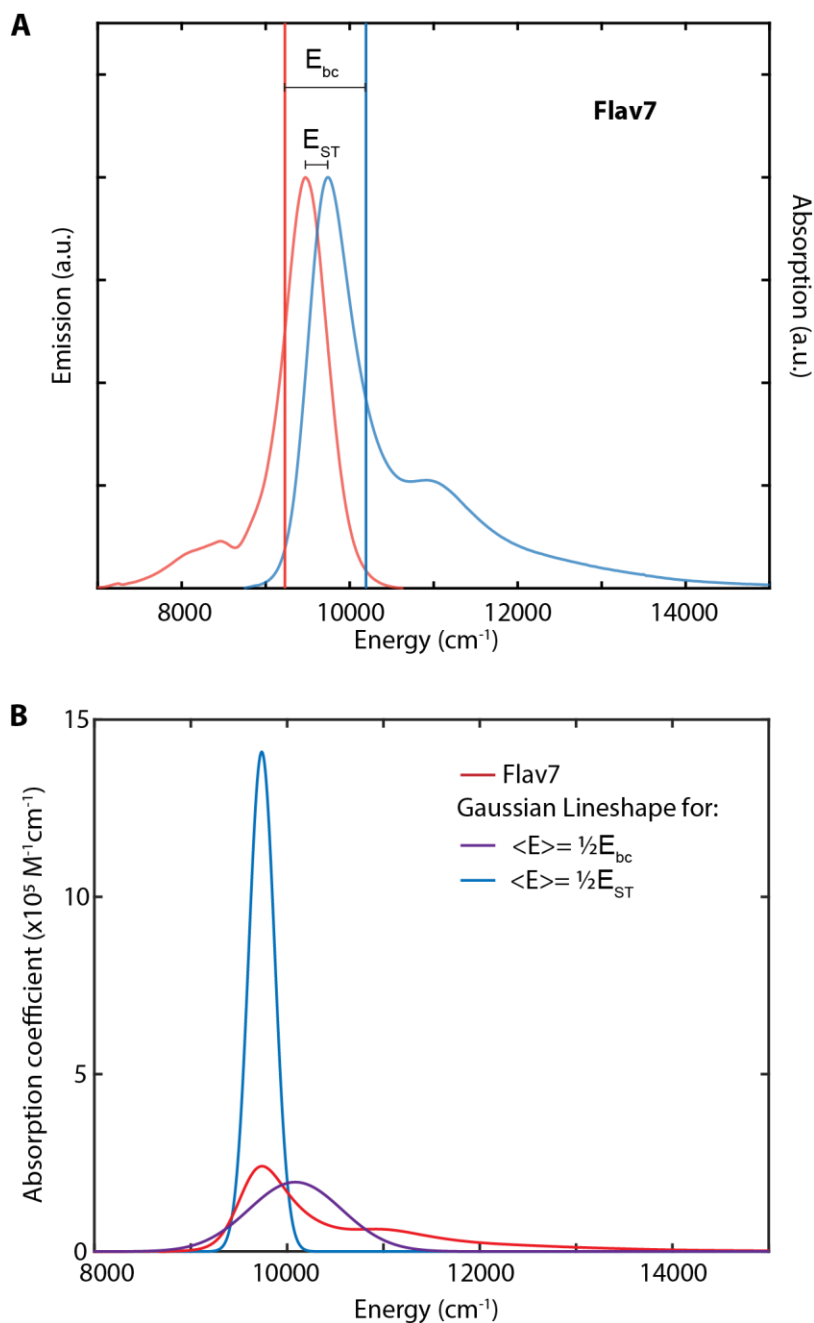


**Figure 3.3.  $E_{ST}$  and  $E_{bc}$  and their impact on “equivalent” Gaussian lineshape.** (a) Illustration of the difference between  $E_{bc}$  and  $E_{ST}$  for Flav7 absorption and emission spectra. (b) Comparison of absorption of Flav7 to an “equivalent” Gaussian lineshape under the assumption that vibrational reorganization energy is  $0.5E_{bc}$  or  $0.5E_{ST}$ . The use of  $E_{bc}$  provides a more comparable  $\epsilon_{max}$  to the experimental absorption.

### 3.3. Using “Particle in a Box” to Determine $\mu_{21}$

In Chapter 2, we observed a relationship between electron donating character on both the bandgap and transition dipole moment of 7-methine flavylum polymethine dyes, both following a “particle in a box”-like behavior. Here, we add a discussion of how treating molecules within this limit affects brightness. We adapt Kuhn’s “particle in a box” analysis for symmetric cyanine dyes with the trans configuration along the polymethine chain.<sup>8</sup> This model assumes the cyanine limit or that there is no symmetry breaking with longer chains, which leads to more polyene character in the molecular system.<sup>94</sup> Both symmetry breaking and cis-structural components will lead to lower values for transition dipole moments. First, the energy gap for the “particle in a box” is as follows:

$$E = \frac{h^2}{8mN^2l^2} (N + 1), \quad (\text{Eq. 3.9})$$

and the transition dipole moment is:

$$\mu_{21} = \frac{4e_c N l}{\pi^2} \cos\left(\frac{\beta}{2}\right) \frac{N(N + 2)}{(N + 1)^2}, \quad (\text{Eq. 3.10})$$

where  $N$  is the number of  $\pi$  electrons in the transition,  $l$  is  $1.39 \times 10^{-8} \text{cm}$  or the bond length of chained elements with a bond number of 1.5, and  $\beta$  is the difference of the bond angle from  $180^\circ$  or  $56^\circ$ . We can relate the number of double bonds in a polymethine chain to the number of  $\pi$  electrons as  $j = \frac{N}{2} - 1$ .

Unsurprisingly, based on the relationship between the energy gap and the number of  $\pi$  electrons or double bonds, 7-methine chromenylium dyes are between  $j = 7$  to 8, where the

shortest path counting the 7-methine chromenylium family is  $j = 7$ , while a 7-methine cyanine structure would have  $j = 5$ . This further supports the previous assumption that the chromenylium ring donates additional electrons than a cyanine of comparable methine bridge length. Using equations 3.8 and 3.10, we can estimate the maximum brightness given a specific energy gap (Figure 3.4). For a constant  $E_{bc} = 964.5 \text{ cm}^{-1}$ , brightness peaks in the red of the electromagnetic spectrum at  $15312 \text{ cm}^{-1}$  or approximately 11 electrons in the transition, corresponding to a Cy7 dye.

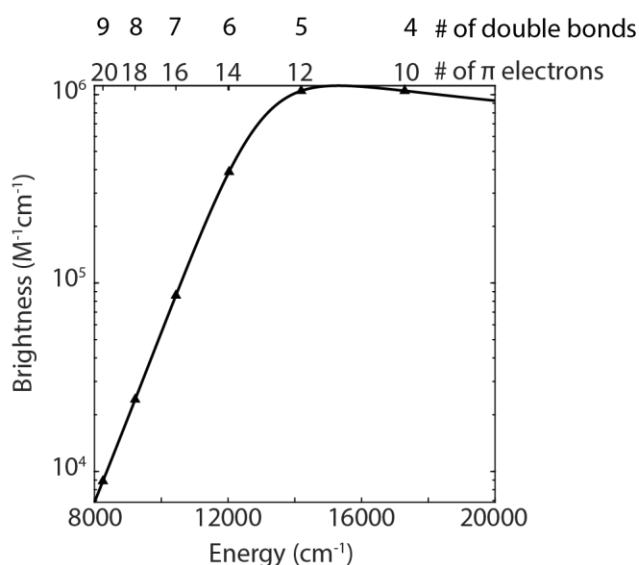


**Figure 3.4. Impact of brightness based on energy using Kuhn’s “particle in a box” model.** Dyes are assumed to remain in the cyanine limit and a constant  $E_{bc}$  of  $964.5 \text{ cm}^{-1}$ . Brightness under these conditions maximizes around 5 double bonds.

### 3.4. Maximizing Quantum Yield and Brightness for a Specific Energy of Fluorescence

One key difference between dye types is changes in vibrational displacement. In prior work we have characterized this as a proportion of the total Stokes shift, which is a more accessible value in the literature. Here, we ask the question, for a fixed emission energy: *Does having a larger*

Stokes shift (and thus smaller  $E_g$ ) outweigh the other energy gap laws that contribute to decreased photoluminescence in the SWIR? Herein, we shall assume that all our molecules will be Gaussian in character such that  $E_{ST} = E_{bc}$  for the sake of this simple model and thus  $E_g = E_F + \frac{1}{2}E_{bc}$ . We calculate the nonadiabatic coupling or C in equation 3.9 as is done in Chapter 2. Using  $E_{bc}$  instead of  $E_{ST}$  leads to  $C = 263 \text{ cm}^{-1}$  which will be kept constant. In Figure 3.5, we show the effect of  $\gamma_M$  (the proportion of  $E_{bc}$  from the maximum vibrational energy  $E_M$ ), fluorescence energy, and the treatment of transition dipole moment (as either a constant or following Kuhn's formalism as described in Section 3.3). First, our hypothesis that either  $\phi_F$  or maximum brightness will be higher for larger select  $E_{bc}$  only held for  $\phi_F$  at very small  $\gamma_M$  (Figure 3.5). To put the amount of coupling of the maximum vibrational mode to  $E_{bc}$  shift into perspective, the coupling would equal  $\gamma_M \times E_{bc,Flav7} = 48 \text{ cm}^{-1}$  in energy or would have a Huang Rhys factor, S, of 0.008, which is small. Even without an inflection point, quantum yield and brightness are most impacted by changes in  $E_{bc}$  at smaller values of  $E_{bc}$ . In Figure 3.5, we include a line representing the  $E_{bc}$  of Flav7 to represent the  $E_{bc}$  of a molecule with smaller vibrational reorganization energy. This shows that at higher  $E_{bc}$  the trade-off between increasing the separation of the absorption and emission energies and loses to quantum yield and brightness diminishes, which may be worthwhile in some applications.

*Within a scaffold type how can we adjust Stokes shift?* For symmetrical polymethine dyes, substitution off the polymethine backbone with an amine group changes the Stokes shift by tuning the ratio between cyanine-like and bis-dipolar confirmations.<sup>95,96</sup> This method will also impact the transition dipole moment, such that increasing the Stokes shift or the adiabatic vibronic coupling with also deleteriously impact the brightness for both the radiative and nonradiative rates. Next we will discuss a proposed pathway for decreasing vibrational reorganization energy.

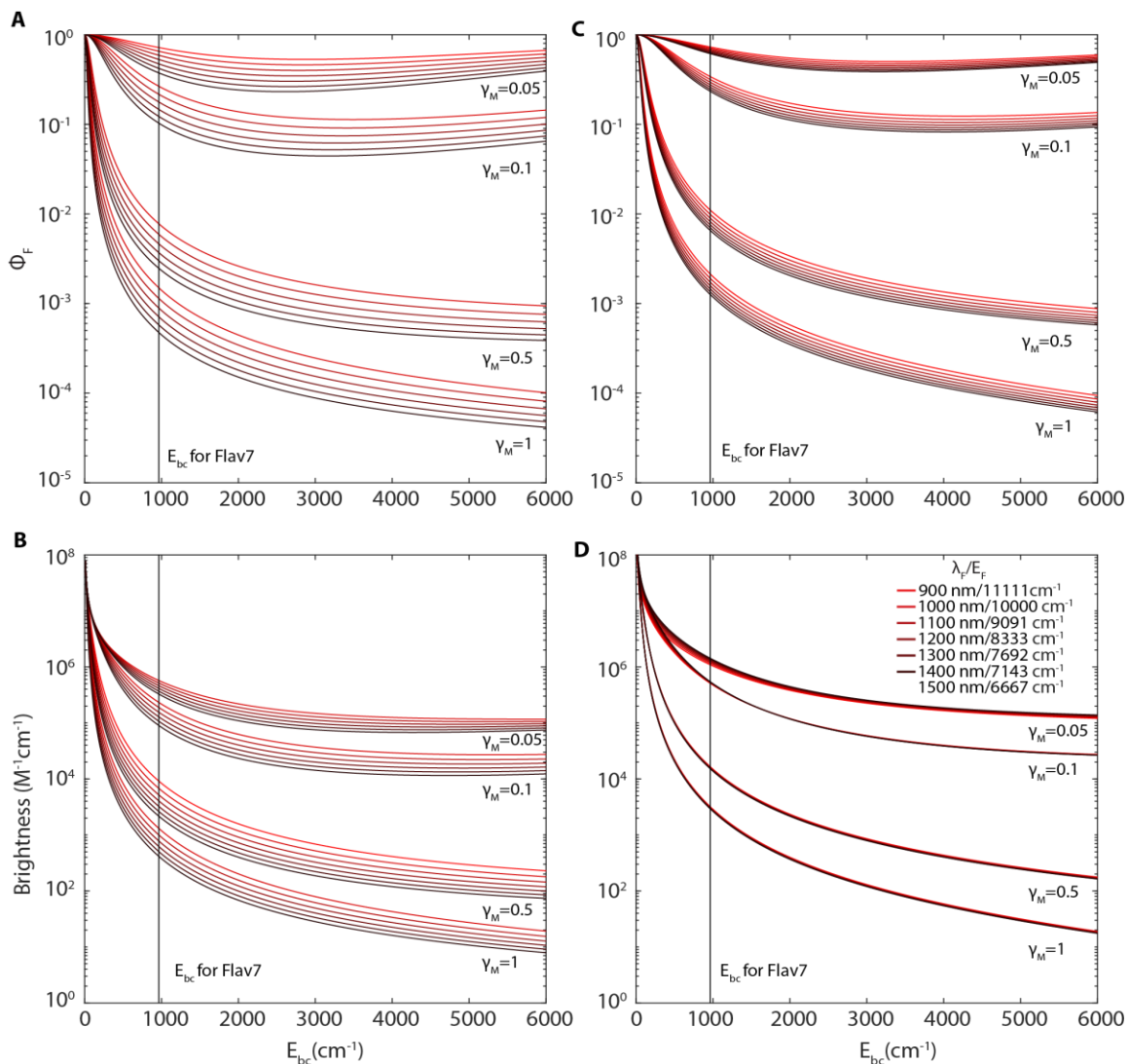


**Figure 3.5. Overall brightness and quantum yield are maximized at small vibrational displacements.** Quantum yield and brightness with respect to different  $E_{bc}$  for a set  $E_F$  for constant  $\mu_{21} = 18 D$  (a,b) and for  $\mu_{21}$  solved from equation 3.10 (c,d). Overall, for smaller  $\gamma_M$ , the decrease with respect to  $E_{bc}$  shallows toward an inflection point. Additionally, energy gap dependence on  $\mu_{21}$  decreases the difference between different  $E_F$  on final  $\Omega_{max}$  and  $\phi_F$ .



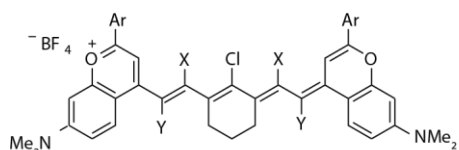
### 3.5. Deuteration Impacts on Brightness

	$E_g$ ( $cm^{-1}$ )	$E_{ST}$ ( $cm^{-1}$ )	$\varepsilon_{max}$ ( $M^{-1} cm^{-1}$ )	$\Omega_{max}$ ( $M^{-1} cm^{-1}$ )	$\phi_F$ ( $\times 10^{-2}$ )	cit.
<b>Flav7<sup>a</sup></b>	9617	267.7	240000	$1470 \pm 50$	0.61	<sup>93</sup>
<b>Flav7-m-d2<sup>a</sup></b>	9626	267.7	230000	$1449 \pm 93$	0.63	<sup>93</sup>
<b>Flav7-m-d2.12<sup>a</sup></b>	9626	267.7	230000	$1518 \pm 137$	0.66	<sup>93</sup>
<b>Flav7-Ar-d10<sup>a</sup></b>	9630	213	— —	— — —	0.67	
<b>ICG<sup>b</sup></b>	12386	383.5	224000	$37000 \pm 5550$	16.7	<sup>97</sup>
<b>ICG-d5<sup>b</sup></b>	12410	400.3	253000	$49000 \pm 7350$	19.8	<sup>97</sup>
<b>ICG-d7<sup>b</sup></b>	12410	369.5	228000	$48000 \pm 7350$	20.8	<sup>97</sup>

<sup>a</sup>DCM is used as solvent. <sup>b</sup>DMSO is used as solvent.

Another proposed way to impact the vibrational reorganization energy is through deuteration by reducing the number of high energy C-H vibrational modes. Deuteration of the polymethine scaffold in dyes have previously shown slight improvements in quantum yield and brightness.<sup>93,97</sup> Interestingly for all scaffold-based deuterium substitution in both ICG and Flav7 there is no trend in a change of Stokes shift, which here we will use as the steady state proxy for vibrational coupling. Thus, more nuanced vibrational analysis may help elucidate these deviations via resonance Raman or femtosecond coherence spectra.<sup>98</sup> To further test prior work that C-H vibrations that take part in the transition are privileged,<sup>64</sup> we designed a Flav7 dye with the phenyl rings deuterated, Flav7-Ar-d10, instead of along the polymethine scaffold, Flav7-m-d2 and Flav7-m-d2.12 (Figure 3.6 a). In this case, we still observe an increase in quantum yield upon deuteration. Similarly, Flav7-Ar-d10's total decay rate ( $1.4 \times 10^{10}$ ) and its nonradiative rate are the only two rates that are statistically different compared to the entirely protonated Flav7 (Figure 3.6). However, for Flav7-Ar-d10, the quantum yield, nonradiative rate, and total decay rate are only slightly higher than the Flav7-m-d2.12 dye. This slight improvement, despite more deuterium inclusion in Flav7-Ar-d10, is indicative that the deuterium inclusions on the scaffold are more

important to vibrational coupling associated with internal conversion (Figure 3.6). On the other hand, for rhodamines and other small molecules, deuteration of the amino groups attached to the 3 and 6 position on the xanthene backbone increases the molar absorption coefficient, quantum yield or both. This is through the reduction of electron donation strength of the substituent suppressing the twisted internal charge transfer or the stronger C-D bond decreasing dealkylation.<sup>99</sup> To test for suppression of twisted internal charge transfer, temperature dependent fluorescent and time resolved photoluminescent measurements need to be done. To study the possible impact of electron donating strength of substituents on the 2- position of the flavylum ring, synthesis of 2-position derivatives and photophysical analysis like those reported for the 7-substitution on the flavylum ring in Chapter 2 would be required. Overall, deuteration appears to be a fruitful design for incremental improvements of current dyes.



Flav7	X=H	Ar=Ph	Y=H
m-d2	X=D	Ar=Ph	Y=H
m-d2.12	X=D	Ar=Ph	Y=H (88%) or D (12%)
Ar-d10	X=H	Ar=Ph-d5	Y=H

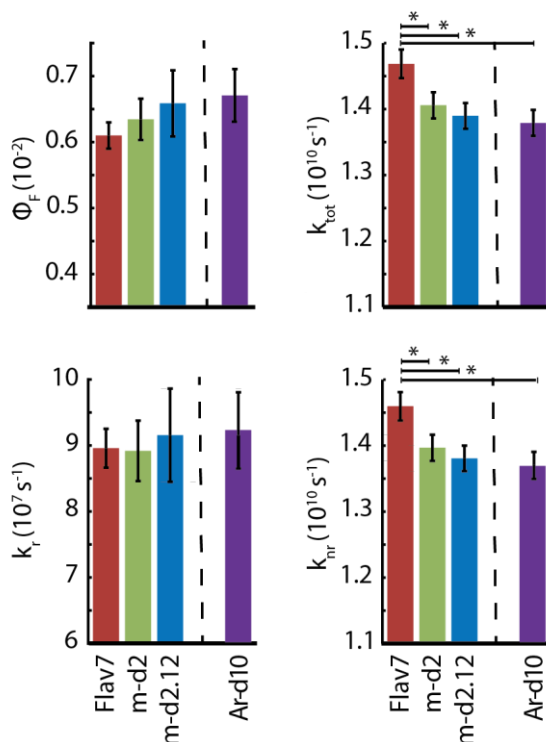


**Figure 3.6. Deuteration of Flav7 and the impact on quantum yields and lifetimes.** (a) Structure of Flav7 and its deuterated derivatives. (b) Bar graphs comparing the quantum yield,  $\phi_F$ , total rate,  $k_{tot}$ , radiative rate,  $k_r$ , and nonradiative rate,  $k_{nr}$ , of Flav7 and its derivatives. Dotted line designates that Flav7-Ar-d10 is added onto a previous figure from Chapter 2. The asterisk indicates that the difference between dyes is significant  $p < 0.05$ .

### 3.6. Conclusions

Overall, high  $\mu_{21}$  and small vibrational reorganization energy that improve quantum yields also improve brightness. For molecules like cyanine dyes that have “particle in a box” character, we found a point at which brightness will maximize when keeping other molecular parameters constant. Deuteration as a method to improve quantum yield, similarly, only slightly improves molecular brightness. Studying resonance Raman and femtosecond coherent spectroscopy will provide greater insight to identify the C-H stretches most important to the process of internal conversion.<sup>98,100,101</sup> We reaffirmed that Stokes shift, though often important in fluorophore choice for imaging considerations, does not always accurately represent total vibrational reorganization energy. Analysis of quantum yield and brightness for set fluorescence energy by varying  $E_{bc}$  shows that decreasing  $E_{bc}$  always improves quantum yield and brightness. However, the impact lessens at higher  $E_{bc}$ , implying that once a certain barycenter (or Stokes shift) is observed, it may not be worth making changes to the compound that optimize  $E_{bc}$  for that scaffold to improve quantum yield and brightness. This is useful since a bright dye with well separated absorption and emission peak can be an important optimization parameter for some imaging applications.

## Chapter 4

### Challenges and Collaborations

#### 4.1. Toward Temperature Dependent Photophysics

One continuing direction of this work proposes to understand the temperature dependence of quantum yield, radiative, and nonradiative rates in the shortwave infrared to check some of the assumptions made in Chapter 2 in the fundamental equations. According to Englman and Jortner's assumptions, the internal conversion of the polymethine dyes discussed in Chapter 2 should not have significant temperature dependence.<sup>14</sup> However, other nonradiative rates, including isomerization which occurs in shorter chain cyanines, are temperature dependent.<sup>73,76</sup> Thus, temperature dependent studies are important for a more complete view of the photophysics of these dyes. Unfortunately, polymethine dyes studied in this thesis are not soluble in standard glass formers such as 2 Me-THF, glycerol,<sup>102</sup> or the sugar matrixes used for cyanine molecular aggregates.<sup>103</sup> This makes it challenging to do temperature dependent studies. After looking at the solubility of dyes in Chapter 2 in less common glass formers, we chose dichloromethane and ethanol in a 1:1 mixture, as previously reported.<sup>104,105</sup>

We first used the model systems of Flav5 and Flav7 in a 0.2 mm cuvette (the standard pathlength for our temperature dependence measurements for other systems) and quickly froze the sample at 77 K in a cryostat. For both Flav5 and Flav7, we noticed a color change that recovered upon return to room temperature (Figure 4.1). The spectral shift in Flav7 resembles previous H-aggregation studies,<sup>26</sup> so we assume that the chromophores H-aggregated during the process of

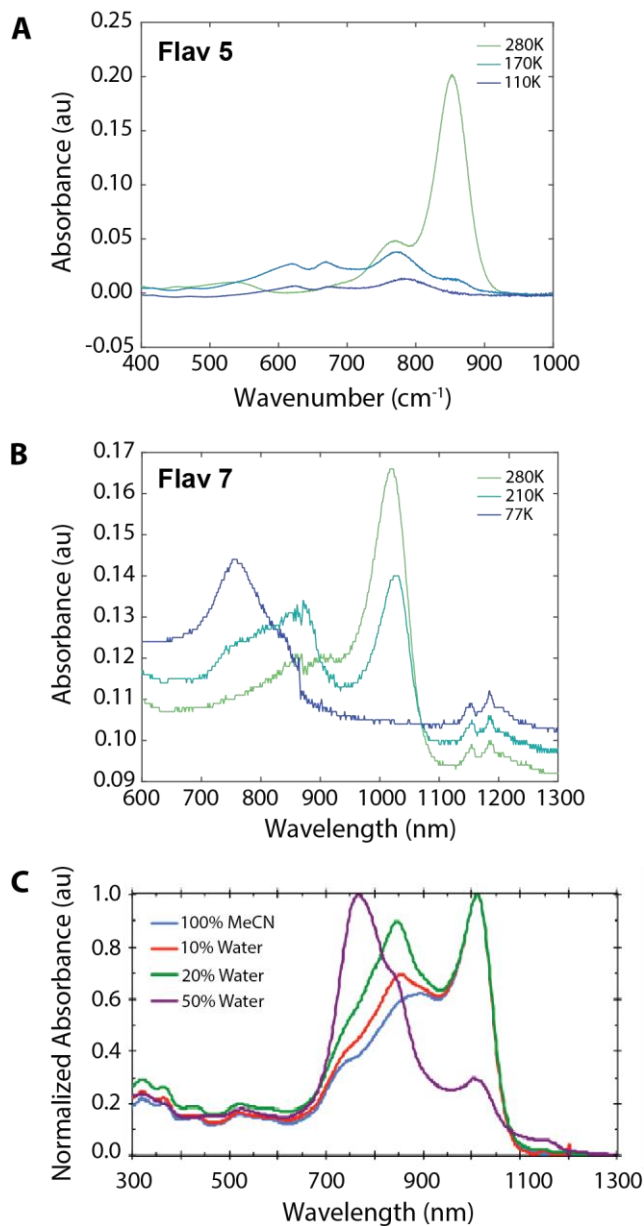


**Figure 4.1. H-aggregation induced by cooling.** Temperature dependent measurements in a 0.02 mm cuvette show spectral changes for Flav5 (a) and Flav7 (b). (c) The change in Flav7 spectra is like H-aggregation in acetonitrile and water, reproduced from Cosco *et al.*<sup>26</sup>

cooling (Figure 4.1). Since the goal is to understand the photophysics of the monomer, we optimized parameters to reduce aggregation.

Based on observations from collaborators that there is less aggregation of the Chrom5 and Chrom7 dyes, we began to include these in our analysis (Figure 4.2). Since one variable for

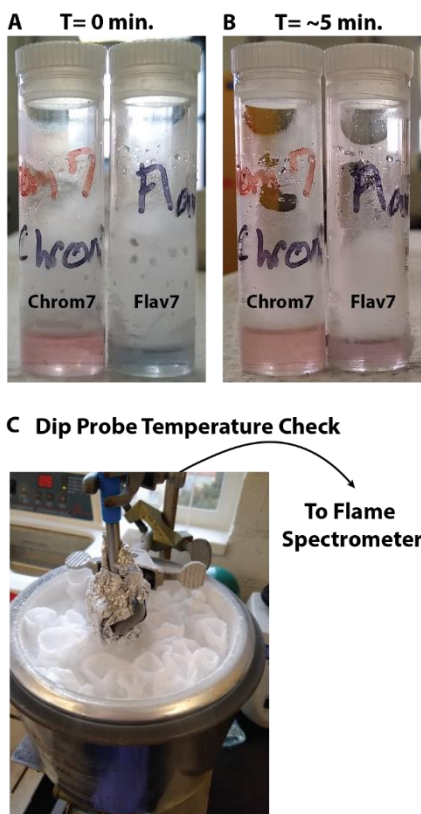


**Figure 4.2. Observation of color change and quick temperature probe set up.** Concentrated Chrom7 and Flav7 after being removed from liquid nitrogen (a) and 5 minutes later (b) shows a greater observation difference with Flav7. (c) Experimental set up of the *in-situ* temperature probe in the chloroform-liquid nitrogen ice bath.

aggregation is concentration, we increased the pathlength of the cuvette to 1 mm and developed a faster method to screen conditions as standard glassy matrix procedures experiments take hours to complete. We used a Vis/NIR/UV-vis *in-situ* probe Ocean Insight, the Flame UV-Vis and NIR spectrometer and a chloroform-liquid nitrogen ice bath to bring the temperature down to 210 K based on the specification of the dip probe (Figure 4.2c). Then the absorption spectra of a solution of a known concentration was measured through the dip probe to observe any reduction in the monomer absorptive features. After finding a concentration where there is no obvious reduction, we measured the temperature dependence absorption measurements of Chrom5 and Chrom7.

For Chrom5 and Chrom7, we observed an absorption peak redshift and a narrowing of the full width half maximum (FWHM) of the first peak with reduction in temperature. The absorption peak's redshift could be a result of changes in reorganization energy with respect to temperature change as well as matrix stabilization. The peak narrowing is indicative of temperature dependent homogenous broadening from the solvent. Future experiments measuring temperature dependent fluorescence and lifetime values would reveal a better molecule understanding of the weak coupling energy gap law.

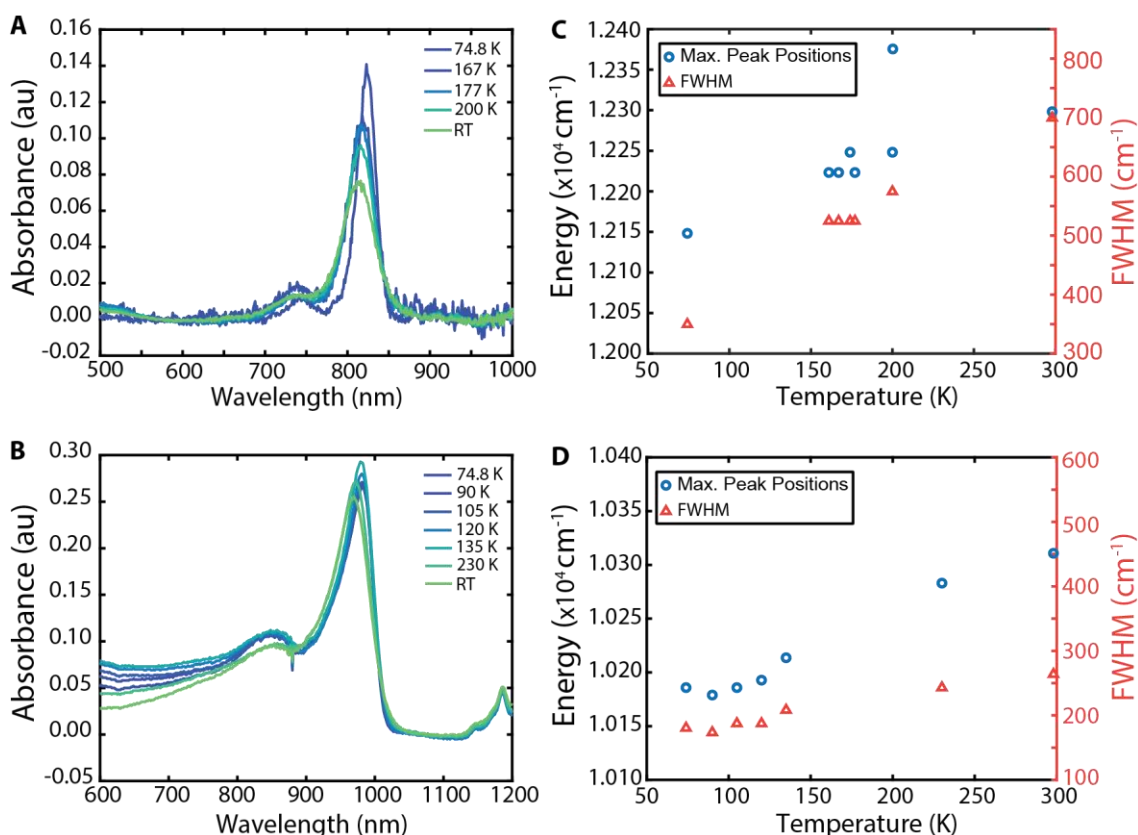


**Figure 4.3. Temperature dependence of Chrom5 and Chrom7.** Absorption spectra for Chrom5 (a) and Chrom7 (b) show a redshift with lower temperatures. (c,d) The peak maximums and the FWHMs of the first peak are plotted with respect to temperature. Chrom5 (c) has a greater change in FWHM than Chrom7 (d).



## 4.2. Heavy Atom Effect

The heavy atom effect is the process by which heavy atoms within molecules or in surrounding molecules induce a greater spin-orbit coupling, allowing for spin forbidden processes like phosphorescence and intersystem crossing to occur.

### 4.2.a. Internal Heavy Atom Effects

One previously shown process to redshift emission of dyes is the inclusion of heavy atoms which can add more electrons into the transition.<sup>26,106</sup> However, heavier atoms, historically metals, allow for spin-orbit mixing which opens spin forbidden processes. If this pathway turns on, it may reduce imaging applications, but retain utility in deeper photodynamic therapy which relies on triplet states to sensitize oxygen.<sup>107,108</sup> To follow up on the energy gap independent parameter analysis between IR-26 and IR-27 from Chapter 2, sulfur substituted Flav7 and Chrom7 were synthesized (Figure 4.4a). Photoluminescence lifetimes were measured following the general method (Section 4.7). All dyes in Table 4.1 with oxygen heteroatoms are both blue shifted and have higher quantum yields than their sulfur heteroatom containing counterparts. When utilizing the energy gap independent parameter,  $\xi$  (Section 2.2d), we saw that addition of oxygen improves quantum yield even beyond the effect of blue shifting the energy gap of the dye, ( $\xi > 0$ , Table 4.1). One reason is the decrease transition dipole moment that was determined from equation 2.3, which is based on the radiative rate. This could be because of a different degeneracy ratio,  $g_2/g_1$ , between the ground and excited state for the sulfur and oxygen substitutions. A higher  $g_2/g_1$  when sulfur is the heteroatom could indicate mixing with a triplet energy state. Additionally, when comparing the nonradiative rates to the nonradiative rate fit from Section 2.2b, we observe a larger gap between the ideal  $k_{nr}$  fit line and the sulfur substituted dyes compared to the oxygen

counterparts (note Figure 4.4c is in log scale). This indicates that there are additional nonradiative rates not included in internal conversion. Together, this indirectly implies that there is more triplet character in the sulfur substituted dyes as sulfur atoms should impart greater spin-orbit coupling onto the molecule. However, other experiments including temperature dependence, transient absorption, computation, and external heavy atom effect would be required to confirm the enhancement of triplet character by sulfur inclusion.

<b>Dye</b>	$E_g$ ( $\text{cm}^{-1}$ )	$E_{ST}$ ( $\text{cm}^{-1}$ )	$\Phi_F$ ( $\times 10^{-2}$ )	$k_{tot}$ ( $\times 10^9 \text{ s}^{-1}$ )	$k_{nr}$ ( $\times 10^9 \text{ s}^{-1}$ )	$\mu_{21}$ ( $\text{D}$ )	$\xi$ ( <b>S to O</b> )
<b>SChrom7</b>	9295	190.0	0.38	17.3	17.2	13.5	0.88
<b>Chrom7</b>	10128	215.4	1.70	6.86	6.74	15.6	
<b>IR – 26</b>	9276	298.7	0.05	49	49	8.4	0.43
<b>IR – 27</b>	10111	240.5	0.35	19.2	19.1	12.3	
<b>SFlav7</b>	8921	175.1	0.10	36.7	36.7	10.8	0.63
<b>Flav7</b>	9603	267.7	0.61	14.7	14.6	15.0	

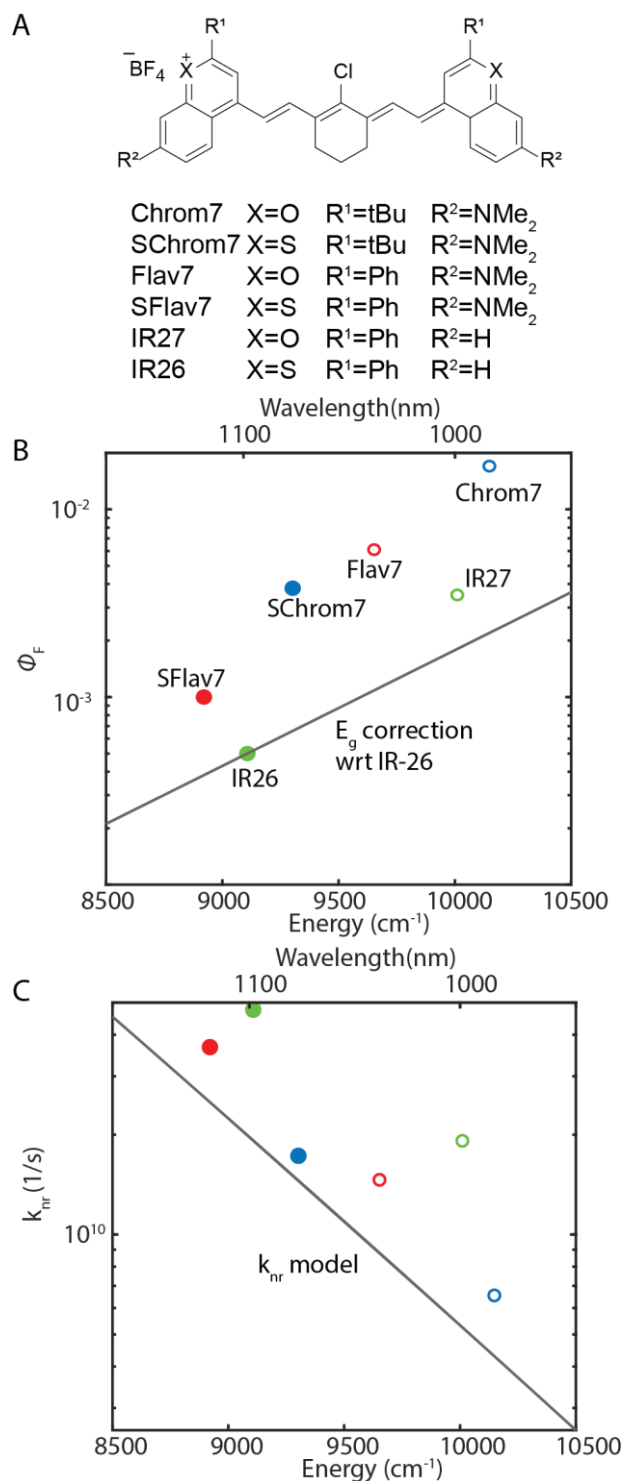


**Figure 4.4. Impact of sulfur as heteroatom in polymethine dyes.** (a) Structure of dyes included in this study. (b) Impact on quantum yield with energy gap using the value of the energy gap comparator for IR 26 to guide the eye. (c) Nonradiative rates with respect to energy gap with the  $k_{nr}$  value derived from Chapter 2.3.

## 4.2.b External Heavy Atom Effect

Like the internal heavy atom effect, the external heavy atom effect is where introduction of a heavy atom in a solvent or a solvent matrix induces intersystem crossing and phosphorescence.<sup>109,110</sup> To study this in the polymethine scaffold, we took lifetimes and quantum yields of Flav5 and Flav7 in different solvents, dichloromethane (DCM), dibromomethane (DBrM), and diiodomethane (DIM). First, both the absorbance and emission spectra redshift with heavier atoms in the solvents (Figure 4.5). This trend could be in part due to the solvent refractive index differences, 1.41, 1.54, and 1.74 in order of increasing molecular weight, but may also

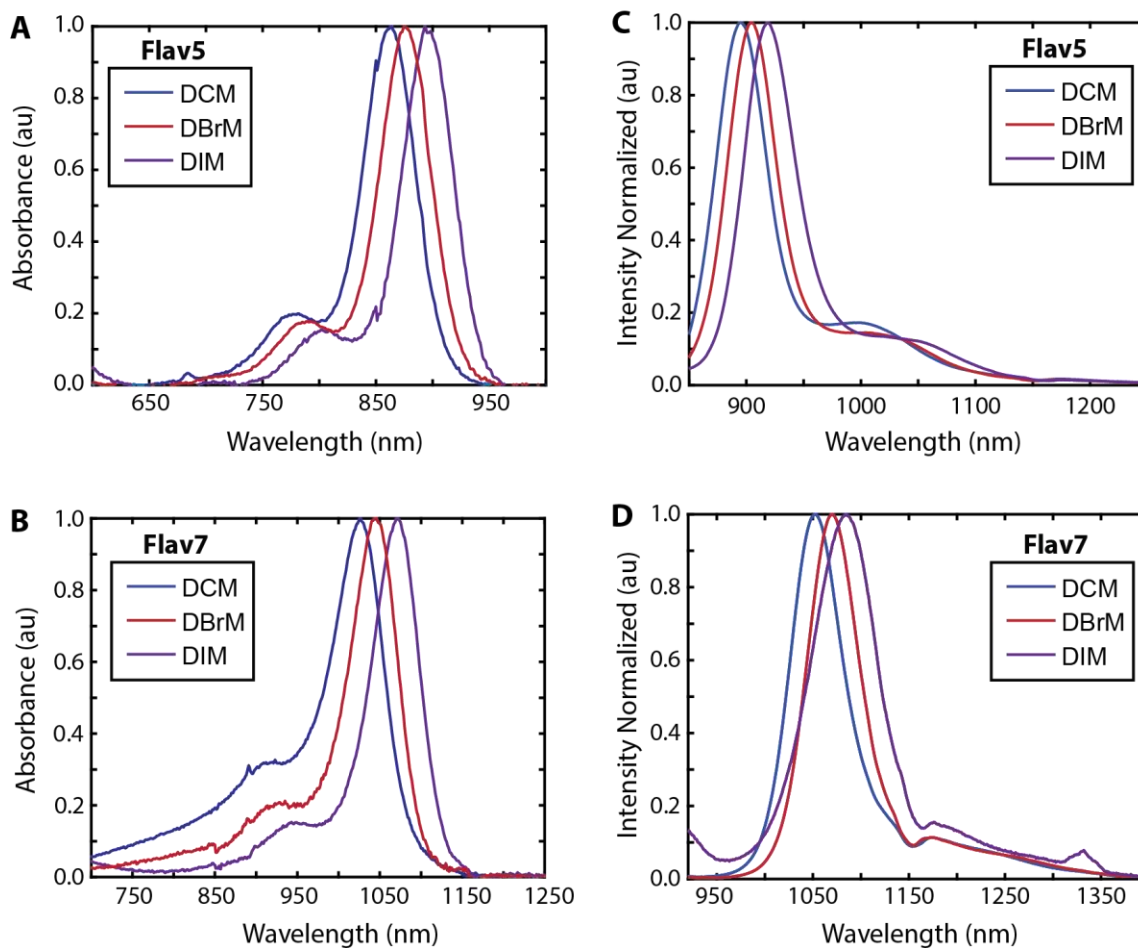


**Figure 4.5. Redshift in absorption and emission with increasingly heavier atom solvent molecule.** Absorption spectra of Flav5 (a) and Flav7 (b) and emission spectra of Flav5 (c) and Flav7 (d) show peaks redshift when changing the solvent from DCM to DBrM to DIM.

indicate that there are nontrivial impacts of the solvent upon the quantum mechanical environment (Figure 4.5).<sup>111,112</sup>

We took relative lifetime and relative quantum yield measurements and observed different trends for Flav5 and Flav7 (Figure 4.6). Total rates and nonradiative rates for Flav7 increased with inclusion of heavier atoms in the solvent which follows energy gap relationships given the slight redshift with heavier atoms but may also be indicative of increased intersystem crossing with external heavy atoms. Unexpectedly the radiative rates and quantum yield in Flav7 and Flav5 is highest in dibromomethane. On the other hand, the total rate and nonradiative rate decrease with redshift in Flav5 which is paradoxical to energy gap laws. Part of this perplexing trend in the quantum yield and radiative rate can be explained by the increase in the refractive index of the solvents which would increase the radiative rate linearly assuming all other values are kept constant. Additionally, the transition dipole moment is not constant across solvents with the transition dipole moment being highest for both Flav7 and Flav5 in DBrM (Table 4.2). These parameters partially counteract the redshift in the energy gap which should lead to a cubic decrease in radiative rates. To explain the perplexing trend in Flav5 for nonradiative rates, we need to look further into steady state indicators of vibrational coupling. For both dyes, the Stokes shift and the

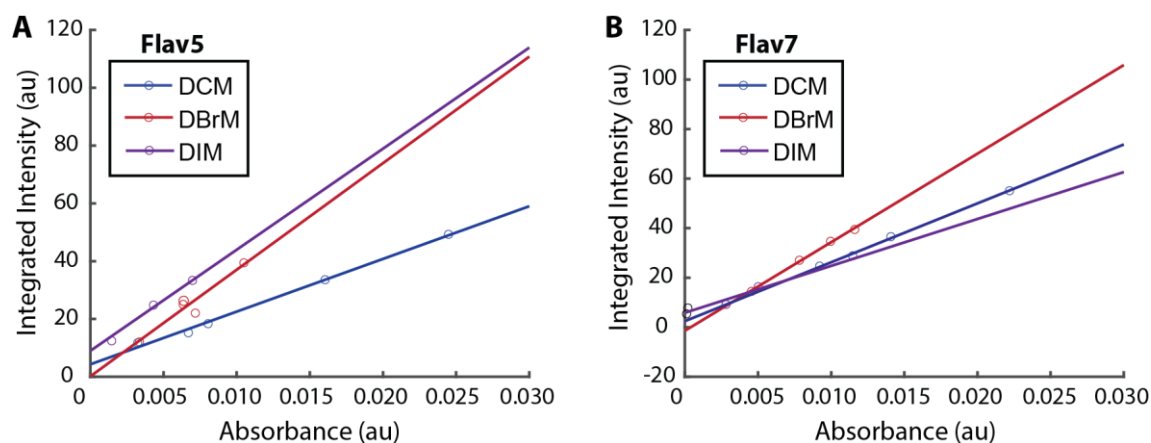


**Figure 4.6. Relative quantum yield for Flav5 (a) and Flav7 (b) in different solvents.**

FWHM of the first transition in fluorescence have no recognizable trend with solvent. However, the absorption FWHM decreases for the heavier atom solvent. Both the total broadening and the amount of mirror symmetry between the absorption and fluorescence impact internal conversion through both adiabatic and nonadiabatic coupling terms which could explain differences in the rate of internal conversion.<sup>113</sup> Alternatively, the solvents could impact other nonradiative rates like the intended intersystem crossing or the unintended isomerization. Note that quantum yield measurements should be replicated over a larger absorption range. Further work should be done to analyze the impact of titration of heavier atom molecules into a standard solvent compared to the current trend of pure solvents, though preferential solubility may be an issue. Additionally, isolation into a glassy matrix would remove many differences in the solvent impact on isomerization with heavier solvent molecules.

<b>Table 4.2. Photophysical Properties of Flav7 and Flav5 in Different Solvents</b>									
<b>Dye</b>	<b>E<sub>g</sub></b> (cm <sup>-1</sup> )	<b>E<sub>ST</sub></b> (cm <sup>-1</sup> )	<b>FWHM<sub>ab</sub></b> (cm <sup>-1</sup> )	<b>FWHM<sub>em</sub></b> (cm <sup>-1</sup> )	<b>Φ<sub>F</sub><sup>*</sup></b> (10 <sup>-2</sup> )	<b>k<sub>tot</sub></b> (10 <sup>9</sup> s <sup>-1</sup> )	<b>k<sub>r</sub></b> (10 <sup>7</sup> s <sup>-1</sup> )	<b>k<sub>nr</sub></b> (10 <sup>9</sup> s <sup>-1</sup> )	<b>μ<sub>21</sub></b> (D)
<b>Flav7</b>									
DCM	9603	267.7	761	585	0.61	14.1 ± 0.2	8.59	14.0	14
DBrM	9466	206.1	647	549	0.9	14.5 ± 0.2	13.0	14.4	18
DIM	9281	129.1	597	693	0.5	15.4 ± 0.2	7.69	15.4	13
<b>Flav5</b>									
DCM	11468	276.9	742	648	6.1	3.01 ± 0.01	18.4	2.83	16
DBrM	11258	353.5	692	622	12.4	2.14 ± 0.01	26.5	1.87	20
DIM	11034	268.7	435	637	11.7	1.80 ± 0.01	21.0	1.59	17

### 4.3. Silicon-Rosindolizine Fluorophores

This section is partially adapted from sections of Meader, W.E., Lin, E.Y., Lim, I., Friedman, H.C., Ndaleh D., Shaik, A.K., Hammer, N.I., Yang, B., Caram, J.R., Sletten, E.M., Delcamp, J.H. “Shortwave Infrared Absorbing and Emitting Silicon-Rosindolizine Fluorophores for *in vivo* Fluorescence Imaging” in preparation. There will be a quick introduction to the molecular system followed by the analysis relevant to my contribution to the manuscript.

Lead by William Meader of the Laboratory of Dr. Jared Delcamp, several novel silicon-rosindolizine (SiRos) fluorophores, a type of xanthene structure, were synthesized and found to have peak emission wavelengths between 1300 and 1700 nm. Akin to the trend of redshift caused by the change from oxygen to sulfur in chromenylium polymethine dyes, the replacement of oxygen with silicon on xanthene dyes also results in a redshift.<sup>114</sup> The research used the silicon replacement approach to redshift the absorption and emission of previously synthesized NIR xanthene dyes.<sup>115,116</sup>

Photoluminescent lifetimes were measured to understand the photophysical characteristics and excited state kinetics of the SiRos dyes (Table 4.3). Upon excitation with a 785 nm laser, emitted photons were detected and timed using superconducting nanowire single photon detectors (SNSPDs, see Section 4.7 for experimental details). Interestingly, the lifetimes were observed to be inversely proportional to the emission energy of the fluorophores, with SiRos1300 having the shortest deconvolved lifetime of 20 ps, and SiRos1700 having the longest lifetime of 47 ps. This is counter intuitive to the energy gap laws (Chapter 2).<sup>14,93</sup> As there was no trend in Stokes shift ( $E_{\text{Stokes}}$ ) for the SiRos dyes, this trend in lifetimes cannot be explained by changes in coupling to vibrational modes between chromophores. Additionally, solvent reabsorption is known to decrease lifetimes due to direct energy transfer from chromophore to solvent vibrational

modes.<sup>77,79</sup> Note there is a large overtone transition in the solvent dichloromethane around 1600 nm; thus, the lengthening of lifetimes at longer wavelengths is even more surprising given these mitigating factors.

Combining quantum yield, lifetime, and absorption spectrum information, we observed that the radiative rates decrease from SiRos1300 to SiRos1700 ( $2.8 \times 10^6 \text{s}^{-1}$  and  $2.34 \times 10^5 \text{s}^{-1}$  respectively) while nonradiative rates only slightly decrease ( $5 \times 10^{10}$  and  $2.13 \times 10^{10}$ ). Therefore, the change in quantum yields is almost entirely attributable to changes in radiative rates. Indeed, the measured transition dipole moment decreases from 3.3 to 1.4 D as the chromophore's emission peak redshifts. We then estimate the oscillator strength of absorption ( $f_{12}$ ), by integrating the absorption cross section, consistent with a single electronic state contributing to the absorption spectrum (eq. 2.38). However, the oscillator strength of emission (eq. 2.35) is substantially diminished, suggesting a large number of "darker" emissive states contribute to the observed photophysics.<sup>117</sup> An estimate of this is given by degeneracy ratio ( $\frac{g_2}{g_1} = -\frac{f_{12}}{f_{21}}$ ) of  $S_1$  states to  $S_0$  states which goes as high as 270 for SiRos1700. This is a dramatic increase compared to the typical  $g_2/g_1$  of 1 to 3 observed for polymethine dyes.<sup>38-40,93</sup> This strongly suggests potential mixing of singlet and triplet excited states as the  $S_1 - S_0$  gap closes, though the degeneracy ratio cannot be taken as a precise estimate of the number of electronic configurations near the bandgap. Increase in triplet and singlet mixing could lengthen the fluorescent lifetimes and, perhaps, protect the excited state from direct internal conversion to the ground state. Increasing  $n \rightarrow \pi^*$  character in SiRos1700 could also account for increasing lifetimes, diminished transition dipole moment, and stronger coupling to triplet states as is suggested by the lifetime data.



	$E_g$ ( $cm^{-1}$ )	$E_{Stokes}$ ( $cm^{-1}$ )	$\tau_F$ ( $ps$ )	$f_{12}$	$f_{21}$	$\mu_{21}$ ( $D$ )	$g_2/g_1$
<b>SiRos1300</b>	8232	1080	20	1.14	-0.028	3.3	41
<b>SiRos1550</b>	6921	996	26	1.15	-0.014	2.5	84
<b>SiRos1700</b>	6419	1052	47	1.07	-0.004	1.4	270

#### 4.4. Deuteration of Additional Polymethine Scaffolds

To further study the effect of deuteration on polymethine scaffolds, we received non-bridged polymethine dyes synthesized by Hana Janeková from the laboratory of Dr. Peter Štacko (Figure 4.7). For all but dye 2, the quantum yields increased, and the Stokes shift decreased with deuteration indicative that we deuterated the most coupled C-H vibrational modes (Table 4.4). These dyes also show a decrease in nonradiative rate and total rate with respect to the deuterated derivatives similar to dyes previously discussed in Chapter 2 and 3. Interestingly for dye 4, the radiative rate increased with deuteration beyond the error in the lifetime analysis. This indicates that the introduction of deuterium may impact the electron density of the scaffold and not just the vibronic environment. However, synthesis of more dyes would be needed to determine if there is a trend. Dye 4 is a nonbridged chlorine free version of Flav7 that is blueshifted by  $296\text{ cm}^{-1}$  and the energy gap independent parameter,  $\xi$ , by comparing Flav7 to dye 4 is 0.5 demonstrating that it has increased quantum yield compared to Flav7 independent of the blueshift in emission (Section 2.2d). Further steps to study this phenomenon would require synthesis of dye 4 with the chlorine in the central part of the methine bridge and Flav7 without the chlorine unit. These two structures would help elucidate if the energy gap shift and the quantum yield differences are predominately from the chlorine addition or the cyclohexane ring addition. We would predict that chlorine has

the greater impact on the quantum yield and the energy gap shift like previously discussed heavier atom trends (Section 4.2a).<sup>7</sup>

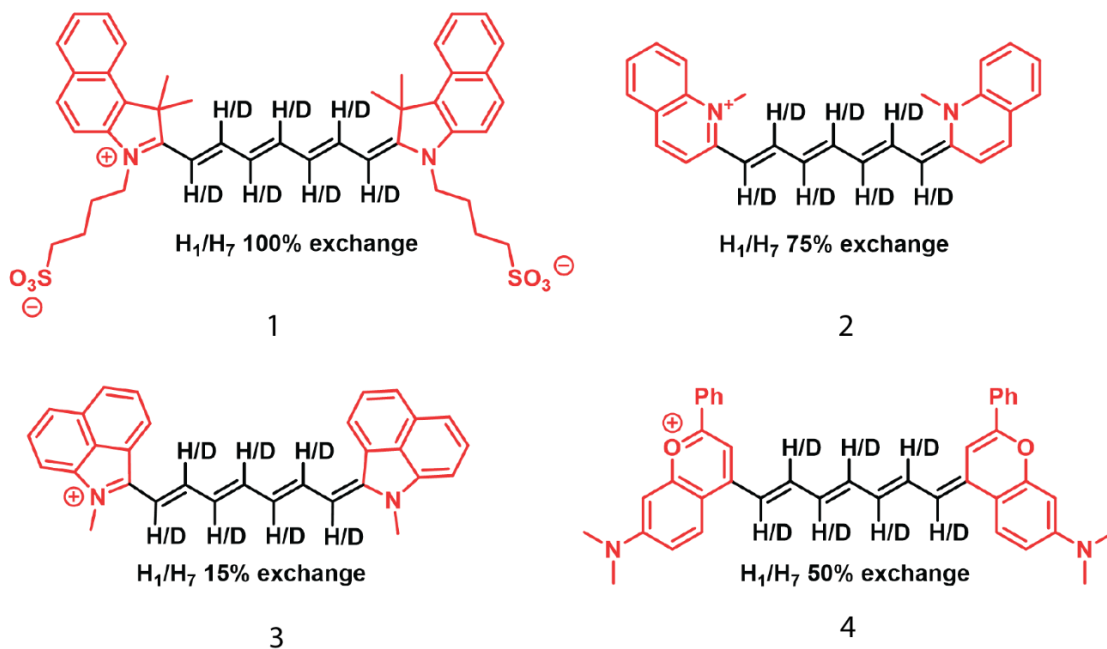


Figure 4.7. Structure of linear 7 chain polymethine dyes 1-4.

Dye	$E_g$ ( $\text{cm}^{-1}$ )	$E_{ST}$ ( $\text{cm}^{-1}$ )	$\epsilon_{\text{max}}$	$\phi_F$ ( $\times 10^{-2}$ )
1H	12353	610	225960 <sup>a</sup>	9.56
1D	12247	570	169730 <sup>a</sup>	10.9
2H	11824	391	224290 <sup>b</sup>	0.055
2D	11838	420	237990 <sup>b</sup>	0.045
3H	9997	270	236920 <sup>b</sup>	0.33
3D	10017	251	219860 <sup>b</sup>	0.36
4H	9899	362	280750 <sup>b</sup>	1.33
4D	9943	316	266580 <sup>b</sup>	1.56

<sup>a</sup> MeOH with 4% DMSO (abs max in bracket) <sup>b</sup>DCM with 4% DMSO

<i>Dye</i>	$k_{tot} (\times 10^9 s^{-1})$	$k_r (\times 10^6 s^{-1})$	$k_{nr} (\times 10^9 s^{-1})$
1H	$2.04 \pm 0.01$	$195 \pm 1.00$	$1.84 \pm 0.01$
1D	$1.80 \pm 0.01$	$197 \pm 1.00$	$1.61 \pm 0.01$
2H	$12.0 \pm 0.10$	$6.58 \pm 0.04$	$12.0 \pm 0.10$
2D	$11.6 \pm 0.10$	$5.20 \pm 0.04$	$11.6 \pm 0.10$
3H	$20.6 \pm 0.40$	$67 \pm 1.00$	$20.5 \pm 0.40$
3D	$18.9 \pm 0.40$	$68 \pm 1.00$	$18.9 \pm 0.40$
4H	$8.41 \pm 0.07$	$112 \pm 1.00$	$8.29 \pm 0.07$
4D	$8.24 \pm 0.07$	$129 \pm 1.00$	$8.11 \pm 0.07$

## 4.5. General Lifetime Methods

The standard procedure for all the lifetime measurements above is as follows: We recorded PL lifetimes using a home-built, all-reflective epifluorescence setup.<sup>37</sup> For all dyes below we used a pulsed 785 nm excitation. Emission was then collected and filtered with a 90:10 beamsplitter and appropriate excitation filters finally reflectively coupled into a single-mode fiber (F-SMF-28-C-10FC, Newport) and detected using an SNSPD (Quantum Opus One).<sup>35,37,80</sup>

Given the short lifetimes of these dyes, lifetimes were fit with a convolution of the instrument response function and an exponential. To determine the lifetime (or decay rate,  $k$ ) for each TCSPC trace we fit each curve to a convolution of the sum of two Gaussians with a single exponential decay:

$$\begin{aligned}
I(t) = & \frac{I_0}{2} e^{-k\left(\frac{t-t_0-\sigma_1^2 k}{2}\right)} \left(1 + \operatorname{erf}\left(\frac{(t-t_0)-\sigma_2^2 k}{\sqrt{2}\sigma}\right)\right) \\
& + \frac{aI_0}{2} e^{-k\left(\frac{t-t_0-t_1-\sigma_2^2 k}{2}\right)} \left(1 \right. \\
& \left. + \operatorname{erf}\left(\frac{(t-t_0-t_1)-\sigma_2^2 k}{\sqrt{2}\sigma_2}\right)\right)
\end{aligned} \tag{Eq. 4.1}$$

The width,  $\sigma_1$  and  $\sigma_2$ , of each Gaussian, the time offset,  $t_1$ , between the two Gaussians and amplitude scale,  $a$ , were determined using the instrument response function (IRF) which was measured as the backscatter off of a cuvette with solvent (e.g., DCM) without the longpass filters (Table 4.6). The initial peak amplitude,  $I_0$ , the rate,  $k$ , and  $t_0$  were free fitting parameters, while the time offset,  $t_1$ , and the IRF widths,  $\sigma_1$  and  $\sigma_2$  were fixed variables. We use a conservative error of 1 ps (the instrument resolution) for our lifetimes.

<b>Table 4.6. Instrument Response Function Fit Parameters</b>		
	<b>IRF fit values for 4.2a</b>	<b>IRF fit values for 4.2b, 4.3, 4.5</b>
<b><math>\sigma_1</math>(ps)</b>	32.0	40.7
<b><math>\sigma_2</math>(ps)</b>	50.6	66.6
<b><math>t_1</math>(ps)</b>	6.6	82.7
<b><math>a</math></b>	1.6	0.25

## 4.6 Future Directions

In the beginning of this chapter, we developed an approach to measure temperature dependence absorption that can be used to measure time resolved emission in polymethine dyes. Temperature dependent absorption measurements of chromenylium polymethine dyes showed redshift and linewidth narrowing in absorption upon cooling. Temperature dependence of time-resolved and steady state emission measurements will illustrate the impact of both immobilization

and temperature on the parameters for energy gap dependence, giving more insight into the fundamental photophysics of the polymethine dyes. Understanding of the external heavy atom effect for polymethine dyes requires further study. The changes in spectral shifts and narrowing shown in section 4.2b demonstrate that there are other variables beyond the heavy atoms inherent to the solvents that need to be addressed. Solvent studies including glassy matrices, viscosity dependence, and solvent mixtures of heavy and nonheavy atoms will help isolate important variables. Work on the internal heavy atom effect shows a decrease in transition dipole moment for all polymethine dyes studied. Going forward, putting the oxygen to sulfur change in heteroatom in the chromenylum polymethine dyes into greater conversation with the rosindolizine and silicon rosindolizine dyes may increase general understanding of the impact of heavy atoms on the heteroatoms in organic chromophores. To this end, time resolved lifetimes for more rosindolizine and silicon rosindolizine derivatives would allow for a more complete energy gap law analysis, as was done in Chapter 2 for this scaffold. Deuteration of other cyanine dyes and a linearized version of Flav7 shows that deuteration's positive effect on quantum yield is not absolute. The difference in quantum yield and energy gap for linearized Flav7 and the original Flav7 reveals opportunities to study non-deuterium-based substitution on the polymethine bridge. All these vignettes demonstrate future pathways to expand the understanding of NIR/SWIR fluorophore photophysics.

## Chapter 5

### Outlook on Photophysics in the SWIR

In the field of SWIR photophysics, there are opportunities through synthesis and photophysical experimentation to improve our understanding of chromophore design. This thesis has predominately focused on polymethine dyes, but there are many other promising SWIR emitting dye classes to be studied, of which I will briefly only discuss a few. For example, xanthene dyes have many synthetic pathways for redshifting their emission, including extending conjugation and heteroatom substitution (Figure 5.1a).<sup>116,118,119</sup> Another class of dyes are donor-acceptor-donor SWIR chromophores that have much larger Stokes shifts than polymethine counterparts and may have different molecular considerations toward photophysical improvement (Figure 5.1b).<sup>72,90,120,121</sup> Both of these scaffolds and others could benefit from application of the combined energy gap law as presented in Chapter 2.

Supramolecular structures are another approach to changing the photophysics of known dyes. Within the polymethine scaffold, one problem is the breakdown of the cyanine limit (where the “particle in a box” model is most applicable) with longer polymethine chains, reducing the transition dipole moment of the dye.<sup>94</sup> One solution is encapsulating longer chain polymethine dyes in a molecular container, which stabilizes the cyanine limit (Figure 5.1c).<sup>122</sup> Another known route toward redshifting the emission is J-aggregation, where several dyes are transition dipole moment coupled. J-aggregates have increased transition dipole moments and reduced the Stokes shifts compared to monomeric dyes making them promising approach toward SWIR imaging systems.<sup>55,56,63,123</sup>

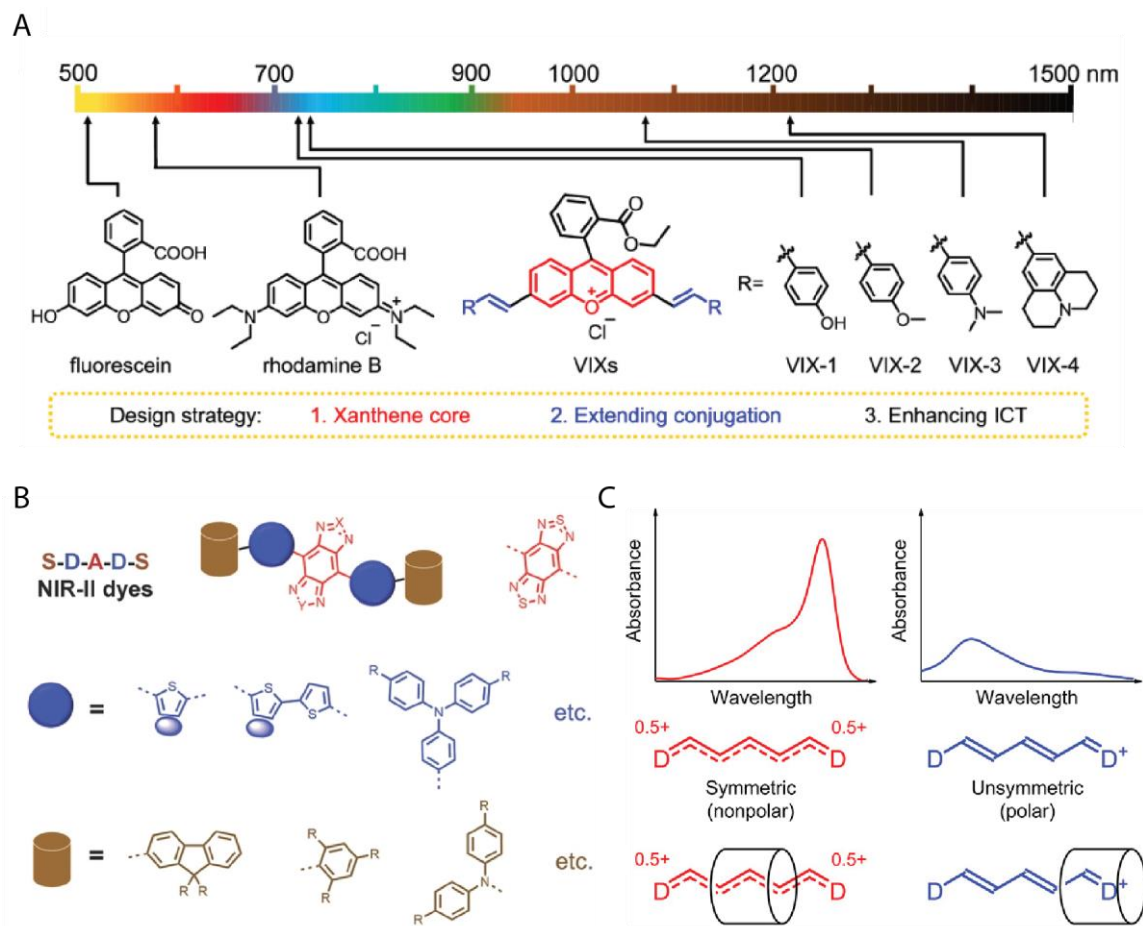


**Figure 5.1. Synthetic approaches toward better SWIR chromophores.** Options include exploring new scaffolds including xanthenes (a) reproduced from Liu *et al.*<sup>118</sup> and DAD dyes (b) reproduced from Zhu *et al.*<sup>121</sup> which show many options for synthetic modification within the scaffold. (c) Supramolecular stabilization of the symmetric nonpolar cyanine limit in polymethine dye improves absorption parameters, reproduced from Li *et al.*<sup>122</sup>.

The combined energy gap law discussed through this thesis has predictive power over the general trends in the SWIR. However, quantum yields are limited by a dye's most detrimental pathway, most often the highest nonradiative rate. In the SWIR, the highest nonradiative rate is predicted to be internal conversion from C-H vibrational stretches. With certain synthetic changes, like deuterating or halogenating privileged C-H stretches, internal conversion may not be the most deleterious rate. Therefore, future directions include the study of other nonradiative rates and the predominance of C-H vibrational stretches for internal conversion. A few of the other nonradiative rates are photoisomerization, vibrational energy transfer, and intersystem crossing. Careful

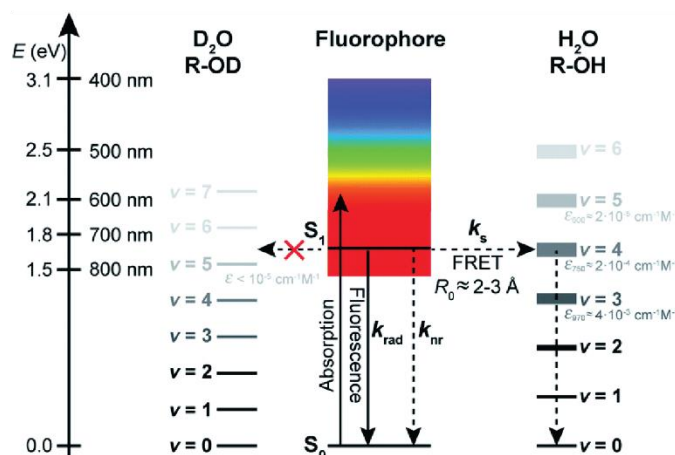
rigidification or temperature dependence can isolate the effect of photoisomerization which previously showed the greatest effect in dyes in the visible spectra.<sup>39,76</sup> Solvent deuterations of both protic and aprotic solvents can probe vibrational FRET (Figure 5.2a).<sup>77-79</sup> Vibrational FRET becomes a critical nonradiative pathway in the SWIR, since solvent vibrational overtone bands become stronger. For example, the molar absorptivity of OH stretches increases from approximately  $2 \times 10^{-4} \text{ cm}^{-1}\text{M}^{-1}$  at 750 nm to  $4 \times 10^{-3} \text{ cm}^{-1}\text{M}^{-1}$  at 970 nm while the OD stretch has negligible absorption in the region ( $< 10^{-5} \text{ cm}^{-1}\text{M}^{-1}$ ) (Figure 5.2a).<sup>77</sup> In Section 2.5h, we observed that deuteration of the O-H stretch in ethanol, increased the lifetime of IR-1061 from  $14 \pm 1$  to  $25 \pm 1$  ps. Additional studies in solvents which better stabilize polymethine dyes will illuminate the effect of overtone stretches from organic molecules like DCM in the SWIR. Understanding the contribution of noninternal conversion nonradiative pathways will improve molecular and solvent system design.

The photophysics behind internal conversion is predicated on understanding the coupling of vibrational modes to the electronic transition. Throughout this dissertation, I have made assumptions based on molecular structure and steady state and time-resolved measurements to parameterize the values of coupling of higher energy vibrational modes. Complicating these assumptions, there are dyes that absorb and emit in the visible spectrum that couple more strongly to lower energy modes.<sup>124</sup> . Therefore, use of techniques like resonance Raman or more recently terahertz femtosecond coherence spectra (Figure 5.2b) can evaluate the coupling associated with each vibrational stretch for organic chromophores.<sup>100,101,125</sup> For dyes with strong coupling from lower energy stretches computational models taking into account the interplay between higher vibrational and lower vibrational modes may be required to fully understand the photophysics



underlying internal conversion.<sup>112</sup> Incorporation of these newer models and experimental parameters will refine our understanding of the fundamental photophysics in SWIR chromophores.

A Vibrational FRET



B Femtosecond coherence spectra for coupling of vibrational modes

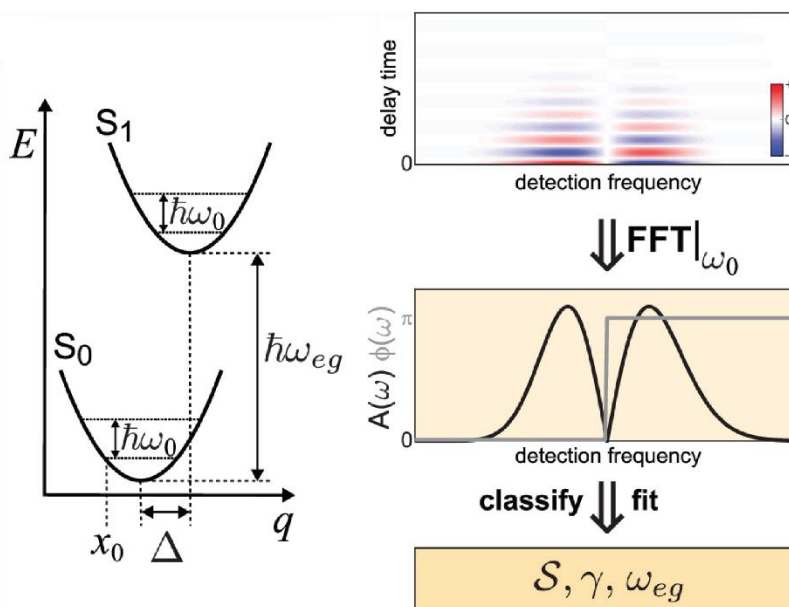


**Figure 5.2. Examples of photophysical experiments to test assumptions associated with energy gap law for nonradiative rates.** (a) FRET to vibrational modes is an additional nonradiative rate which reduced with deuteration. Figure was reproduced from Maillard *et al.*<sup>77</sup> (b) Femtosecond coherence spectroscopy can probe the coupling of each vibrational mode of a molecule. On the left is a diagram of the displaced harmonic oscillator model. On the right, measured vibrational quantum beat signals are Fourier transformed into femtosecond coherence spectra. These spectra can be fit to classify, the Huang-Rhys factor,  $S = \frac{1}{2} \left( \frac{\Delta}{x_0} \right)^2$ , energy gap in frequency  $\omega_{eg}$ , and electronic dephasing,  $\gamma$ . Reproduced from Barclay *et al.*<sup>101</sup>

## References

- (1) Bruns, O. T.; Bischof, T. S.; Harris, D. K.; Franke, D.; Shi, Y.; Riedemann, L.; Bartelt, A.; Jaworski, F. B.; Carr, J. A.; Rowlands, C. J.; et al. Next-Generation in Vivo Optical Imaging with Short-Wave Infrared Quantum Dots. *Nat. Biomed. Eng.* **2017**, *1* (4), 0056.
- (2) Carr, J. A.; Valdez, T. A.; Bruns, O. T.; Bawendi, M. G. Using the Shortwave Infrared to Image Middle Ear Pathologies. *Proc. Natl. Acad. Sci. U. S. A.* **2016**, *113* (36), 9989–9994.
- (3) Carr, J. A.; Aellen, M.; Franke, D.; So, P. T. C.; Bruns, O. T.; Bawendi, M. G. Absorption by Water Increases Fluorescence Image Contrast of Biological Tissue in the Shortwave Infrared. *Proc. Natl. Acad. Sci. U. S. A.* **2018**, *115* (37), 9080–9085.
- (4) Kutila, M.; Pyykonen, P.; Holzhuter, H.; Colomb, M.; Duthon, P. Automotive LiDAR Performance Verification in Fog and Rain. In *IEEE Conference on Intelligent Transportation Systems, Proceedings, ITSC*; Institute of Electrical and Electronics Engineers Inc., 2018; Vol. 2018-November, pp 1695–1701.
- (5) Photonics Products: Imaging for Surveillance and Security: SWIR cameras cut through haze for surveillance and security | Laser Focus World  
<https://www.laserfocusworld.com/detectors-imaging/article/16556355/photonics-products-imaging-for-surveillance-and-security-swir-cameras-cut-through-haze-for-surveillance-and-security> (accessed Nov 19, 2022).
- (6) Tenney, S. M.; Vilchez, V.; Sonnleitner, M. L.; Huang, C.; Friedman, H. C.; Shin, A. J.; Atallah, T. L.; Deshmukh, A. P.; Ithurria, S.; Caram, J. R. Mercury Chalcogenide Nanoplatelet-Quantum Dot Heterostructures as a New Class of Continuously Tunable

- Bright Shortwave Infrared Emitters. *J. Phys. Chem. Lett.* **2020**, *11* (9), 3473–3480.
- (7) Mayerhöffer, U.; Gsänger, M.; Stolte, M.; Fimmel, B.; Würthner, F. Corrigendum: Synthesis and Molecular Properties of Acceptor-Substituted Squaraine Dyes. *Chem. – A Eur. J.* **2021**, *27* (71), 17970–17971.
- (8) Kuhn, H. A Quantum-Mechanical Theory of Light Absorption of Organic Dyes and Similar Compounds. *J. Chem. Phys.* **1949**, *17* (12), 1198–1212.
- (9) Dirac, P. A. M. The Quantum Theory of the Emission and Absorption of Radiation. *Proc. R. Soc. London. Ser. A, Contain. Pap. a Math. Phys. Character* **1927**, *114* (767), 243–265.
- (10) Einstein, A. Zur Quantentheorie Der Strahlung. *Phys. Zeitschrift* **1917**, *18* (121).
- (11) Hilborn, R. C. Einstein Coefficients, Cross Sections, f Values, Dipole Moments, and All That. *Am. J. Phys.* **1982**, *50* (11), 982–986.
- (12) Planck, M. Zur Theorie Des Gesetzes Der Energieverteilung Im Normalspectrum. *Verhandlungen der Dtsch. Phys. Gesellschaft* **1900**, *2*, 237–245.
- (13) Strickler, S. J.; Berg, R. A. Relationship between Absorption Intensity and Fluorescence Lifetime of Molecules. *J. Chem. Phys.* **1962**, *37* (4), 814–822.
- (14) Englman, R.; Jortner, J. The Energy Gap Law for Radiationless Transitions in Large Molecules. *Mol. Phys.* **1970**, *18* (2), 145–164.
- (15) Poh, Y. R.; Pannir-Sivajothi, S.; Yuen-Zhou, J. Understanding the Energy Gap Law under Vibrational Strong Coupling. **2022**.

- (16) Kwak, K.; Thanthirige, V. D.; Pyo, K.; Lee, D.; Ramakrishna, G. Energy Gap Law for Exciton Dynamics in Gold Cluster Molecules. *J. Phys. Chem. Lett.* **2017**, *8* (19), 4898–4905.
- (17) Caspar, J. V.; Meyer, T. J. Application of the Energy Gap Law to Nonradiative, Excited-State Decay. *J. Phys. Chem.* **1983**, *87* (6), 952–957.
- (18) Kober, E. M.; Caspar, J. V.; Lumpkin, R. S.; Meyer, T. J. Application of the Energy Gap Law to Excited-State Decay of Osmium(II)-Polypyridine Complexes: Calculation of Relative Nonradiative Decay Rates from Emission Spectral Profiles. *J. Phys. Chem.* **1986**, *90* (16), 3722–3734.
- (19) Maciejewski, A.; Safarzadeh-Amiri, A.; Verrall, R. E.; Steer, R. P. Radiationless Decay of the Second Excited Singlet States of Aromatic Thiones: Experimental Verification of the Energy Gap Law. *Chem. Phys.* **1984**, *87* (2), 295–303.
- (20) Wilson, J. S.; Chawdhury, N.; Al-Mandhary, M. R. A.; Younus, M.; Khan, M. S.; Raithby, P. R.; Köhler, A.; Friend, R. H. The Energy Gap Law for Triplet States in Pt-Containing Conjugated Polymers and Monomers. *J. Am. Chem. Soc.* **2001**, *123* (38), 9412–9417.
- (21) Birks, J. B.; Hamilton, T. D. S.; Najbar, J. Deuteration Effects on the Phosphorescence of Aromatic Hydrocarbons. *Chem. Phys. Lett.* **1976**.
- (22) Abe, T.; Miyazawa, A.; Konno, H.; Kawanishi, Y. Deuteration Isotope Effect on Nonradiative Transition of Fac-Tris (2-Phenylpyridinato) Iridium (III) Complexes. *Chem. Phys. Lett.* **2010**, *491* (4–6), 199–202.

- (23) Guttman, C.; Rice, S. A. Fluorescence Lifetimes of Individual Vibronic Levels of Partially Deuterated Benzenes: A Further Test of the Theory of Radiationless Processes. *J. Chem. Phys.* **1974**, *61* (2), 651–660.
- (24) Hong, G.; Antaris, A. L.; Dai, H. Near-Infrared Fluorophores for Biomedical Imaging. *Nat. Biomed. Eng.* **2017**, *1* (1), 0010.
- (25) Lautenschläger, G.; Gessner, R.; Gockel, W.; Haas, C.; Schweickert, G.; Bursch, S.; Welsch, M.; Sontag, H. Sentinel-2: Next Generation Satellites for Optical Land Observation from Space. In *Sensors, Systems, and Next-Generation Satellites XVII*; Meynart, R., Neeck, S. P., Shimoda, H., Eds.; 2013; Vol. 8889, p 88890L.
- (26) Cosco, E. D.; Caram, J. R.; Bruns, O. T.; Franke, D.; Day, R. A.; Farr, E. P.; Bawendi, M. G.; Sletten, E. M. Flavylum Polymethine Fluorophores for Near- and Shortwave Infrared Imaging. *Angew. Chemie Int. Ed.* **2017**, *56* (42), 13126–13129.
- (27) Carr, J. A.; Franke, D.; Caram, J. R.; Perkinson, C. F.; Saif, M.; Askoxylakis, V.; Datta, M.; Fukumura, D.; Jain, R. K.; Bawendi, M. G.; et al. Shortwave Infrared Fluorescence Imaging with the Clinically Approved Near-Infrared Dye Indocyanine Green. *Proc. Natl. Acad. Sci.* **2018**, *115* (17), 4465–4470.
- (28) Wan, H.; Du, H.; Wang, F.; Dai, H. Molecular Imaging in the Second Near-Infrared Window. *Adv. Funct. Mater.* **2019**, *29* (25), 1900566.
- (29) Semonin, O. E.; Johnson, J. C.; Luther, J. M.; Midgett, A. G.; Nozik, A. J.; Beard, M. C. Absolute Photoluminescence Quantum Yields of IR-26 Dye, PbS, and PbSe Quantum Dots. *J. Phys. Chem. Lett.* **2010**, *1* (16), 2445–2450.

- (30) Hatami, S.; Würth, C.; Kaiser, M.; Leubner, S.; Gabriel, S.; Bahrig, L.; Lesnyak, V.; Pauli, J.; Gaponik, N.; Eychmüller, A.; et al. Absolute Photoluminescence Quantum Yields of IR26 and IR-Emissive Cd<sub>1</sub>-XHg<sub>x</sub>Te and PbS Quantum Dots-Method- and Material-Inherent Challenges. *Nanoscale* **2015**, *7* (1), 133–143.
- (31) Hu, J. Y.; Ning, Y.; Meng, Y. S.; Zhang, J.; Wu, Z. Y.; Gao, S.; Zhang, J. L. Highly Near-IR Emissive Ytterbium(III) Complexes with Unprecedented Quantum Yields. *Chem. Sci.* **2017**, *8* (4), 2702–2709.
- (32) Li, B.; Zhao, M.; Feng, L.; Dou, C.; Ding, S.; Zhou, G.; Lu, L.; Zhang, H.; Chen, F.; Li, X.; et al. Organic NIR-II Molecule with Long Blood Half-Life for in Vivo Dynamic Vascular Imaging. *Nat. Commun.* **2020**, *11* (1), 3102.
- (33) Ding, B.; Xiao, Y.; Zhou, H.; Zhang, X.; Qu, C.; Xu, F.; Deng, Z.; Cheng, Z.; Hong, X. Polymethine Thiopyrylium Fluorophores with Absorption beyond 1000 Nm for Biological Imaging in the Second Near-Infrared Subwindow. *J. Med. Chem.* *62* (4), 2049–2059.
- (34) Cosco, E. D.; Spearman, A. L.; Ramakrishnan, S.; Lingg, J. G. P.; Saccomano, M.; Pengshung, M.; Arús, B. A.; Wong, K. C. Y.; Glasl, S.; Ntziachristos, V.; et al. Shortwave Infrared Polymethine Fluorophores Matched to Excitation Lasers Enable Non-Invasive, Multicolour in Vivo Imaging in Real Time. *Nat. Chem.* **2020**, *12* (12), 1123–1130.
- (35) Cosco, E. D.; Arús, B. A.; Spearman, A. L.; Atallah, T. L.; Lim, I.; Leland, O. S.; Caram, J. R.; Bischof, T. S.; Bruns, O. T.; Sletten, E. M. Bright Chromenyl Polymethine Dyes Enable Fast, Four-Color in Vivo Imaging with Shortwave Infrared Detection. *J. Am. Chem. Soc.* **2021**, *143* (18), 6836–6846.

- (36) Mattioli, F.; Zhou, Z.; Gaggero, A.; Tanner, M. G.; San, L.; Alvarez, E.; Jiang, W.; Subashchandran, S.; Okamoto, R.; Zhang, L.; et al. Superconducting Nanowire Single-Photon Detectors: Physics and Applications. *Supercond. Sci. Technol. Supercond. Sci. Technol* **2012**, *25* (25), 63001–63016.
- (37) Atallah, T. L.; Sica, A. V.; Shin, A. J.; Friedman, H. C.; Kahrobai, Y. K.; Caram, J. R. Decay-Associated Fourier Spectroscopy: Visible to Shortwave Infrared Time-Resolved Photoluminescence Spectra. *J. Phys. Chem. A* **2019**, *123* (31), 6792–6798.
- (38) Štacková, L.; Muchová, E.; Russo, M.; Slavíček, P.; Štacko, P.; Klán, P. Deciphering the Structure–Property Relations in Substituted Heptamethine Cyanines. *J. Org. Chem.* **2020**, *85* (15), 9776–9790.
- (39) Matikonda, S. S.; Hammersley, G.; Kumari, N.; Grabenhorst, L.; Glembockyte, V.; Tinnefeld, P.; Ivanic, J.; Levitus, M.; Schnermann, M. J. Impact of Cyanine Conformational Restraint in the Near-Infrared Range. *J. Org. Chem.* **2020**, *85* (9), 5907–5915.
- (40) Karaca, S.; Elmacı, N. A Computational Study on the Excited State Properties of a Cationic Cyanine Dye: TTBC. *Comput. Theor. Chem.* **2011**, *964* (1–3), 160–168.
- (41) Bixon, M.; Jortner, J. Intramolecular Radiationless Transitions. *J. Chem. Phys.* **1968**, *48* (2), 715–726.
- (42) Shi, J.; Izquierdo, M. A.; Oh, S.; Park, S. Y.; Milián-Medina, B.; Roca-Sanjuán, D.; Gierschner, J. Inverted Energy Gap Law for the Nonradiative Decay in Fluorescent Floppy Molecules: Larger Fluorescence Quantum Yields for Smaller Energy Gaps. *Org.*

- Chem. Front.* **2019**, *6* (12), 1948–1954.
- (43) Hochstrasser, R. M.; Marzacco, C. Perturbations between Electronic States in Aromatic and Heteroaromatic Molecules. *J. Chem. Phys.* **1968**, *49* (3), 971–984.
- (44) Zerbetto, F.; Zgierski, M. Z.; Orlandi, G.; Marconi, G. Vibronic Coupling in Polyenes and Their Derivatives. Interpretation of the Absorption and Emission Spectra of a Derivative of Dodecahexaene. *J. Chem. Phys.* **1987**, *87* (5), 2505–2512.
- (45) Russin, T. J.; Altinoğlu, E. İ.; Adair, J. H.; Eklund, P. C. Measuring the Fluorescent Quantum Efficiency of Indocyanine Green Encapsulated in Nanocomposite Particulates. *J. Phys. Condens. Matter* **2010**, *22* (33), 334217.
- (46) Rurack, K.; Spieles, M. Fluorescence Quantum Yields of a Series of Red and Near-Infrared Dyes Emitting at 600–1000 Nm. *Anal. Chem.* **2011**, *83* (4), 1232–1242.
- (47) Ayala-Orozco, C.; Liu, J. G.; Knight, M. W.; Wang, Y.; Day, J. K.; Nordlander, P.; Halas, N. J. Fluorescence Enhancement of Molecules inside a Gold Nanomatryoshka. *Nano Lett.* **2014**, *14* (5), 2926–2933.
- (48) Li, B.; Lu, L.; Zhao, M.; Lei, Z.; Zhang, F. An Efficient 1064 Nm NIR-II Excitation Fluorescent Molecular Dye for Deep-Tissue High-Resolution Dynamic Bioimaging. *Angew. Chemie Int. Ed.* **2018**, *57* (25), 7483–7487.
- (49) Wang, S.; Fan, Y.; Li, D.; Sun, C.; Lei, Z.; Lu, L.; Wang, T.; Zhang, F. Anti-Quenching NIR-II Molecular Fluorophores for in Vivo High-Contrast Imaging and PH Sensing. *Nat. Commun.* **2019**, *10* (1), 1058.



- (50) Shi, Y.; Yuan, W.; Liu, Q.; Kong, M.; Li, Z.; Feng, W.; Hu, K.; Li, F. Development of Polyene-Bridged Hybrid Rhodamine Fluorophores for High-Resolution NIR-II Imaging. *ACS Mater. Lett.* **2019**, 418–424.
- (51) Lei, Z.; Sun, C.; Pei, P.; Wang, S.; Li, D.; Zhang, X.; Zhang, F. Stable, Wavelength-Tunable Fluorescent Dyes in the NIR-II Region for In Vivo High-Contrast Bioimaging and Multiplexed Biosensing. *Angew. Chemie - Int. Ed.* **2019**, 58 (24), 8166–8171.
- (52) Zhang, F.; Li, B.; Zhao, M. Fluorescent Dye Excited/Emitted by Second Infrared Window and Preparation Method Thereof. CN 110079117, 2019.
- (53) Hansch, C.; Leo, A.; Taft, R. W. *A Survey of Hammett Substituent Constants and Resonance and Field Parameters*; 1991; Vol. 91.
- (54) Kasha, M.; Rawls, H. R.; El-Bayoumi, M. A. The Exciton Model In Molecular Spectroscopy. *Pure Appl. Chem.* **1965**.
- (55) Chen, W.; Cheng, C. A.; Cosco, E. D.; Ramakrishnan, S.; Lingg, J. G. P.; Bruns, O. T.; Zink, J. I.; Sletten, E. M. Shortwave Infrared Imaging with J-Aggregates Stabilized in Hollow Mesoporous Silica Nanoparticles. *J. Am. Chem. Soc.* **2019**, 141 (32), 12475–12480.
- (56) Sun, C.; Li, B.; Zhao, M.; Wang, S.; Lei, Z.; Lu, L.; Zhang, H.; Feng, L.; Dou, C.; Yin, D.; et al. J-Aggregates of Cyanine Dye for NIR-II in Vivo Dynamic Vascular Imaging beyond 1500 Nm. *J. Am. Chem. Soc.* **2019**, 141 (49), 19221–19225.
- (57) Symes, R.; Sayer, R. M.; Reid, J. P. Cavity Enhanced Droplet Spectroscopy: Principles,

- Perspectives and Prospects. *Phys. Chem. Chem. Phys.* **2004**, *6* (3), 474–487.
- (58) Barnes, M. D.; Whitten, W. B.; Ramsey, J. M. Enhanced Fluorescence Yields through Cavity Quantum-Electrodynamic Effects in Microdroplets. *J. Opt. Soc. Am. B* **1994**, *11* (7), 1297.
- (59) Lu, X.; Ye, G.; Punj, D.; Chiechi, R. C.; Orrit, M. Quantum Yield Limits for the Detection of Single-Molecule Fluorescence Enhancement by a Gold Nanorod. *ACS Photonics* **2020**, *7* (9), 2498–2505.
- (60) Srinivasan, V.; Ramamurthy, S. S. Purcell Factor: A Tunable Metric for Plasmon-Coupled Fluorescence Emission Enhancements in Cermet Nanocavities. *J. Phys. Chem. C* **2016**, *120* (5), 2908–2913.
- (61) G. Avramenko, A.; S. Rury, A. Quantum Control of Ultrafast Internal Conversion Using Nanoconfined Virtual Photons. *J. Phys. Chem. Lett.* **2020**, *11* (3), 1013–1021.
- (62) S. Ulusoy, I.; A. Gomez, J.; Vendrell, O. Modifying the Nonradiative Decay Dynamics through Conical Intersections via Collective Coupling to a Cavity Mode. *J. Phys. Chem. A* **2019**, *123* (41), 8832–8844.
- (63) Humeniuk, A.; Mitrić, R.; Bonačić-Koutecký, V. Size Dependence of Non-Radiative Decay Rates in J-Aggregates. *J. Phys. Chem. A* **2020**, *124* (49), 10143–10151.
- (64) Kusinski, M.; Nagesh, J.; Gladkikh, M.; Izmaylov, A. F.; Jockusch, R. A. Deuterium Isotope Effect in Fluorescence of Gaseous Oxazine Dyes. *Phys. Chem. Chem. Phys.* **2019**, *21* (10), 5759–5770.

- (65) Hirata, S.; Totani, K.; Watanabe, T.; Kaji, H.; Vacha, M. Relationship between Room Temperature Phosphorescence and Deuteration Position in a Purely Aromatic Compound. *Chem. Phys. Lett.* **2014**, *591*, 119–125.
- (66) Bai, L.; Sun, P.; Liu, Y.; Zhang, H.; Hu, W.; Zhang, W.; Liu, Z.; Fan, Q.; Li, L.; Huang, W. Novel Aza-BODIPY Based Small Molecular NIR-II Fluorophores for: In Vivo Imaging. *Chem. Commun.* **2019**, *55* (73), 10920–10923.
- (67) Chung, P.-H.; Tregidgo, C.; Suhling, K. Determining a Fluorophore's Transition Dipole Moment from Fluorescence Lifetime Measurements in Solvents of Varying Refractive Index. *Methods Appl. Fluoresc.* **2016**, *4* (4), 045001.
- (68) Marciniak, H.; Auerhammer, N.; Ricker, S.; Schmiedel, A.; Holzapfel, M.; Lambert, C. Reduction of the Fluorescence Transition Dipole Moment by Excitation Localization in a Vibronically Coupled Squaraine Dimer. *J. Phys. Chem. C* **2019**, *123* (6), 3426–3432.
- (69) Fron, E.; Coutiño-Gonzalez, E.; Pandey, L.; Sliwa, M.; Van Der Auweraer, M.; De Schryver, F. C.; Thomas, J.; Dong, Z.; Leen, V.; Smet, M.; et al. Synthesis and Photophysical Characterization of Chalcogen Substituted BODIPY Dyes. *New J. Chem.* **2009**, *33* (7), 1490–1496.
- (70) Zhang, X. F.; Zhang, J.; Liu, L. Fluorescence Properties of Twenty Fluorescein Derivatives: Lifetime, Quantum Yield, Absorption and Emission Spectra. *J. Fluoresc.* **2014**, *24* (3), 819–826.
- (71) Yang, Q.; Hu, Z.; Zhu, S.; Ma, R.; Ma, H.; Ma, Z.; Wan, H.; Zhu, T.; Jiang, Z.; Liu, W.; et al. Donor Engineering for NIR-II Molecular Fluorophores with Enhanced Fluorescent

- Performance. *J. Am. Chem. Soc.* **2018**, *140* (5), 1715–1724.
- (72) Zhu, X.; Liu, C.; Hu, Z.; Liu, H.; Wang, J.; Wang, Y.; Wang, X.; Ma, R.; Zhang, X.; Sun, H.; et al. High Brightness NIR-II Nanofluorophores Based on Fused-Ring Acceptor Molecules. *Nano Res.* **2020**, *13* (9), 2570–2575.
- (73) Cooper, M.; Ebner, A.; Briggs, M.; Burrows, M.; Gardner, N.; Richardson, R.; West, R. *Cy3B TM : Improving the Performance of Cyanine Dyes*; 2004; Vol. 14.
- (74) Sanborn, M. E.; Connolly, B. K.; Gurunathan, K.; Levitus, M. Fluorescence Properties and Photophysics of the Sulfoindocyanine Cy3 Linked Covalently to DNA. *J. Phys. Chem. B* **2007**, *111* (37), 11064–11074.
- (75) Waggoner, A. S.; Mujumdar, R. B. Rigidized Trimethine Cyanine Dyes, 1998.
- (76) Michie, M. S.; Götz, R.; Franke, C.; Bowler, M.; Kumari, N.; Magidson, V.; Levitus, M.; Loncarek, J.; Sauer, M.; Schnermann, M. J. Cyanine Conformational Restraint in the Far-Red Range. *J. Am. Chem. Soc.* **2017**, *139* (36), 12406–12409.
- (77) Maillard, J.; Klehs, K.; Rumble, C.; Vauthey, E.; Heilemann, M.; Fürstenberg, A. Universal Quenching of Common Fluorescent Probes by Water and Alcohols. *Chem. Sci.* **2021**, *12* (4), 1352–1362.
- (78) Wen, Q.; V. Kershaw, S.; Kalytchuk, S.; Zhovtiuk, O.; Reckmeier, C.; I. Vasilevskiy, M.; L. Rogach, A. Impact of D<sub>2</sub>O/H<sub>2</sub>O Solvent Exchange on the Emission of HgTe and CdTe Quantum Dots: Polaron and Energy Transfer Effects. *ACS Nano* **2016**, *10* (4), 4301–4311.
- (79) Aharoni, A.; Oron, D.; Banin, U.; Rabani, E.; Jortner, J. Long-Range Electronic-to-

- Vibrational Energy Transfer from Nanocrystals to Their Surrounding Matrix Environment. *Phys. Rev. Lett.* **2008**, *100* (5), 057404.
- (80) Pengshung, M.; Neal, P.; Atallah, T. L.; Kwon, J.; Caram, J. R.; Lopez, S. A.; Sletten, E. M. Silicon Incorporation in Polymethine Dyes. *Chem. Commun.* **2020**, *56* (45), 6110–6113.
- (81) Hirayama, S.; Phillips, D. Correction for Refractive Index in the Comparison of Radiative Lifetimes in Vapour and Solution Phases. *J. Photochem.* **1980**, *12* (2), 139–145.
- (82) Toptygin, D. Effects of the Solvent Refractive Index and Its Dispersion on the Radiative Decay Rate and Extinction Coefficient of a Fluorescent Solute. *Journal of Fluorescence*. May 2003, pp 201–219.
- (83) Fox, M. *Quantum Optics: An Introduction (Oxford Master Series in Physics)*; 1970.
- (84) Lin, Z.; W. Kohn, A.; Van Voorhis, T. Toward Prediction of Nonradiative Decay Pathways in Organic Compounds II: Two Internal Conversion Channels in BODIPYs. *J. Phys. Chem. C* **2020**, *124* (7), 3925–3938.
- (85) Faraji, S.; Matsika, S.; Krylov, A. I. Calculations of Non-Adiabatic Couplings within Equation-of-Motion Coupled-Cluster Framework: Theory, Implementation, and Validation against Multi-Reference Methods. *J. Chem. Phys.* **2018**, *148* (4), 044103.
- (86) Warshel, A.; Dauber, P. Calculations of Resonance Raman Spectra of Conjugated Molecules. *J. Chem. Phys.* **1977**, *66* (12), 5477–5488.
- (87) Piwoński, H.; Nozue, S.; Habuchi, S. The Pursuit of Shortwave Infrared-Emitting

- Nanoparticles with Bright Fluorescence through Molecular Design and Excited-State Engineering of Molecular Aggregates. *ACS Nanosci. Au* **2022**, 0 (0).
- (88) Zhang, F.; Lei, Z. Molecular Engineering of NIR-II Fluorophores for Improved Biomedical Detection. *Angew. Chemie* **2020**, ange.202007040.
- (89) McNamara, L. E.; Boyn, J. N.; Melnychuk, C.; Anferov, S. W.; Mazziotti, D. A.; Schaller, R. D.; Anderson, J. S. Bright, Modular, and Switchable Near-Infrared II Emission from Compact Tetrathiafulvalene-Based Diradicaloid Complexes. *J. Am. Chem. Soc.* **2022**.
- (90) Ma, H.; Liu, C.; Hu, Z.; Yu, P.; Zhu, X.; Ma, R.; Sun, Z.; Zhang, C. H.; Sun, H.; Zhu, S.; et al. Propylenedioxy Thiophene Donor to Achieve NIR-II Molecular Fluorophores with Enhanced Brightness. *Chem. Mater.* **2020**, 32 (5), 2061–2069.
- (91) Cademartiri, L.; Montanari, E.; Calestani, G.; Migliori, A.; Guagliardi, A.; Ozin, G. A. Size-Dependent Extinction Coefficients of PbS Quantum Dots. *J. Am. Chem. Soc.* **2006**, 128 (31), 10337–10346.
- (92) De Jong, M.; Seijo, L.; Meijerink, A.; Rabouw, F. T. Resolving the Ambiguity in the Relation between Stokes Shift and Huang–Rhys Parameter. *Phys. Chem. Chem. Phys.* **2015**, 17 (26), 16959–16969.
- (93) Friedman, H. C.; Cosco, E. D.; Atallah, T. L.; Jia, S.; Sletten, E. M.; Caram, J. R. Establishing Design Principles for Emissive Organic SWIR Chromophores from Energy Gap Laws. *Chem* **2021**, 7 (12), 3359–3376.
- (94) Tolbert, L. M.; Zhao, X. Beyond the Cyanine Limit: Peierls Distortion and Symmetry

- Collapse in a Polymethine Dye. *J. Am. Chem. Soc.* **1997**, *119* (14), 3253–3258.
- (95) Sissa, C.; Painelli, A.; Terenziani, F.; Trotta, M.; Ragni, R. About the Origin of the Large Stokes Shift in Aminoalkyl Substituted Heptamethine Cyanine Dyes. *Phys. Chem. Chem. Phys.* **2019**, *22* (1), 129–135.
- (96) Zhang, J.; Moemeni, M.; Yang, C.; Liang, F.; Peng, W. T.; Levine, B. G.; Lunt, R. R.; Borhan, B. General Strategy for Tuning the Stokes Shifts of near Infrared Cyanine Dyes. *J. Mater. Chem. C* **2020**, *8* (47), 16769–16773.
- (97) Li, D. H.; Smith, B. D. Deuterated Indocyanine Green (ICG) with Extended Aqueous Storage Shelf-Life: Chemical and Clinical Implications. *Chem. – A Eur. J.* **2021**, *27* (58), 14535–14542.
- (98) Guthmuller, J. The Role of Herzberg-Teller Effects on the Resonance Raman Spectrum of Trans -Porphycene Investigated by Time Dependent Density Functional Theory. *J. Chem. Phys.* **2018**, *148* (12), 124107.
- (99) Grimm, J. B.; Xie, L.; Casler, J. C.; Patel, R.; Tkachuk, A. N.; Falco, N.; Choi, H.; Lippincott-Schwartz, J.; Brown, T. A.; Glick, B. S.; et al. A General Method to Improve Fluorophores Using Deuterated Auxochromes. *JACS Au* **2021**, *1* (5), 690–696.
- (100) Avila Ferrer, F. J.; Barone, V.; Cappelli, C.; Santoro, F. Duschinsky, Herzberg–Teller, and Multiple Electronic Resonance Interferential Effects in Resonance Raman Spectra and Excitation Profiles. The Case of Pyrene. *J. Chem. Theory Comput.* **2013**, *9* (8), 3597–3611.

- (101) Barclay, M. S.; Huff, J. S.; Pensack, R. D.; Davis, P. H.; Knowlton, W. B.; Yurke, B.; Dean, J. C.; Arpin, P. C.; Turner, D. B. Characterizing Mode Anharmonicity and Huang-Rhys Factors Using Models of Femtosecond Coherence Spectra. *J. Phys. Chem. Lett.* **2022**, *13* (24), 5413–5423.
- (102) Dorn, H. P.; Müller, A. Temperature Dependence of the Fluorescence Lifetime and Quantum Yield of Pseudoisocyanine Monomers. *Chem. Phys. Lett.* **1986**, *130* (5), 426–431.
- (103) Deshmukh, A. P.; Koppel, D.; Chuang, C.; Cadena, D. M.; Cao, J.; Caram, J. R. Design Principles for Two-Dimensional Molecular Aggregates Using Kasha’s Model: Tunable Photophysics in Near and Short-Wave Infrared. *J. Phys. Chem. C* **2019**, *123* (30), 18702–18710.
- (104) Shokri, S.; Wiederrecht, G. P.; Gosztola, D. J.; Ayitou, A. J. L. Photon Upconversion Using Baird-Type (Anti)Aromatic Quinoidal Naphthalene Derivative as a Sensitizer. *J. Phys. Chem. C* **2017**, *121* (42), 23377–23382.
- (105) Lesikar I’, A. V. Organic Halide-Alcohol Interactions: Observation by Means of the Glass Transition. *J. Solution Chem.* **1977**, *6* (12).
- (106) Sola-Llano, R.; Jiménez, J.; Avellanal-Zaballa, E.; Johnson, M.; Cabrerros, T. A.; Moreno, F.; Maroto, B. L.; Muller, G.; Bañuelos, J.; Cerdán, L.; et al. BOPHYs versus BODIPYs: A Comparison of Their Performance as Effective Multi-Function Organic Dyes. *Dye. Pigment.* **2019**, *170*, 107662.
- (107) Liu, H.; Yin, J.; Xing, E.; Du, Y.; Su, Y.; Feng, Y.; Meng, S. Halogenated Cyanine Dyes



- for Synergistic Photodynamic and Photothermal Therapy. *Dye. Pigment.* **2021**, *190*, 109327.
- (108) Gorman, A.; Killoran, J.; O'Shea, C.; Kenna, T.; M. Gallagher, W.; F. O'Shea, D. In Vitro Demonstration of the Heavy-Atom Effect for Photodynamic Therapy. *J. Am. Chem. Soc.* **2004**, *126* (34), 10619–10631.
- (109) She, P.; Yu, Y.; Qin, Y.; Zhang, Y.; Li, F.; Ma, Y.; Liu, S.; Huang, W.; Zhao, Q.; She, P. F.; et al. Controlling Organic Room Temperature Phosphorescence through External Heavy-Atom Effect for White Light Emission and Luminescence Printing. *Adv. Opt. Mater.* **2020**, *8* (4), 1901437.
- (110) Baleizão, C.; Berberan-Santos, M. N. External Heavy-Atom Effect on the Prompt and Delayed Fluorescence of [70]Fullerenes. *ChemPhysChem* **2010**, *11* (14), 3133–3140.
- (111) Stsiapura, V. I.; Kurhuzenkau, S. A.; Kuzmitsky, V. A.; Bouganov, O. V.; Tikhomirov, S. A. Solvent Polarity Effect on Nonradiative Decay Rate of Thioflavin T. *J. Phys. Chem. A* **2016**, *120* (28), 5481–5496.
- (112) Jang, S. J. A Simple Generalization of the Energy Gap Law for Nonradiative Processes. **2021**.
- (113) Valiev, R. R.; Cherepanov, V. N.; Nasibullin, R. T.; Sundholm, D.; Kurten, T. Calculating Rate Constants for Intersystem Crossing and Internal Conversion in the Franck-Condon and Herzberg-Teller Approximations. *Phys. Chem. Chem. Phys.* **2019**, *21* (34), 18495–18500.

- (114) Kushida, Y.; Nagano, T.; Hanaoka, K. Silicon-Substituted Xanthene Dyes and Their Applications in Bioimaging. *Analyst* **2015**, *140* (3), 685–695.
- (115) Rathnamalala, C. S. L.; Gayton, J. N.; Dorris, A. L.; Autry, S. A.; Meador, W.; Hammer, N. I.; Delcamp, J. H.; Scott, C. N. Donor–Acceptor–Donor NIR II Emissive Rhodindolizine Dye Synthesized by C–H Bond Functionalization. **2019**.
- (116) Chatterjee, S.; Shaik, A. K.; Wijesinghe, K. H.; Ndaleh, D.; Dass, A.; Hammer, N. I.; Delcamp, J. H. Design and Synthesis of RhodIndolizine Dyes with Improved Stability and Shortwave Infrared Emission up to 1250 Nm. *J. Org. Chem.* **2022**, *87* (17), 11319–11328.
- (117) Zheng, L.; Polizzi, N. F.; Dave, A. R.; Migliore, A.; Beratan, D. N. Where Is the Electronic Oscillator Strength? Mapping Oscillator Strength across Molecular Absorption Spectra. **2016**.
- (118) Liu, D.; He, Z.; Zhao, Y.; Yang, Y.; Shi, W.; Li, X.; Ma, H. Xanthene-Based NIR-II Dyes for In Vivo Dynamic Imaging of Blood Circulation. *Cite This J. Am. Chem. Soc* **2021**, *143*, 17136–17143.
- (119) Daly, H. C.; Matikonda, S. S.; Steffens, H. C.; Ruehle, B.; Resch-Genger, U.; Ivanic, J.; Schnermann, M. J. Ketone Incorporation Extends the Emission Properties of the Xanthene Scaffold Beyond 1000 Nm†. *Photochem. Photobiol.* **2022**, *98* (2), 325–333.
- (120) Qian, G.; Dai, B.; Luo, M.; Yu, D.; Zhan, J.; Zhang, Z.; Ma, D.; Yuan Wang, Z. Band Gap Tunable, Donor–Acceptor–Donor Charge-Transfer Heteroquinoid-Based Chromophores: Near Infrared Photoluminescence and Electroluminescence. *Chem. Mater.* **2008**, *20* (19), 6208–6216.

- (121) Zhu, S.; Tian, R.; Antaris, A. L.; Chen, X.; Dai, H. Near-Infrared-II Molecular Dyes for Cancer Imaging and Surgery. *Adv. Mater.* **2019**, *31* (24), 1900321.
- (122) Li, D. H.; Smith, B. D. Supramolecular Mitigation of the Cyanine Limit Problem. *J. Org. Chem.* **2022**, *87* (9), 5893–5903.
- (123) Cravcenco, A.; Yu, Y.; Edhborg, F.; Goebel, J. F.; Takacs, Z.; Yang, Y.; Albinsson, B.; Börjesson, K. Exciton Delocalization Counteracts the Energy Gap: A New Pathway toward NIR-Emissive Dyes. *J. Am. Chem. Soc.* **2021**, *18*, jacs.1c10654.
- (124) Qiu, X.; Tian, G.; Lin, C.; Pan, Y.; Ye, X.; Wang, B.; Ma, D.; Hu, D.; Luo, Y.; Ma, Y. Narrowband Emission from Organic Fluorescent Emitters with Dominant Low-Frequency Vibronic Coupling. *Adv. Opt. Mater.* **2021**, *9* (4), 2001845.
- (125) Shreve, A. P.; Haroz, E. H.; Bachilo, S. M.; Weisman, R. B.; Tretiak, S.; Kilina, S.; Doorn, S. K. Determination of Exciton-Phonon Coupling Elements in Single-Walled Carbon Nanotubes by Raman Overtone Analysis. **2007**.